**UNIVERSIDAD NACIONAL AUTÓNOMA DE MÉXICO**
PROGRAMA DE MAESTRÍA Y DOCTORADO EN INGENIERÍA
ENERGÍA – PROCESOS Y USO EFICIENTE DE ENERGÍA

# Experimental and Numerical Study of Magnetohydrodynamic Flow Instabilities in a Cylindrical Cavity

## TESIS

QUE PARA OPTAR POR EL GRADO DE:
**DOCTOR EN INGENIERÍA**

PRESENTA:
**James Pérez Barrera**

TUTOR PRINCIPAL:
**Dr. Sergio Cuevas García, Instituto de Energías Renovables**

COMITÉ TUTOR:
Dr. Eduardo Ramos Mora, IER-UNAM
Dr. Mariano López de Haro, IER-UNAM
Dr. Rubén Ávila Rodríguez, Facultad de Ingeniería, UNAM
Dr. Raúl Alejandro Ávalos Zúñiga, CICATA-IPN

CIUDAD DE MÉXICO, Enero 2018

**JURADO ASIGNADO:**

| | |
|---|---|
| Presidente: | Dr. Mariano López de Haro, IER-UNAM |
| Secretario: | Dr. Rubén Ávila Rodríguez, Facultad de Ingeniería, UNAM |
| Vocal: | Dr. Sergio Cuevas García, IER-UNAM |
| 1 er. Suplente: | Dr. Dmitry Krasnov, TUI, Ilmenau, Alemania |
| 2 d o. Suplente: | Dr. Aldo Figueroa Lara, Facultad de Ciencias, UAEM |

Lugar o lugares donde se realizó la tesis: Instituto de Energías Renovables (IER-UNAM)
Osservatorio Astronomico di Cagliari (Italia)
Technische Universität Ilmenau (TUI, Alemania)

**TUTOR DE TESIS:**

Dr. Sergio Cuevas García

_____

**FIRMA**

# Contents

# Resumen

En esta tesis se presenta un estudio experimental, analítico y numérico de la dinámica del flujo en una capa delgada producido en un agitador electromagnético con geometría cilíndrica bajo distintas condiciones experimentales. El fluido de trabajo empleado es una solución electrolítica de baja conductividad eléctrica sobre la que actúa una fuerza de cuerpo electromagnética azimutal producida por la interacción de una corriente eléctrica directa radial y un campo magnético externo esencialmente vertical. La tesis se enfoca en el estudio teórico y experimental de una inestabilidad recien descubierta. Se utilizaron distintas formas de visualización y análisis de los patrones de flujo que incluyen el uso de tinta trazadora, mediciones mediante Velocimetría por Imágenes de Partículas (PIV, por sus siglas en inglés) e imágenes termográficas. Desde el punto de vista teórico se exploraron soluciones cuasi-bidimensionales con diferentes condiciones de frontera y soluciones numéricas tridimensionales de las ecuaciones de balance que modelan el sistema, mismas que fueron resueltas utilizando una técnica numérica híbrida volumen finito - Fourier espectral. En el Capítulo 1 se presenta la descripción detallada del dispositivo, las condiciones experimentales de interés y las formas de visualización de los patrones de flujo, así como la descripción del flujo que da lugar a la inestabilidad reportada, consistente en el surgimiento de vórtices anticiclónicos en un flujo azimutal. Se muestra que la técnica PIV no es capaz de capturar adecuadamente el campo de velocidades, particularmente los vórtices que surgen cuando el flujo presenta la inestabilidad. Por tanto, se muestran resultados preliminares de una técnica mejorada que permite visualizar los vórtices anticiclónicos. En el Capítulo 2 se obtienen soluciones analíticas del flujo azimutal en el agitador tanto para el caso de un metal líquido como de un electrolito, utilizando una aproximación cuasi-bidimensional y considerando condiciones generales de deslizamiento. En el tercer Capítulo se presentan las soluciones numéricas tridimensionales obtenidas aplicando el método híbrido desarrollado por Nuñez *et al.* (2012) considerando condiciones experimentales realistas. A partir de dichas soluciones es posible describir de manera detallada la dinámica tridimensional

del flujo, tanto para flujos axisimétricos mayormente azimutales como para aquellos donde se observa la inestabilidad. Los resultados numéricos se comparan satisfactoriamente con las observaciones experimentales, tanto cuantitativa como cualitativamente.

Con el objetivo de que esta tesis sea autocontenida se incluyen tres apéndices. En el Apéndice A se describen brevemente las ecuaciones fundamentales de la magnetohidrodinámica (MHD) que gobiernan el comportamiento de un fluido Newtoniano, conductor, no magnetizable e incompresible. Haciendo uso de la aproximación de bajo número de Reynolds magnético, dichas ecuaciones se expresan utilizando la velocidad, la presión y el potencial eléctrico como variables primitivas. En el Apéndice B se describe el método numérico empleado en el presente trabajo y se discuten algunas de sus principales ventajas. El Apéndice C describe algunas técnicas de solución numérica de ecuaciones diferenciales parciales hiperbólicas de interés para el estudio de flujos astrofísicos, y que fueron estudiadas durante una estancia corta en el Osservatorio Astronomico di Cagliari, en Cagliari, Italia como parte de un Programa de Entrenamiento para Jóvenes Investigadores (YITP, por sus siglas en inglés) patrocinado por el gobierno italiano.

# Abstract

In this thesis, an experimental, analytical and numerical study of the flow dynamics in a thin layer produced by an electromagnetic stirrer with cylindrical geometry under different experimental conditions, is presented. In the stirrer, an azimuthal electromagnetic force generated by the interaction of a radial electric current and a mainly vertical magnetic field drives a low conductivity electrolytic solution. The thesis is focused on the theoretical and experimental characterization of a recently discovered hydrodynamic instability. Different techniques of visualization and analysis of the flow patterns such as tracking of dye tracers, Particle Image Velocimetry (PIV) measurements and thermographic images were used. From the theoretical point of view, quasi-two-dimensional solutions considering different boundary conditions and three-dimensional numerical solutions of the governing equations obtained using a hybrid finite volume - Fourier spectral numerical technique were explored. Chapter 1 presents the detailed description of the device, the experimental conditions of interest and the visualization techniques of the flow patterns, as well as the description of the flow that originates the reported instability, which consists in the emergence of anticyclonic vortices on a base azimuthal flow. It is shown that PIV technique is not capable of properly capturing the velocity field, particularly that of the vortices that appear when the instability is triggered. Nevertheless, preliminary results of an improved PIV technique which allows the measurement of the anticyclonic vortices, are shown. In Chapter 2, solutions of the governing equations using a quasi-two-dimensional approximation, are obtained for both liquid metal and electrolyte flows, considering general slip conditions. Chapter 3 presents the three-dimensional numerical solutions obtained by using the hybrid methodology proposed by Nuñez *et al.* (2012), considering realistic experimental conditions. From these solutions it is possible to describe in detail the three-dimensional dynamics of the flow, both for the mainly azimuthal flows as well as for those flows where the instability is triggered. The numerical results are in good agreement, both qualitatively and quantitatively, with the experimental observations.

In an attempt to make this thesis self-contained, three appendices are included. Appendix A briefly describes the fundamental magnetohydrodynamic (MHD) equations that govern the motion of a Newtonian, electrically conducting, non-magnetizable, incompressible fluid. By applying the low magnetic Reynolds number approximation, such equations are expressed in terms of the velocity, pressure and electric potential as primitive variables. Appendix B describes the numerical method used in this work and discusses some of its main advantages. Appendix C describes some numerical techniques to solve hyperbolic partial differential equations of interest for the analysis of astrophysical flows that were studied during a short-term stay at the Osservatorio Astronomico di Cagliari, in Cagliari, Italy as a part of a Young Invertigators Training Program (YITP) supported by the Italian goverment.

# Introduction

*MagnetoHydroDynamics* (MHD) is the branch of physics which combines the subjects of fluid dynamics and electromagnetism to study the behavior of electrically conducting, non-magnetizable fluids interacting with magnetic fields. In nature, these kind of phenomena appear in a wide range of situations from geophysical phenomena, like the dynamo effect (which is the most accepted theory to explain the existence of Earth's magnetic field), to the formation and evolution of stars and galaxies [Bachetti *et al.* (2010), Romanova *et al.* (2013)]. From the technological point of view, MHD can be used to improve or control processes of industrial importance since, in many technological applications, working fluids are electrically conducting, for instance, liquid metals, electrolytes and molten salts. In such fluids, electromagnetic forces can be used to control, stir, pump, levitate or enhance the heat transfer, thus improving the energy usage and minimizing losses.

The non-intrusive nature of electromagnetic forces provides an alternative to mechanical direct-contact forces for the handling of electrically conducting fluids. Due to this fact, in the past few decades, several industrial processes have taken advantage of the tools offered by MHD to achieve technological improvements [Asai (2012)]. Such processes are employed, for instance, in the metallurgical and nuclear engineering industries. In fact, the use of electromagnetic fields for handling, control, transport and monitoring of electrically conducting fluids in different industrial applications has been named Electromagnetic Processing of Materials (EPM). A good example is the Czochralski's method, used to manufacture crystalline silicon. In this method, a silicon crystal seed is immersed and rotated in melted silicon and, after a cooling process, a larger crystal with a homogeneous concentration of aditives, known as dopants, is obtained. Since crystalline silicon is used in electronic devices, the crystaline structure and concentration of dopants are crucial because they greatly affect the properties of the material. High quality silicon can be obtained by controlling in a very precise way the crystallization and doping processes. As several authors, Hjellming & Walker (1986) suggested the use of magnetic fields to control the motion

of liquid silicon and, as a result, obtain crystals with better electronic properties.

In many industrial processes, stirring and mixing of fluids is very important. In the food, painting, chemical, metallurgical, pharmaceutical, and many others industries, the efficiency of these processes has a major impact in the quality of the final products. In general terms, stirring refers to the creation of recirculating motion inside the fluid, whereas mixing is normally used to obtain a homogeneous concentration of a physical quantity from an originally inhomogeneous state. Effective stirring and mixing can be achieved by means of electromagnetic forces either by inducing electrical currents in a highly conducting fluid (*v. e.* a liquid metal) or by directly injecting electrical currents in a conducting fluid (*v. e.* an electrolyte or a liquid metal) and making it interact with an external magnetic field. In any case, MHD flows have proven to be useful for the stirring and mixing of electrically conducting fluids required in different industrial applications [Asai (2012)].

A major advantage of MHD-driven flows is the absence of direct contact of the working fluid with an external agent, so that the purity of the fluid can be preserved while the dynamics of the flow can be controlled in a precise way. The non-intrusive nature of MHD phenomena is also very important in the so-called Lorentz force velocimetry (LFV), which is a novel technique used to measure local and global velocities in melted metals and electrolytes. LFV is a suitable alternative to the traditional intrusive or optical techniques, particularly for liquid metals which are opaque and often hot and aggresive [Thess *et al.* (2006), Thess *et al.* (2007)].

In the past few decades, many technological efforts have been focused in miniaturazing devices with the aim of using them in medical, biological and chemical applications. The idea is to build small scale devices capable of performing, for instance, diagnostic tests or chemical reactions with a minimum volume of body fluids or reactants. Although the so-called *Lab-on-a-chip* systems have gained a lot of attention in recent years [Li (2005), Ghallab & Badawy (2010)], still some challenges must be overcome since, incidentally, building micro-sized components can be a difficult, expensive task, not to mention the inherent difficulties of the accurate control of the involved substances. The branch of fluid mechanics which deals with flows at micro scales is the *microfluidics* and the potential application of MHD in this area has been succesfully demonstrated [see, for instance, Yi *et al.* (2002), Qian & Bau (2009)]. In fact, it has been shown that, as occur at larger scales, magnetic fields can be used in microfluidic devices for different purposes such as stirring, pumping, controlling and monitoring of conducting liquids, mainly electrolytes, chemical or biological fluids.

A not so evident application of MHD is the modeling of atmospheric and meteoro-

logical phenomena at laboratory scale, as evidenced by the large amount of studies performed in the former Soviet Union and Russia [Bondarenko & Gak (1978), Bondarenko *et al.* (1979), Dovzhenko *et al.* (1979), Ponomarev (1980), Dovzhenko *et al.* (1981), Gak (1981), Krymov (1989), Manin (1989), Batchaev & Ponomarev (1989), Dolzhanskii *et al.* (1990), Dolzhanskii *et al.* (1992), Bondarenko *et al.* (2002), Gledzer *et al.* (2013) and references therein]. The so-called *MHD method*, consists in producing Lorentz forces in a thin layer of an electrolyte through the injection of an electric current that interacts with different configurations of an external magnetic field. This method has been used to generate vortex patterns that resemble structures observed at geophysical or even planetary scale. The use of thin electrolyte layers is justified by the fact that phenomena ocurring in the atmosphere are, indeed, very thin because they occur in horizontal scales of the order of hundreds of kilometers, whereas its vertical scales span up to ten kilometers height, thus the typical aspect ratio for these phenomena is around 0.1 or less. The latter statement implies that, in principle, two-dimensional or quasi-two-dimensional approaches can be succesfully applied to model approximately phenomena such as cyclones, tropical storms or hurricanes, and the MHD method provides a very simple and efficient way to create and control flows resembling those observed in the atmosphere.

As it can be seen from the previous descriptions, MHD has a large potential of application in science, engineering and technology. With that in mind, the Renewable Energy Institute of the National Autonomous University of Mexico (IER-UNAM), has developed a research program on different MHD flows of fundamental and applied interest. These include, for instance, the study of vortex dynamics and mixing in thin layers of electrolytes and liquid metals driven by localized electromagnetic forces [Figueroa (2010), Beltrán (2010)], the effect of a magnetic field in natural convection [Nuñez (2012)], enhancement of heat transfer using electromagnetic forces [Román (2012)], the liquid metal flow past localized magnetic fields [Domínguez (2013)] and the use of MHD generators for wave energy conversion. In these studies, experimental, analytical and numerical techniques have been developed and applied to obtain a better comprehension of the physical situations.

In the present work, experimental, analytical and numerical studies of the electromagnetically driven free surface flow of an electrolyte in a cylindrical geometry are presented. The main motivation is the understanding and modeling of a new type of instability recently discovered experimentally at IER-UNAM, which could be of relevance for mixing purposes and the modeling of atmospheric phenomena. Magnetohydrodynamic flows in annular ducts have been widely explored both experimentally and theoretically. From the experimental point of view, annular ducts avoid the

difficulty of considering the entrance region that is present in rectilinear ducts under a transversal magnetic field. In the most common configuration, the annular duct is formed in the gap between two coaxial electrically conducting cylinders, limited by insulating top and bottom walls. By placing the duct on top of a permanent magnet or at the center of a magnetic solenoid, an approximately uniform magnetic field parallel to the cylinder's axis is induced. If an electric potential difference is applied between the coaxial cylinders, a radial electric current density will arise in the conducting fluid. The interaction of the radial current with the axial magnetic field produces an azimuthal Lorentz force that drives the flow. Some early works dealt with this problem theoretically and analytical solutions for simplied models were obtained [Chang & Lundgren (1959), Kessey (1964), Schweitzer & Soler (1970)]. Since the pioneering works of Baylis (1971) and Baylis & Hunt (1971), attention has been mainly focused on liquid metals at high Hartmann numbers, motivated by important applications related to metallurgy and fusion blanket technologies. Moresco & Alboussière (2004) used the annular duct configuration to investigate experimentally the stability properties of the Hartmann layer and the transition to turbulence in liquid metal flow. In turn, Mikhailovich (2010) performed an experimental study of the rotaing flow of liquid metal driven by an azimuthal force in an annular container. In a more recent study, Mikhailovich *et al.* (2012) analyzed the decay of mean velocity components and turbulent fluctuations, as well as the peculiarities of spectral characteristics of such flows. Zhao *et al.* (2011) explored numerically the centrifugal instability between coaxial infinite conducting cylinders at large Hartmann numbers, disregarding the Hartmann walls with the aim to understand better the role of the sidewall layers. In a subsequent numerical study, Zhao & Zikanov (2012) considered the existence of insulating top and bottom Hartmann walls in an annular (toroidal) duct of square cross-section with the same geometry and parameter range used in the experiment by Moresco & Alboussière (2004).

As shown in the previous paragraphs, there is a large body of literature devoted to liquid metal MHD flows in cylindrical cavities and annular ducts. For the electrolyte case, the number of studies is also high, and they are mostly addressed to the modeling of atmospheric phenomena, as previously mentioned. However, the majority of these studies are focused on shearing flows generated inside the annular flow region. This is achieved by using concentric ring magnets with inverted polarity. Since the direction of the Lorentz force is determined by the orientation of the current relative to the direction of the magnetic field, this configuration leads to the formation of a flow region where the Lorentz force changes abruptly from one direction to the opposite, creating a shearing force that originates the appearance of hydrodynamic instabilities. In this way it is very easy to generate vortical structures resembling

large scale atmospheric phenomena, as shown in Fig. 1a) [Dovzhenko *et al.* (1981), Dolzhanskii *et al.* (1990), Dolzhanskii *et al.* (1992)]. Although these studies present interesting results, they focus in qualitative experimental observations or analytical approaches and, to our knowledge, comprehensive numerical simulations or quantitative measurements of the velocity field have not been reported in the literature. On the other hand, experimental observations in a cylindrical electromagnetic stirrer first reported by Pérez-Espinoza (2012) account for a new instability that leads to very interesting flow patterns. Although they resemble those reported by the Soviet researchers, there is a crucial difference: the magnetic field used by Pérez-Espinoza (2012) has the same polarity in the whole flow region so that the azimuthal Lorentz force remained with the same direction in the whole flow domain (see also Pérez-Barrera *et al.* (2015)). That means that the mechanism responsible for the apperance of the vortices in the Soviet experiments is absent, nevertheless, the instability vortices are still clearly seen in the form of anticyclonic vortices, that is, vortices rotating in the opposite direction to the global azimuthal flow (see Fig. 1b). It was found that their patterns were very robust: they existed in layers of various thicknesses regardless of the shape, size or strength of the magnets used and the direction of the electric current, even though no mean counterflow was detected in the experiments. Moreover, the vortex patterns were always observed near the outer cylinder. Our experiments also demonstrated that the observed vortices arise on a background of an essentially axisymmetric flow, and thus it is natural to consider them as growing perturbations on an axisymmetric base flow [Suslov *et al.* (2017)]. Preliminary studies of this flow rised several intriguing questions that motivated the realization of an extensive experimental and theoretical study that is reported on this thesis. It includes flow visualization experiments, as well as Particle Image Velocimetry (PIV) and thermographic measurements. From the theoretical side, both analytical solutions for some simplified flow models and full three-dimensional numerical simulations that contain the essential features of the analyzed flow are presented.

The structure of this thesis is as follows. Chapter 1 describes the experimental setup, the experimental conditions and the flow visualizations performed by means of dye tracers and thermographic images for two magnetic field configurations, namely, a magnetic field with the same polarity produced by a permanent bar magnet and an array of two concentric cylindrical magnets with opposite polarity. The emergence of the flow instability that leads to the appearance of anticyclonic vortices in the first configuration is discussed and also analyzed using Particle Image Velocimetry (PIV). In Chapter 2 the governing equations are analytically solved considering a quasi-two-dimensional approach and general slip boundary conditions. The solutions for a liquid metal and electrolyte flows are presented and discussed. The numerical

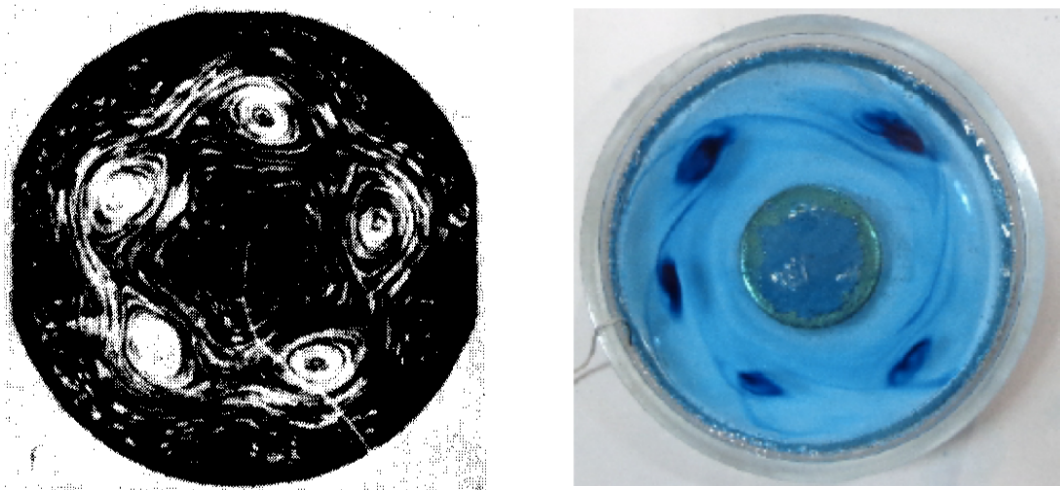

**(a)** **(b)**

Figure 1: Comparison between the flow patterns observed by *a*) Dolzhanskii *et al.* (1990) and *b*) Pérez-Espinoza (2012) created using the MHD method. In *a*) the vortices appear in a shearing flow created by the change of polarity of the magnetic field inside the electroylte layer whereas in *b*) the magnetic field has the same polarity in the whole flow region. The resemblance between the two flows is remarkable.

solution of the equations for realistic experimental conditions is presented in Chapter 3. In order to solve numerically the problem, a hybrid Fourier-Galerkin - Finite Volume scheme, as proposed by Nuñez *et al.* (2012), was implemented for the full three-dimensional (3D) flow. Numerical results are compared with experimental data finding both qualitative and quantitative agreement. The last Chapter presents the concluding remarks of the work developed in this thesis.

In an attempt to make the content of this thesis self-contained three appendices are included. In Appendix A, the fundamental equations for an incompressible, Newtonian, non-magnetizable, electrically conducting fluid under a magnetic field are obtained. To model the flow driven by the azimuthal Lorentz force in the electromagnetic stirrer, the equations are expressed in the low magnetic Reynolds number approximation considering the electric potential as electromagnetic variable ($\phi-$formulation). Appendix B briefly describes the numerical scheme implemented in the present work. Finally, with the aim of describing the work carried out during a short-term stay at the Osservatorio Astronomico di Cagliari (OAC), in Cagliari, Italy, in Appendix C some classical, textbook problems regarding hyperbolic partial differential equations, which are the equations appearing when modeling astrophysi-

cal flows with MHD included, are presented. This stay was supported by the Italian goverment as part of a Young Investigators Training Program.

Chapter 1

# Experimental setup and observations[‡]

This Chapter describes the experimental observations of the flow produced with an electromagnetic stirrer with cylindrical geometry on top of a permanent magnet with uniform polarity that generates an azimuthal Lorentz force in an electrolyte layer. It starts with a brief description of the experimental device and conditions of interest. Then qualitative observations using a dye tracer are presented for different conditions, particularly, for those in which a hydrodynamic instability arises. These observations are summarized by means of a map of qualitative behavior. Observations using an array of concentric cylindrical magnets of opposite polarity are also analyzed. PIV measurements made at the free surface are presented and discussed. In both magnetic field configurations thermographic images that allow to visualize the temperature field distribution in the flow are presented.

## 1.1 Description of the experimental setup

The electromagnetic stirrer consists of an open cylindrical cavity of 85.7 mm in diameter and 19.4 mm in depth made of acrylic. Two copper electrodes are placed inside the cavity, one is made from a thin sheet which is wrapped around the inner wall of the cavity, while the second can be set in any of two different configurations: a concentric cylinder (Configuration I, see Fig. 1.1) or a coin embedded at the bottom of the cavity (Configuration II), both with a diameter of 25.4 mm, so that, the gap between the electrodes is 30.15 mm. The electrodes are connected to a source of DC current and, to close the electrical circuit, the cavity is filled up to a certain

[‡]Part of this chapter was published in Pérez-Barrera *et al.* (2015), *Instability of electrolyte flow driven by an azimuthal Lorentz force.* **Magnetohydrodynamics**, Vol. 51, pp. 203-210.

height, $h$, with a weakly conducting fluid consisting of an aqueous solution of Sodium Bicarbonate ($NaHCO_3$) 8% by weight so that a radial current circulates in the electrolyte. Underneath the acrylic container a ferrite bar magnet (152.4 mm×101.6 mm×25.4 mm) is placed in such a way that the main component of the magnetic field is perpendicular to the circular section of the cavity and covers the whole flow region. The reference value of the magnetic field at the corner where the acrylic bottom meets the inner electrode is 60 mT (see Fig. 1.1).

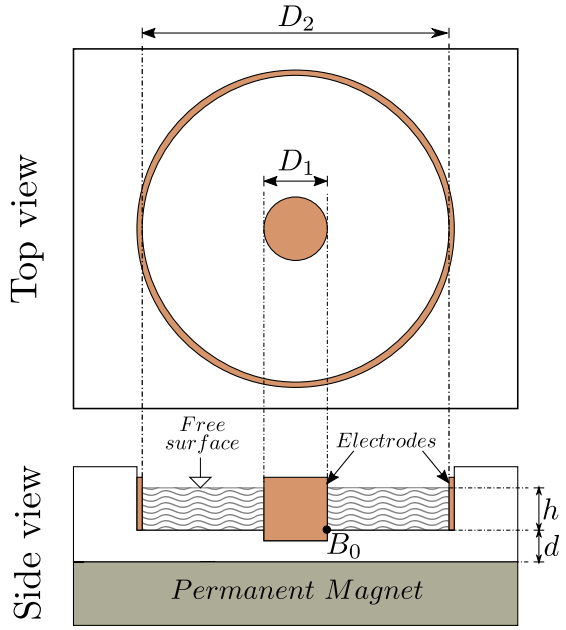


Figure 1.1: Sketch of the experimental setup depicting the electromagnetic stirrer with concentric cylinders as electrodes (Configuration I). The inner and outer diameters of the electrodes are $D_1 = 25.4$ mm and $D_2 = 85.7$ mm, respectively, so that the gap between them is $L = 30.15$ mm. The thickness of the electrolyte layer, $h$, varies form 2.5 mm to 10 mm, while $d = 6$ mm is the distance between the surface of the magnet and the bottom of the cavity. $B_0 = 60$ mT is a reference value for the magnetic field taken at the bottom of the cavity at the interface between the outer electrode and the fluid (black point).

When an electric potential difference is held between the electrodes, a radial electric current travels through the conducting fluid from one electrode to the other. The interaction of the radial current and the axial magnetic field generates a body force, termed *Lorentz force*, which sets the fluid into azimuthal motion. The sense of

rotation of the fluid depends on the direction of the current and the polarity of the magnetic field according to the right-hand rule (see Fig. 1.2).

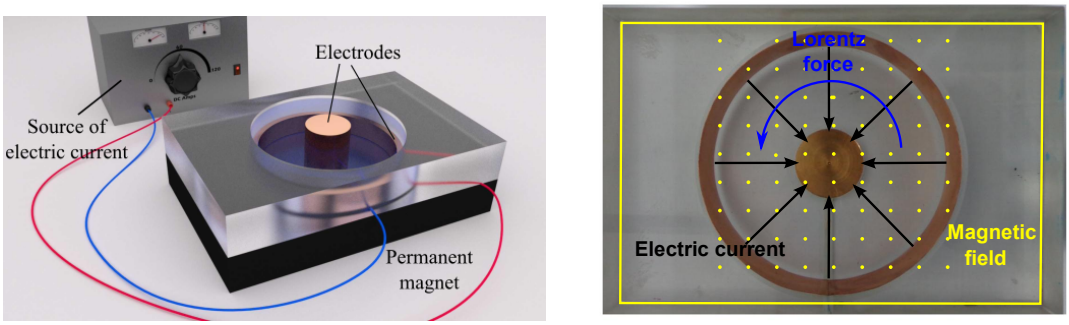


**(a)** **(b)**

Figure 1.2: Perspective view of the experimental setup. ($a$) The electrodes are connected to a source of electric current and the gap between the electrodes is filled with the electrolyte solution, thus closing the electrical circuit. ($b$) The interaction of the radial electric current (black arrows) and the applied magnetic field whose main component points out of the plane (yellow points) generates a Lorentz force (blue arrow) in the azimuthal counterclockwise direction.

In order to do a systematic study of the flows observed in the experimental device, the geometry, magnetic field distribution and fluid properties were fixed. This means that the two parameters that can be varied freely (control parameters) are the applied electric current $I_0$ and the thickness of the electrolyte layer $h$. The experimental procedure was as follows: once the control parameters were defined, the thickness of the electrolyte layer was fixed at a certain value and a steady DC current was injected through it. The electrolyte was at rest at the beginning of the experiment. In order to visualize the flow patterns appearing at the free surface, a blob of edible dye was dropped before the injection of the current. A camera placed above the device allowed to record the flow evolution as function of time. The experiments were carried out from one up to three minutes, mostly because the electrolysis in the fluid produced many bubbles which could affect the flow dynamics and it also diminishes the electrical conductivity of the electrolyte as time passes. This methodology was repeated varying the electric current from 50 mA up to 300 mA using a 50 mA step. The depth of the electrolyte layer was varied from 2.5 mm up to 10 mm with steps of 2.5 mm. Table 1.1 summarizes the experimental conditions of interest for the present work.

Table 1.1: Experimental conditions used in this work.

| Experimental parameter | Value |
|---|---|
| Inner electrode diameter, $D_1$ | 25.4 mm |
| Outer electrode diameter, $D_2$ | 80.57 mm |
| Gap between electrodes, $L$ | 30.15 mm |
| Dimensions of the magnet | $15.24\times10.16\times2.54$ cm$^3$ |
| Reference magnetic field, $B_0$ | 60 mT |
| Conductivity of electrolyte, $\sigma$ | 6.98 $(\Omega\text{m})^{-1}$ |
| Conductivity of copper electrodes, $\sigma_{Cu}$ | $5.7\times10^7$ $(\Omega\text{m})^{-1}$ |
| Mass density of electrolyte, $\rho$ | 1086 kg/m$^3$ |
| Kinematic viscosity of electrolyte, $\nu$ | $1\times10^{-6}$ m$^2/s$ |
| Electrolyte layer thickness, $h$ | 2.5 mm - 10 mm |
| Applied electric current, $I_0$ | 50 mA - 300 mA |

## 1.2 Experimental observations with dye tracer

At the beginning of the experiment, the fluid (originally at rest) starts moving in the same direction as that of the azimuthal Lorentz force (clockwise or counterclockwise) and, depending on the value of the applied electric current and thickness of the fluid layer, different flow patterns can be observed. If the applied current is small (around 50 mA) then the fluid just rotates in the azimuthal direction for all layer thicknesses explored. As time progresses, the tracer develops a spiral revealing that the azimuthal component of the velocity field is dependent of the radial position. Figure 1.3 shows the flow evolution revealed by the tracer at different times for the concentric cylinders configuration with $h = 7.5$ mm and $I_0 = 50$ mA. The electric current flows radially inwards whereas the magnetic field points away from the plane of the page, thus producing a counterclockwise flow.

When the applied electric current exceeds certain critical value, the initial azimuthal flow destabilizes and several travelling vortices appear. These kind of vortices are known as *anticyclonic vortices* due to the fact that their rotation is opposite to that of the bulk motion [Marcus (1990), Bracco *et al.* (1999)]. Figure 1.4 shows the flow evolution at different times for configuration I for an applied electric current of $I_0 =$ 150 mA and an electrolyte layer thickness of $h = 7.5$ mm. For these experimental conditions the bulk motion is counterclockwise whereas the vortices spin clockwise. Here, eight vortices can be clearly seen. As it is shown in the numerical simulations presented in Chapter 4, the non-homogeneous magnetic field distribution produced

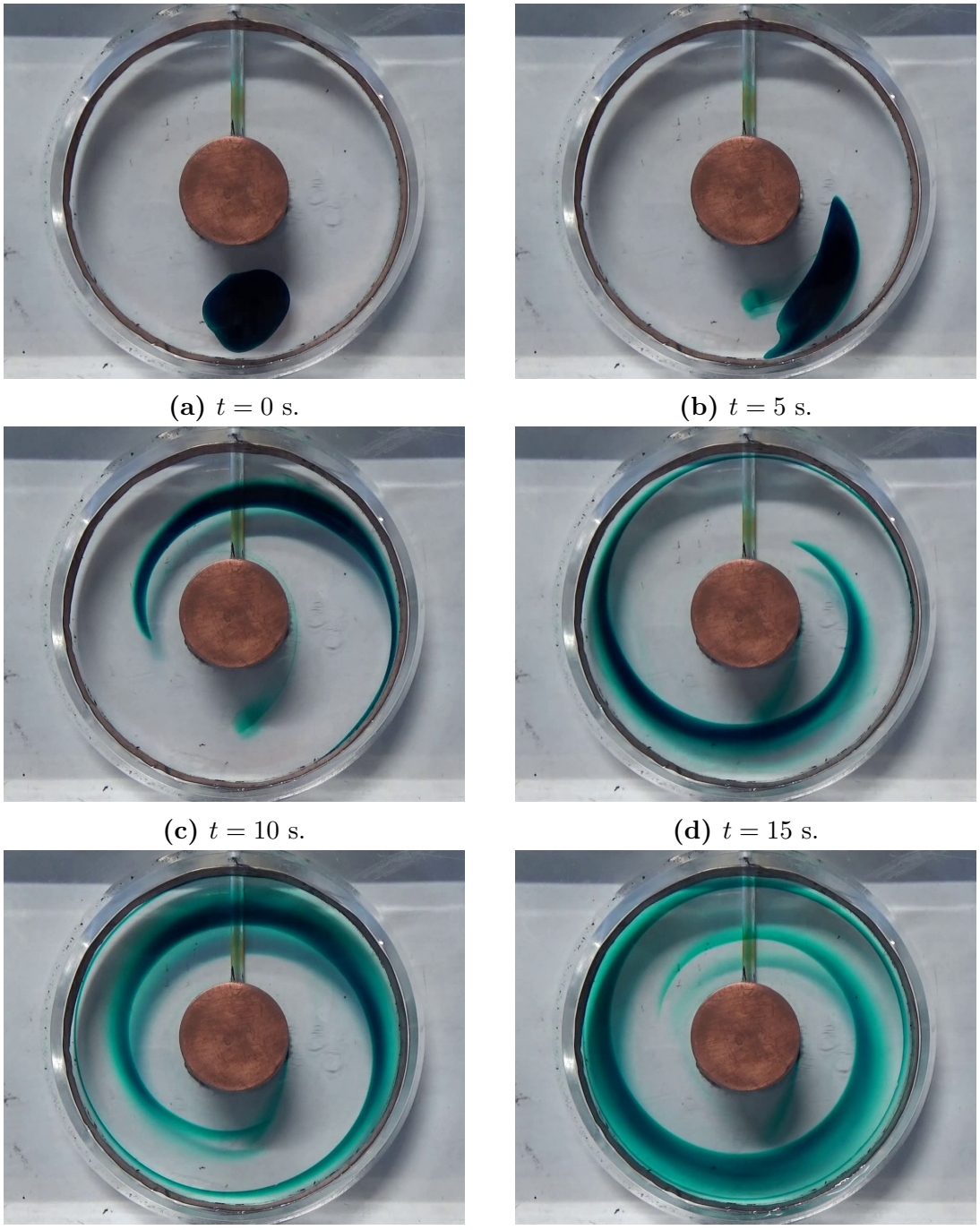

**(a)** $t = 0$ s. **(b)** $t = 5$ s.

**(c)** $t = 10$ s. **(d)** $t = 15$ s.

**(e)** $t = 20$ s. **(f)** $t = 25$ s.

Figure 1.3: Flow evolution for configuration I for $h = 7.5$ mm and $I_0 = 50$ mA. The flow starts from rest ($a$) and when the Lorentz force is applied, it moves in the azimuthal direction ($b$-$c$) so that the tracer forms a spiral as time progresses ($d$-$f$).

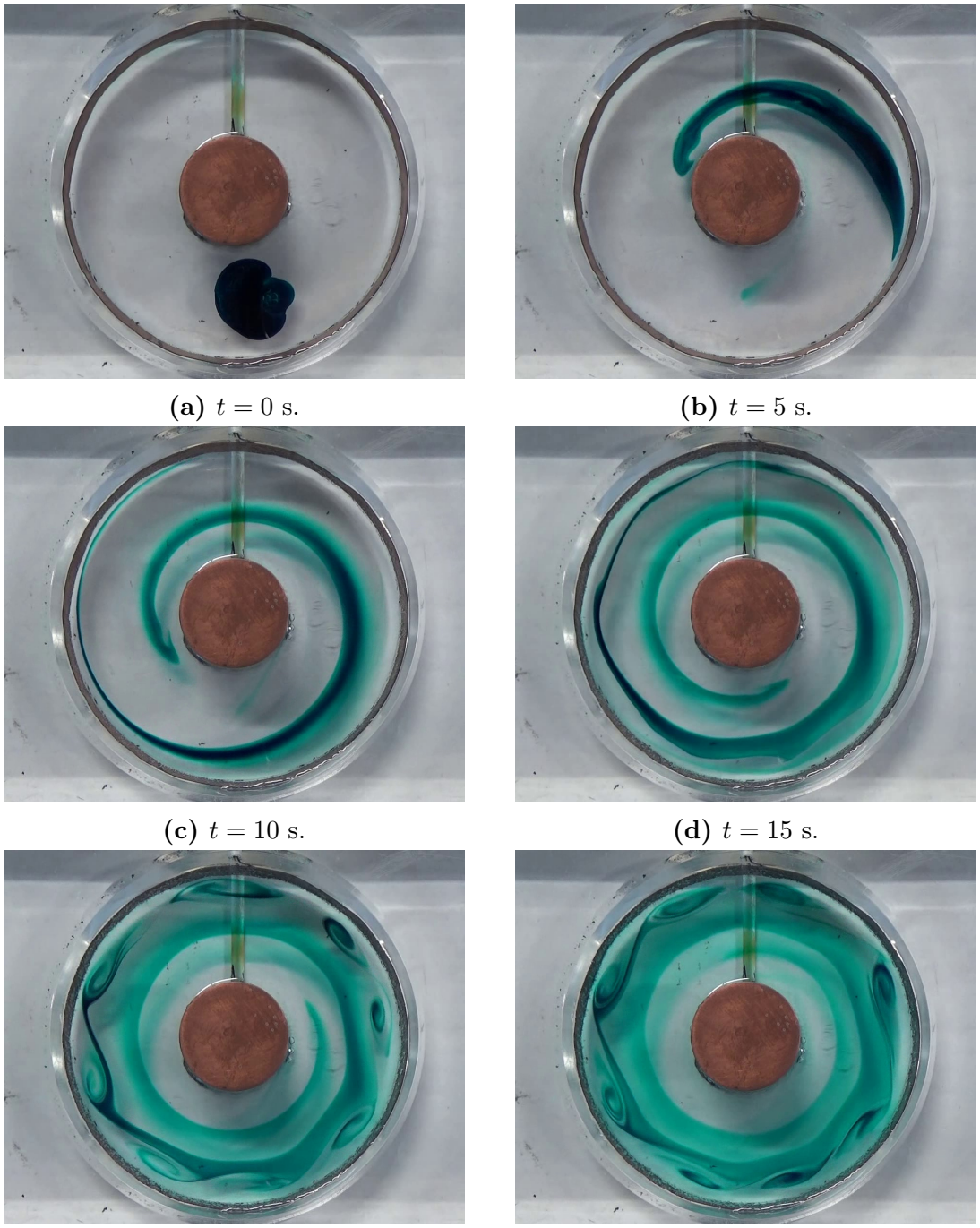

**(a)** $t = 0$ s. **(b)** $t = 5$ s.

**(c)** $t = 10$ s. **(d)** $t = 15$ s.

**(e)** $t = 20$ s. **(f)** $t = 25$ s.

Figure 1.4: Flow evolution for configuration I with $h = 7.5$ mm and $I_0 = 150$ mA. The flow starts from rest ($a$) and when the Lorentz force is applied it drives an azimuthal flow that leads the tracer to form a spiral ($b$-$c$). Eventually, the flow destabilizes ($d$) and serveral travelling anticyclonic vortices appear ($e$-$f$).

by the permanent magnet seems to be very important in determining the appearance of the instability and the number of vortices observed with different experimental conditions. If the sense of rotation of the bulk is changed (either by changing the direction of the injected current or the polarity of the magnetic field), the rotation of the vortices is also changed in such a way that they remain anticyclonic. The vortices are approximately equidistant and once they appear, they remain for long periods of time. The number of observed vortices varies from 4 up to 11 depending on the experimental conditions (applied electric current and electrolyte layer thickness). The instability was observed to appear in both configurations I and II.

To illustrate different flow patterns observed, Fig. 1.5 shows four cases with different number of vortices found with distinct experimental conditions. In all cases, vortices are observed near the outer electrode regardless of the inner electrode configuration and the directon of the electric current. In dimensionless terms, two governing parameters were defined, namely, the aspect ratio $h/L$, that is, the ratio of the layer thickness to the gap between the outer and inner electrodes, and the applied electric parameter $I_0/I_{max}$, where $I_{max}$ is the maxmimum applied current. From the variation of these quantities, it is possible to find the critical parameters for the occurrence of the instability. In what follows, only results for configuration I are presented, but similar results were found for the other configuration.

All experiments correspond to small aspect ratios ($0.1 \leq h/L < 0.4$). For the smallest value, the bottom friction inhibits the appearance of the instability in a larger range of applied current, where a purely azimuthal flow was observed. In fact, the smaller the layer thickness, the larger the current intensity required for the onset of the instability. As the aspect ratio incresases, the current density required for the emergence of vortices diminishes. These observations are summarized in Table 1.2, where the number of vortices originated by the instability in configuration I is presented for different experimental conditions.

The map of qualitative behavior for configuration I presented in Fig. 1.6 identifies the region where outer anticyclonic vortices are formed for the given aspect ratio and electric current parameter.

To illustrate the flow created by an imposed shearing force, the configuration with a magnetic field distribution with an abrupt change in polariry was used. This flow was explored using the experimental device with the central electrode embedded in the bottom wall (Configuration II), placed on top of two cylindrical concentric ring magnets with opposite polarities whose inner and outer diameters are 9.4 mm and 31.6 mm for the inner magnet, and 33.3 mm and 86 mm for the outer one, respec-

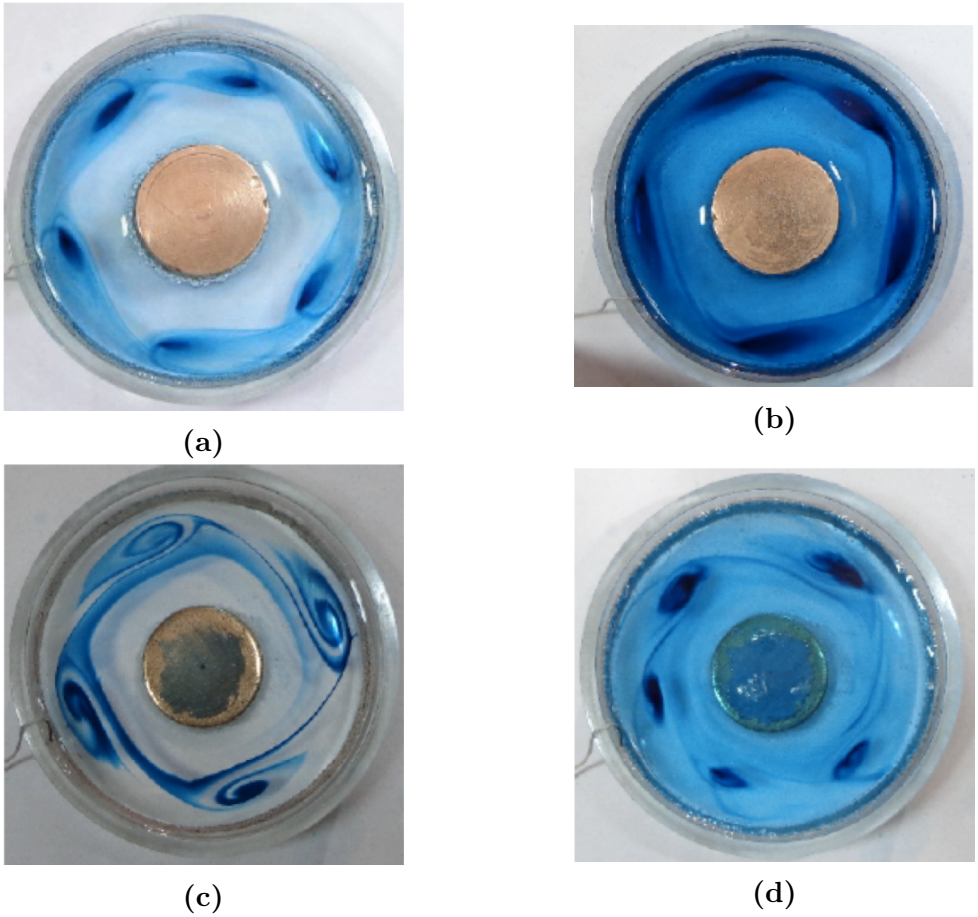

**(a)** **(b)**

**(c)** **(d)**

Figure 1.5: Dye visualization of the instability observed for a layer thickness of 10 mm. *a*) and *b*) correspond to configuration I. *c*) and *d*) correspond to configuration II. The current density for *a*) and *c*) is 100 mA, and for *b*) and *d*) is 300 mA.

Table 1.2: Experimental results for configuration I.

| $h$ [mm] | $h/L$ | $I_0$ [mA] | $I_0/I_{max}$ | No. of outer vortices |
|---|---|---|---|---|
| 10 | 0.39 | 25-50 | 0.062-0.125 | 0 |
| 10 | 0.39 | 75-100 | 0.187-0.250 | 5 |
| 10 | 0.39 | 125-400 | 0.312-1.0 | 6 |
| 7.5 | 0.29 | 25-50 | 0.062-0.125 | 0 |
| 7.5 | 0.29 | 75-100 | 0.187-0.250 | 5, 6 |
| 7.5 | 0.29 | 125-400 | 0.312-1.0 | 5, 6, 7 |
| 5.0 | 0.19 | 25-180 | 0.062-0.450 | 0 |
| 5.0 | 0.19 | 190-400 | 0.475-1.0 | 8, 10, 11 |
| 2.5 | 0.10 | 25-250 | 0.062-0.625 | 0 |
| 2.5 | 0.10 | 275-400 | 0.6875-1.0 | 11 |

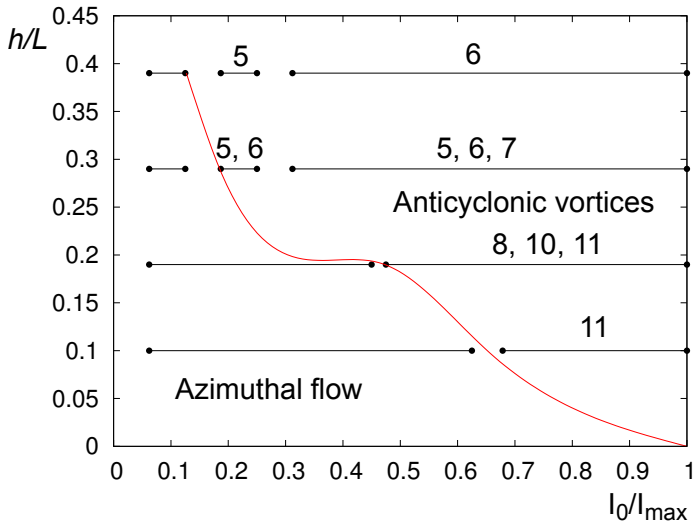


Figure 1.6: Experimental map of qualitative behavior for configuration I. The curved, red line marks the treshold where external anticyclonic vortices are formed for the given aspect ratio ($h/L$) and applied current parameter ($I_0/I_{max}$). The number on top of the intervals indicate the number of vortices observed for the corresponding conditions.

tively. In this way, the inner magnet exceeded the diameter of the central electrode by 6.2 mm, while the external magnet covered completely the flow domain. This configuration of magnetic field generates a Lorentz force in two opposite directions, thus rendering a shearing flow inside the flow region. As it was mentioned in the Introduction, the flow created in this manner has been extensively studied, most notably by Soviet and Russian researchers [Bondarenko & Gak (1978), Dovzhenko *et al.* (1979), Ponomarev (1980), Dovzhenko *et al.* (1981), Krymov (1989), Manin (1989), Gledzer *et al.* (2013)], since the generated flow patterns resemble atmospheric phenomena. Figure 1.7 shows the observed flow patterns at different times for an applied electric current $I_0 = 150$ mA and an electrolyte layer thickness $h = 5$ mm using the coin-shaped inner electrode. It can be observed the formation of a tripolar vortex similar to those previously reported for hydrodynamic flows [see, for instance, Van Heijst *et al.* (1991), Samimy *et al.* (2003)].

Starting from rest, when the electrical current is turned on the shearing flow starts developing and two large vortices form and rotate very slowly in the counter-clockwise direction whereas a third vortex (constrained by the other two) remains at the center of the container (see Fig. 1.7).

## 1.3 PIV results

In order to obtain quantitative information of the flow field, Particle Image Velocimetry measurements were performed. For that end, neutrally bouyant, 10 mm in diameter, silver-covered, glass spheres were colocated in the electrolyte solution to trace the fluid motion. Illumination of the free surface was achieved by means of a laser sheet. To guarantee that the analyzed plane of flow corresponds mainly to the free surface, PIV measurements were made using only previously selected tracers. First, the tracers were centrifuged and only those that remained on the free surface were selected. Using a videocamera, the motion of the spheres located at the free surface was recorded and analyzed to obtain quantitative information of the flow.

Consistently with the dye tracer visualizations, the PIV analyses revealed that an almost purely azimuthal flow ocurred in the cases where the instability did not develop, corresponding to low applied electric current intensities. For all the subsequent results, the experiments were one minute long. This duration was chosen considering that the time interval was enough for the flow to reach either steady-state or a well developed instability. Also, for longer time intervals the electrolysis of the solution drastically changes the electrical properties of the electrolyte and many bubbles are

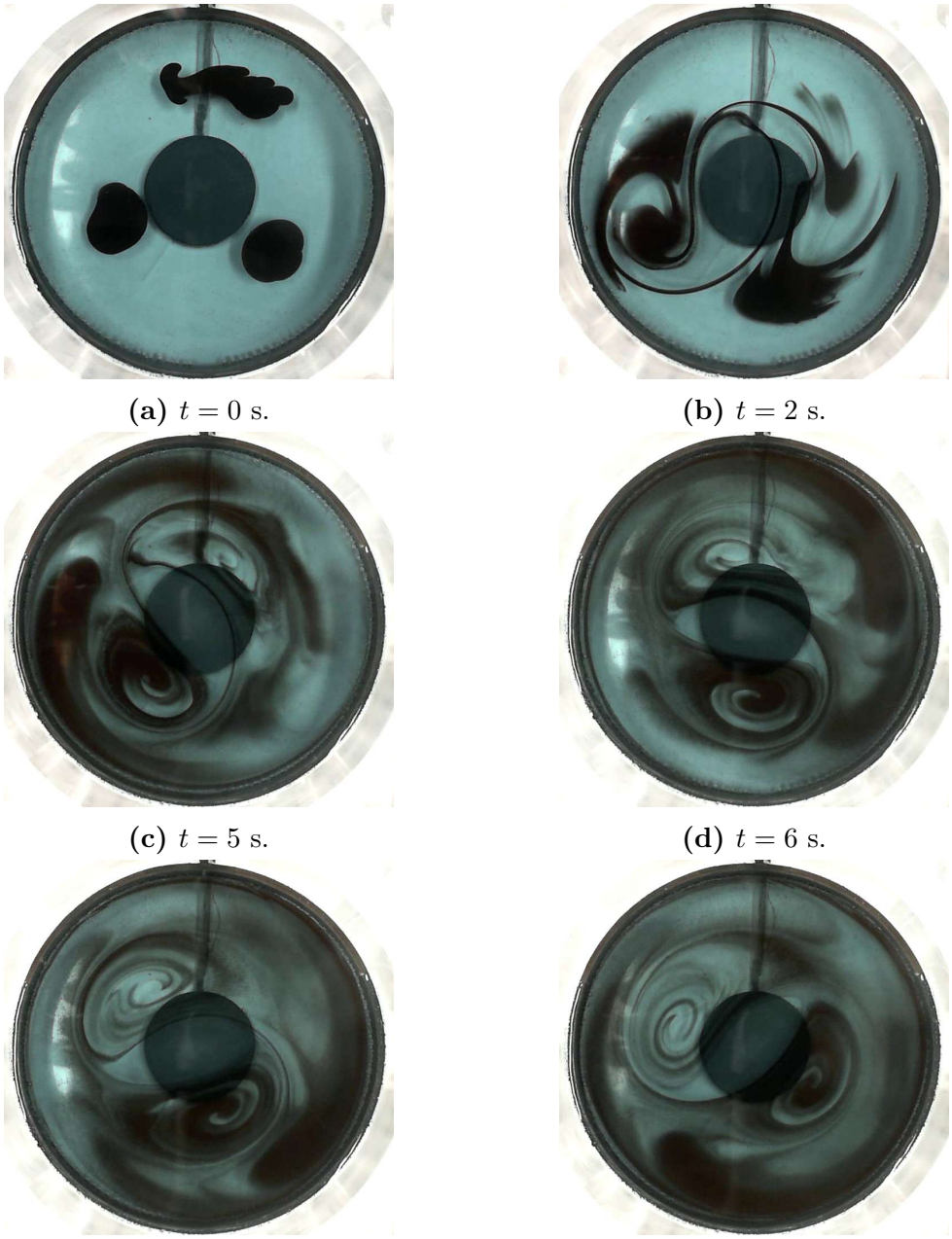

**(a)** $t = 0$ s. **(b)** $t = 2$ s.

**(c)** $t = 5$ s. **(d)** $t = 6$ s.

**(e)** $t = 6.5$ s. **(f)** $t = 7$ s.

Figure 1.7: Experimental flow observed for an array of two cylindrical concentric magnets with opposite polarities. *a*) Initial distribution of the tracer. *b*) Formation of two large vortices which constraint the thrid central vortex. $c) - f)$ The two large vortices travel slowly counter-clockwise.

formed at the electrodes, affecting the flow dynamics. Figure 1.8a) shows the steady-state PIV velocity field at the free surface of a 5 mm thick electrolyte layer when an applied electric current of 50 mA is applied. The existence of an almost purely azimuthal motion can be corroborated in Fig. 1.8b), where the azimuthal velocity component at a radial position $r = 3.1$ cm is plotted as a function of time. Starting from rest, a linear growth of this component can be observed for small times (less than 10 s), then the growth becomes slower to finally get to a steady-state flow, as evidenced by the fact that the azimuthal component reaches a terminal value of about 2.05 cm/s.

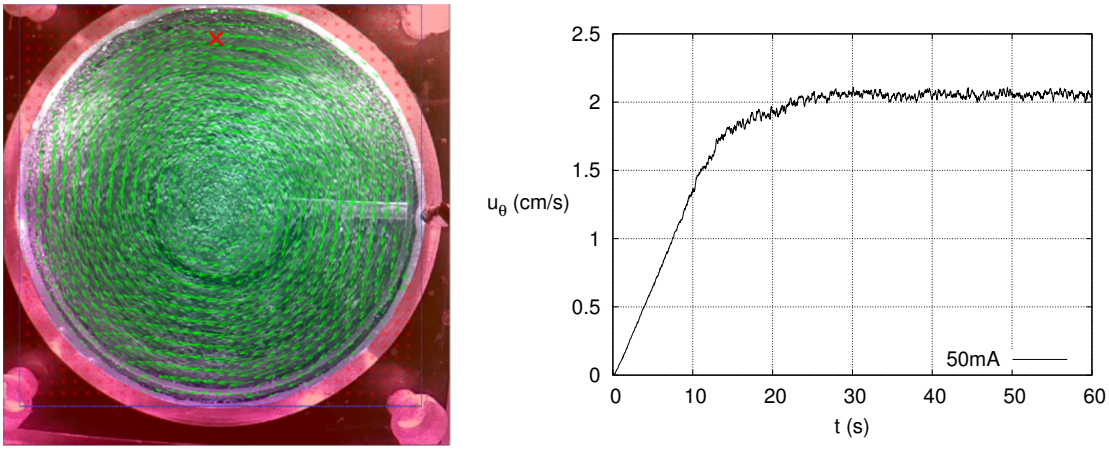


**(a)** **(b)**

Figure 1.8: PIV results for a purely azimuthal flow. *a*) Velocity field for the steady flow. *b*) Azimuthal component as function of time at $r = 3.1$ cm and $\theta = 90°$ (red cross). $I_0 = 50$ mA and $h = 5$ mm.

As it was shown with the dye tracer results, increasing the intensity of the applied electric current triggers the appearance of the instability of the flow. Even though this instability was clearly seen with the tracers used for PIV, after processing the videos it was found that the PIV toolkit was not capable of capturing the structure of the anticyclonic vortices. Figure 1.9 shows the calculated velocity fields at the free surface for an applied electric current of 150 mA at different instants of time. When the flow starts developing, a purely azimuthal flow is observed, which is nicely capturated by the PIV technique but, as the flow destabilizes and the anticyclonic vortices appear, it is very clear that the measurements are not good anymore. The right part of the images has a lot of noise because of the conduit drilled in the container in order to connect the central electrode to the power source. Besides this

detail, the presence of the vortices is not observed in the velocity field. This might be due to the lack of tracers in the electrolyte, which are agglomerated by the vortices, thus resulting in regions where no tracers can be used to calculate the local velocities, as can be appreciated in Figs. 1.9c) and 1.9d). Another possible explanation for the absence of vortices in the velocity field is the difference between the two scales of velocity involved in the experiments, that is, the bulk azimuthal velocity and the smaller velocity associated to the anticyclonic vortices. This difference in the scales of velocity implies that two different spatial PIV resolutions are needed to capture either the azimuthal flow or the anticyclonic vortices.

Since the PIV technique uses only one spatial resolution at a time, only the azimuthal flow can be calculated properly. Even though it is not possible to capture the instability with this technique, the PIV measurements of the azimuthal flow can be used to validate the performed numerical simulations described in Chapter 4 of this thesis. Figure 1.10 shows the measured azimuthal velocity as a function of time for an applied electric current of 150 mA at two different radial positions (red crosses in Fig. 1.9a) and $\theta = 90°$. It can be observed that the velocity near the outer electrode where vortices appear ($r = 3.1$ cm) is not calculated properly, whereas the mainly azimuthal flow far away from the vortices ($r = 2.02$ cm) is well resolved reaching approximately a terminal value.

It is worth mentioning that these difficulties using the PIV technique led us to try to improve the measurement technique in order to capture the observed flow instability. The idea behind this improvement is to *reduce* the azimuthal flow, this can be done by taking the PIV measurements in a reference frame rotating at the mean translational velocity of the vortices. In this way the vortices remain at the same position when observed from the laboratory reference frame. There are at least two ways to achieve this effect, one is to rotate the camera with a constant angular velocity while recording the experiments and processing the images with the traditional PIV technique; the second one is to record the videos with the camera fixed and then pre-process the images by rotating them with certain angular velocity. As this technique is currently being developed, only preliminary results using the pre-processing of the recorded images are presented next.

Figure 1.11 shows four images obtained with the improved technique for an applied current of 150 mA at different instants of time. The mean translastional velocity of the vortices was selected from the previously obtained PIV data taking the azimuthal velocity at the radial position where the vortices are present. It can be clearly noticed that the images are rotated as time progresses, nevertheless, the vortices remain at the same position. With respect to the first image, the other three are rotated in

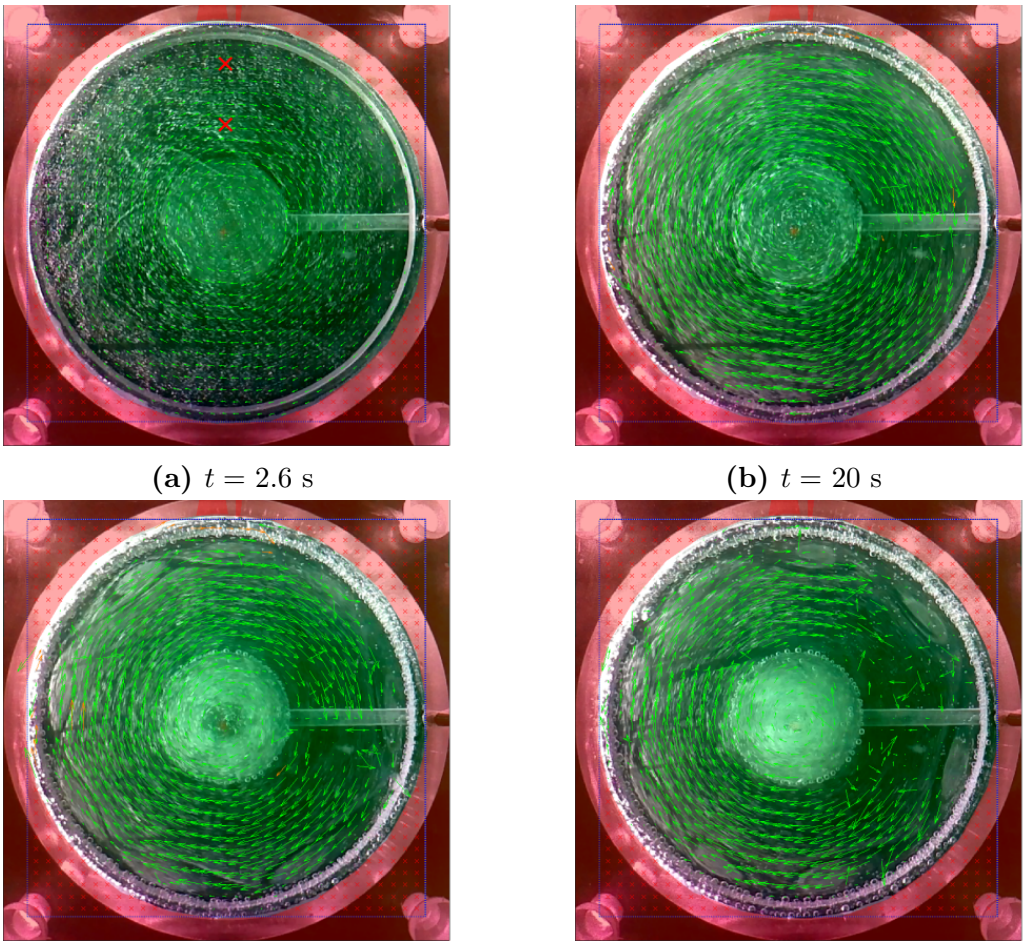

**(a)** $t = 2.6$ s **(b)** $t = 20$ s

**(c)** $t = 40$ s **(d)** $t = 60$ s

Figure 1.9: Velocity fields measured with traditional PIV procedure at different instants for $I_0 = 150$ mA, $h = 5$ mm. First, the azimuthal flow develops ($a$), giving rise to the appearance of the instability ($b$), and eventually to the formation of anticyclonic vortices, ($c$ and $d$). However, the PIV is not able to capture them.

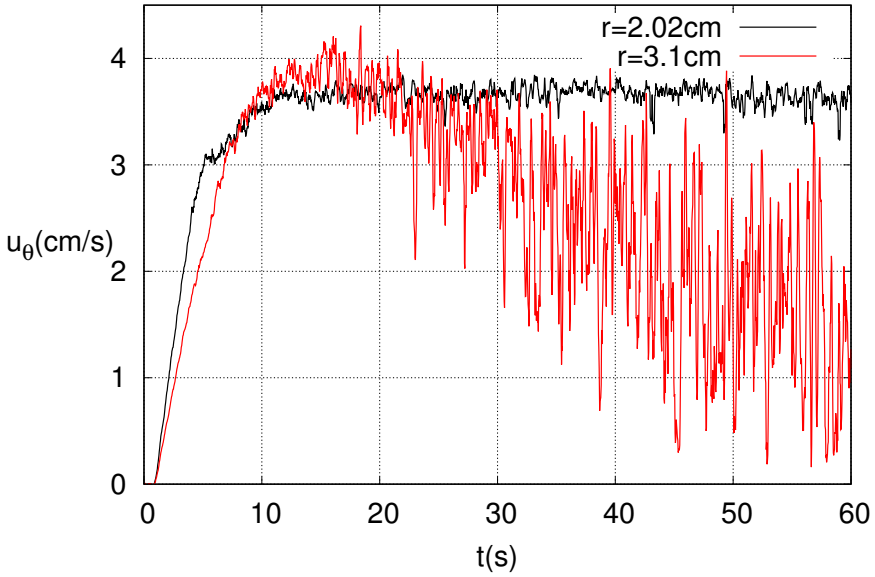


Figure 1.10: Azimuthal velocity component as a function of time for two distinct radial positions. Near the outer electrode ($r = 3.1$ cm), where anticyclonic vortices are present, the azimuthal component is not well calculated showing large fluctuations in very short periods of time and reaching almost null velocities (red line). Far from the outer cylinder ($r = 2.02$ cm) the flow is almost azimuthal so the velocity component is much better calculated (black line).

45° increments. The time interval between two images is about 0.7 s. It is worth noting that this procedure was only applied once the instability was well developed. The developing flow in the early stages is mainly azimuthal and it is well captured by the traditional PIV technique.

Having fixed the vortices, the PIV processing was applied. Figure 1.12 displays the same four images shown in Fig. 1.11 after PIV processing. As it was shown previously, the conduit to connect the inner electrode causes a lot of noise in the neighborhood region, nevertheless, away from it the structure of the vortices and their velocity field can be appreciated. This example shows that this methodology has the potential to allow the quantitative analysis of the observed vortices although there are still some issues that must be addressed. For instance, the proper choice of the angular velocity to rotate the images and the way to avoid the noise introduced by conduit at the bottom of the container. Currently this work is in progess and it is expected to submit it soon to an specialized journal.

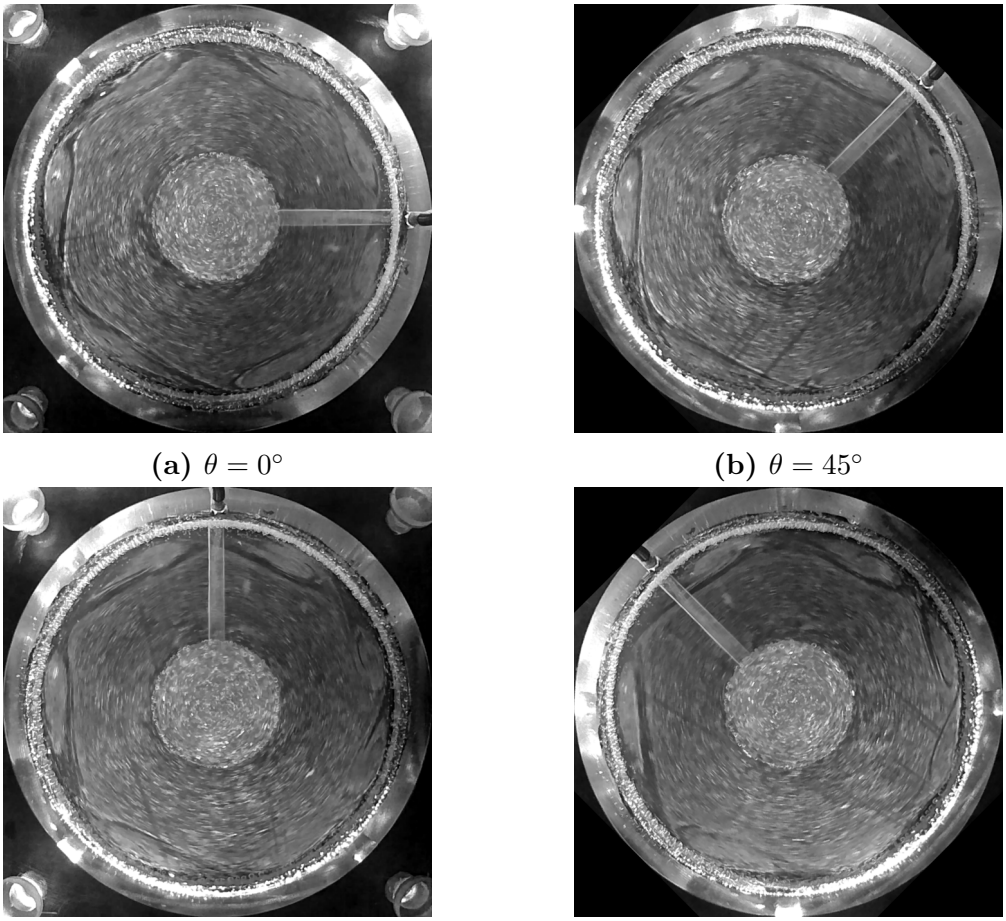

**(a)** $\theta = 0°$ **(b)** $\theta = 45°$

**(c)** $\theta = 90°$ **(d)** $\theta = 135°$

Figure 1.11: Images corresponding to different time instants for an applied electric current of 150 mA and an electrolyte layer thickness of 5 mm. With respect to *a*) the images are rotated by 45° increments. It can be appreciated that the vortices remain at fixed positions due to the change of reference frame.

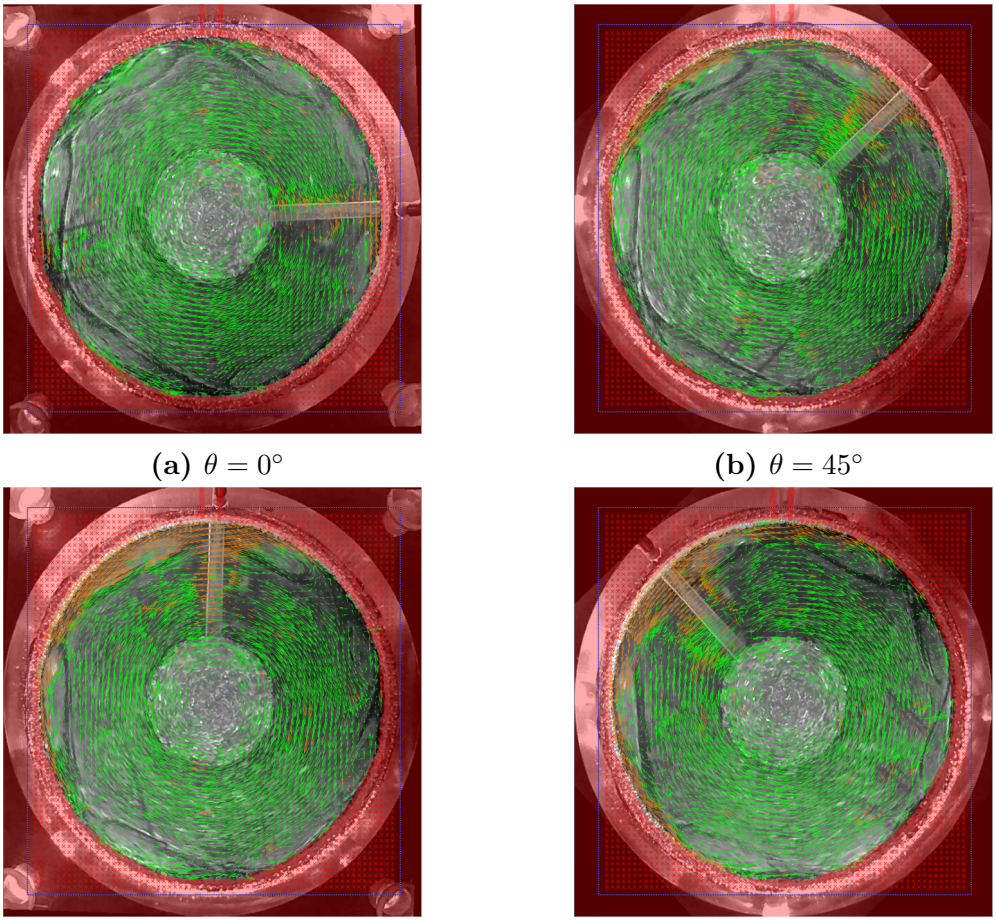

**(a)** $\theta = 0°$ **(b)** $\theta = 45°$

**(c)** $\theta = 90°$ **(d)** $\theta = 135°$

Figure 1.12: PIV processing of the rotated images shown in the previous figure. It can be seen the noise created by the conduit drilled to close the electrical circuit. However, away from that region, the velocity field of the vortices is resolved.

## 1.4 Visualizations using thermographic images

With the aim of complementing the experimental information obtained with dye visualization and PIV, several experiments in which the flow was visualized by means of images obtained with a thermographic camera, recently acquired at the Renewable Energy Institute, were carried out. In order to perform this kind of experiments, the electrolyte solution was heated up to around $60°C$ and quickly poured into the stirrer. Due to the temperature differences between the electrolyte and the cylindrical cavity and mainly with the environment, an intense heat transfer is established that leads to a time-dependent temperature distribution registered by the thermographic camera. The camera used for these experiments is a *FLIR x6540sc* which has a spatial resolution of $640 \times 512$ pixels and is capable of detecting temperature differences of 20 mK. Since even slight temperature differences can be detected, thermographic images can, in principle, be used to identify different flow structures which determine the heat transfer characteristics. These experiments were also carried out using the two different magnetic field configurations employed previously, namely, a single bar magnet with uniform polarity and two concentric cylindrical magnets with opposite polarities.

Figure 1.13 shows the temperature distribution observed at different times in an electrolyte layer thickness of 5 mm and an applied electric current of 200 mA using the single permanent bar magnet. Initially, the fluid is at rest, then the Lorentz force is applied and the fluid starts moving in the azimuthal clockwise direction. After some time, the flow destabilizes and several anticyclonic vortices are formed, which remain rotating for long periods of time. It is remarkable that, for the long-time behavior, eight anticyclonic vortices can be clearly observed very close to the outer electrode, as ocurred in the isothermal flow. In fact, the flow is very similar to the one observed using the dye tracer described in the previous sections. As a matter of fact, the temperature differences do not seem to inhibit nor greatly alter the emergence of the instability.

Figure 1.14 shows the temperature distribution, at different times, for a shearing flow generated by two concentric, cylindrical magnets with opposite polarities, using an applied current of 150 mA, where a complex pattern can be appreciated. Note that there are also small vortices near the outer electrode that could not be observed just using the dye tracer. This points out to the possibility that heat transfer plays an important role in the observed dynamics for these experimental conditions. From the described experiments, it is clear that the temperature distribution in the electrolyte can be used to visualize the flow dynamics in non-isothermal magnet-

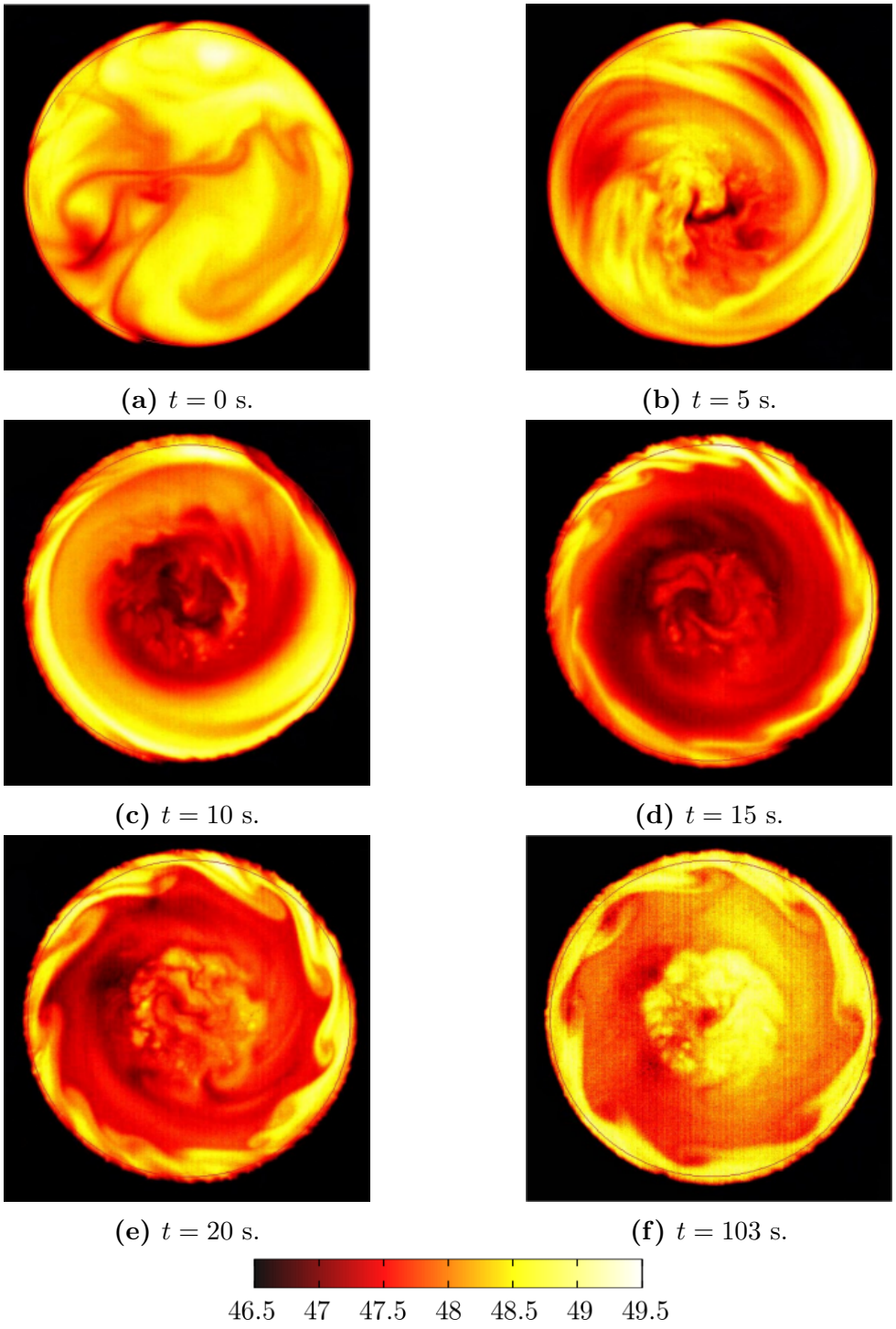


**(a)** $t = 0$ s. **(b)** $t = 5$ s.

**(c)** $t = 10$ s. **(d)** $t = 15$ s.

**(e)** $t = 20$ s. **(f)** $t = 103$ s.

Figure 1.13: Temperature distribution at different times for $h = 5$ mm and $I_0 = 200$ mA using a single bar magnet. *a*) The fluid is at rest and then (*b*-*c*) it starts moving in the azimuthal direction. *d*) The flow destabilizes and *e*) several travelling vortices appear. *f*) The vortices keep rotating for long periods of time.

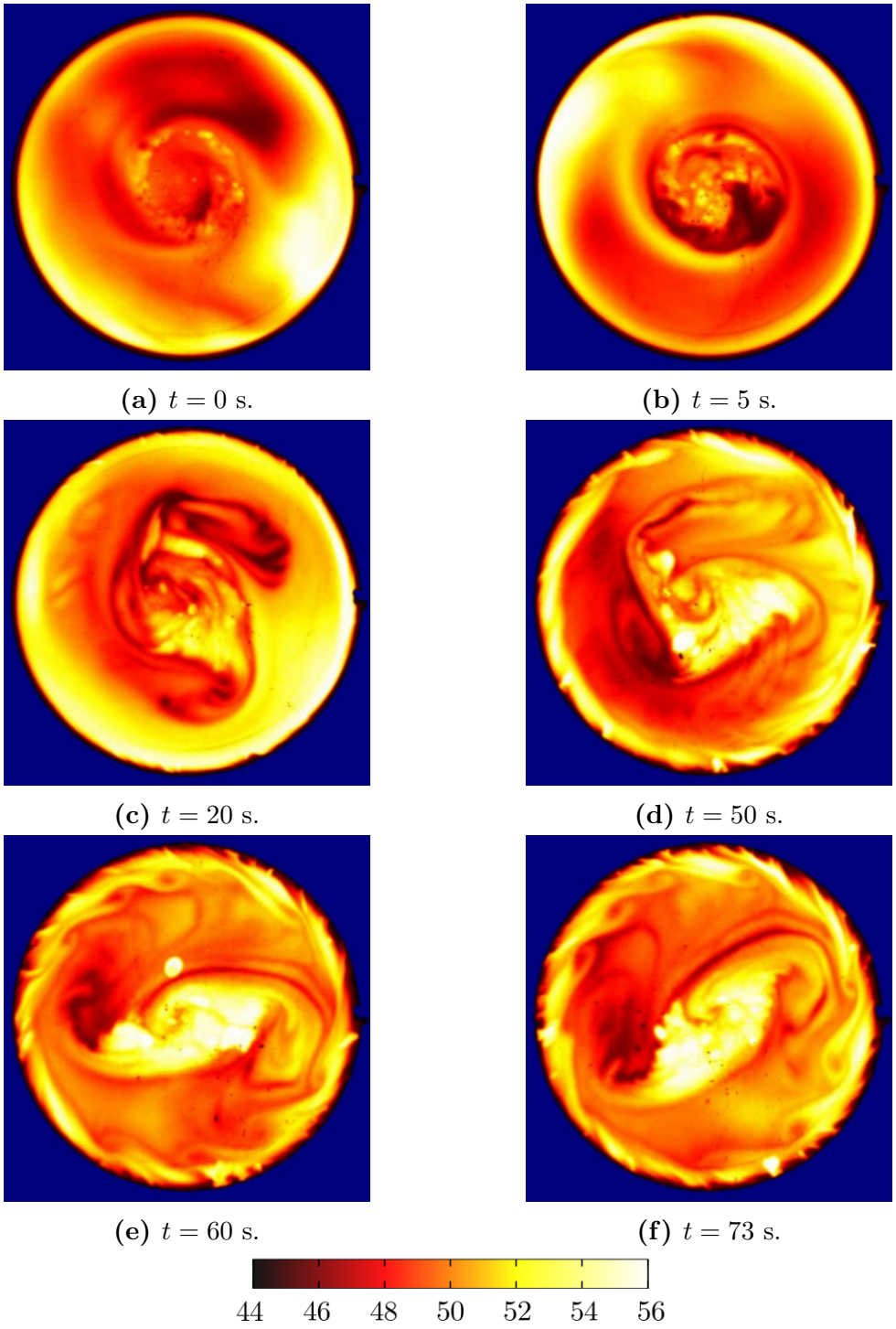


**(a)** $t = 0$ s. **(b)** $t = 5$ s.

**(c)** $t = 20$ s. **(d)** $t = 50$ s.

**(e)** $t = 60$ s. **(f)** $t = 73$ s.

Figure 1.14: Temperature distribution at different times for $h = 5$ mm and $I_0 = 150$ mA using two concentric cylindrical magnets with inverted polarity. *a*) The fluid is at rest and then (*b*-*c*) it starts moving in the azimuthal direction due to the shearing force. *d*) The flow destabilizes and *e*) a central structure with several outer vortices appears. *f*) The structure keeps rotating.

ically driven flows at laboratory scale. However, the impact of the heat transfer in the flow dynamics must be determined accurately in the future. So far, in the preliminary experiments performed in this work there are cases in which the heat transfer does not seem to affect (at least qualitatively) the flow dynamics, while in other cases temperature gradients drastically affect the observed flow patterns. In any case, the use of thermographic information opens new interesting possibilities for future experimental studies as well as the numerical analysis of non-isothermal electromagnetically driven flows.

Chapter 2

# Analytical solutions for the flow inside an annular MHD stirrer[§]

In this chapter, the flow of electrically conducting fluids in an annular MHD stirrer is explored theoretically assuming that the layer of fluid in the annular gap is very thin. A quasi-two-dimensional model that considers a linear friction due to the boundary layer attached to the insulating bottom wall is implemented and analytical solutions for the azimuthal flow are obtained for two different cases. The first corresponds to a high conductivity fluid (a liquid metal) where the electric potential is coupled to the fluid velocity. The second case considers a low conductivity fluid (an electrolyte) where the electric potential is uncoupled from the fluid motion. The effect of slip boundary conditions at the walls of the inner and outer cylinders, as well as the space between them, is explored. This study is partly motivated by microfluidic applications.

## 2.1 Introduction

As it was mentioned in the Introduction of this thesis, the use of electromagnetic forces to control and manipulate electrically conducting fluids in microfluidic devices has observed an increased interest in past years [Bau *et al.* (2003), Qian & Bau (2009)]. In particular, it has been demonstrated that mixing of fluids can be properly accomplished using electromagnetic forces and, with a properly designed MHD stirrer, chaotic advection can substantially enhance mixing efficiency [Yi *et al.* (2002)].

[§]Part of this chapter was published in Pérez-Barrera *et al.* (2016), *Analysis of an annular MHD stirrer for microfluidic applications*, in Springer's series **Recent Advances in Fluid Dynamics with Environmental Applications**, pp. 275 - 288.

This chapter is aimed at searching analytical solutions for electromagnetically driven flows in annular channels. Although in some cases analytical treatments require highly idealized assumptions, conditions imposed in this work are closer to realistic microfluidic flows. Most analytical solutions reported in the literature for electromagnetically driven flows in annular configurations assume that coaxial cylinders are infinite [see, for instance, Gleeson *et al.* (2004), Digilov (2007), Zhao *et al.* (2011), Qin & Bau (2012)]. In this work, we use a quasi-two-dimensional (Q2D) model based on an averaging procedure in the normal direction that considers the presence of the bottom wall which originates either the Hartmann friction for high conductivity fluids [Sommeria (1988), Andreev *et al.* (2001)] or pure viscous friction effects for low conductivity fluids [Satijn *et al.* (2001)]. In addition, given the relevance that slippage may have at microfluidic scale, generalized Navier slip boundary conditions are considered at the lateral walls which mainly determine the dynamic flow behavior [Rivero & Cuevas (2012)]. According to the electrical conductivity of the working fluid, two different cases are treated. The first case corresponds to a liquid metal flow where induction effects cannot be neglected and the equation of motion and that for the electric potential are coupled. In the second case, a solution is sought for a low conductivity fluid, such as an electrolyte, where induction effects are negligible. This implies that the electric potential is uncoupled from the fluid velocity and, therefore, can be determined independently from the equations of motion.

## 2.2 Formulation

As in the device described in Chapter 1 (see Fig. 1.1) we consider a thin layer of fluid with thickness $h$ that lies in the gap between the inner and outer cylinders of radii $R_1$ and $R_2$, respectively, which are assumed to be perfectly conductors. The bottom wall of the annular container is electrically insulated. An electric potential difference $\Delta\phi = \phi_2 - \phi_1$ is applied between the walls of the inner ($\phi_1$) and outer ($\phi_2$) cylinders so that a DC current can circulate radially in the fluid layer. The current interacts with a uniform applied magnetic field of strength $B_0$ parallel to the cylinder's axis, and, therefore, a Lorentz force is produced in the azimuthal direction. As shown in Appendix A, the governing MHD equations in the low magnetic Reynolds number approximation that must be solved to determine the flow in this device are the following:

$$\nabla \cdot \mathbf{u} = 0, \tag{2.1}$$

$$\rho\left(\frac{\partial \mathbf{u}}{\partial t}+(\mathbf{u}\cdot\nabla)\mathbf{u}\right)=-\nabla p+\eta\nabla^2\mathbf{u}+\mathbf{j}\times\mathbf{B}, \tag{2.2}$$

$$\mathbf{j}=\sigma\left(-\nabla\phi+\mathbf{u}\times\mathbf{B}_0\right), \tag{2.3}$$

$$\nabla^2\phi=\nabla\cdot(\mathbf{u}\times\mathbf{B}_0), \tag{2.4}$$

where $\mathbf{u}$, $p$, $\mathbf{B}$, $\mathbf{j}$ and $\phi$ are the velocity, pressure, applied magnetic field, electric current density and electric potential, respectively, while $\rho$, $\eta$ and $\sigma$ are the mass density, kinematic viscosity and electrical conductivity of the fluid, respectively. We now search for solutions of these equations in the quasi-two-dimensional approximation.

## 2.3 Quasi-two-dimensional approximation

Different physical mechanisms may promote the quasi-two-dimensionalization of flows, for instance, the force of gravity in a stratified flow, the Coriolis force in a rotating homogeneous fluid or the surface tension in a soap film. A strong magnetic field acting transversally to insulating walls that confine an MHD flow may also lead to the supression of wall-normal motions. Quasi-two-dimensional (Q2D) flows also occur when a significant geometrical confinement is imposed, as in motions generated in shallow fluid layers, as it may occur in microfluidic applications. This condition is satisfied when the relevant length scale in the plane of the flow is much larger than the thickness of the fluid layer. Due to the supression of the wall-normal motion, the Q2D approach assumes that the transport of momentum in the normal direction is mainly diffusive, as a result, an averaging procedure, where the governing equations are integrated in the normal direction (or along the lines of force when a magnetic field is present) within the thickness of the fluid layer, can be applied. In this way, the problem is formulated in terms of core (averaged) variables while the effect of the boundary layer attached to the bottom of the wall is included through an additional linear term in the momentum equations accounting for the wall friction. In liquid metal flows under strong magnetic fields, Hartmann layers must be considered [Sommeria (1988), Andreev *et al.* (2001)], while in flows of low conductivity fluids (*v. e.* electrolytes) with or without magnetic fields, the viscous boundary layer is the relevant one [Satijn *et al.* (2001)].

In this work, the Q2D approach was used to look for steady laminar azimuthal axisymmetric solutions, that is $\mathbf{u}=u_\theta(r)\hat{\mathbf{e}}_\theta$, where $u_\theta$ and $\hat{\mathbf{e}}_\theta$ are the velocity component and the unit vector in the azimuthal direction, respectively.

In dimensionless form, the governing equations (2.1) - (2.4) expressed in cylindrical coordinates reduce to the following form when the Q2D approach is considered

$$\frac{u_\theta^2}{r+\alpha} = \frac{dp}{dr}, \tag{2.5}$$

$$\frac{d^2u_\theta}{dr^2} + \frac{1}{r+\alpha}\frac{du_\theta}{dr} - \frac{u_\theta}{(r+\alpha)^2} - \frac{Ha}{\varepsilon}u_\theta - j_r = 0, \tag{2.6}$$

$$j_r = -\frac{d\phi}{dr} + Ha^2 u_\theta, \tag{2.7}$$

$$\frac{1}{r+\alpha}\frac{d}{dr}\left((r+\alpha)\frac{d\phi}{dr}\right) = \frac{Ha^2}{r+\alpha}\frac{d}{dr}\left((r+\alpha)u_\theta\right), \tag{2.8}$$

where $u_\theta$, and the pressure, $p$, are normalized by $u_0 = \sigma B_0 \Delta\phi R/\rho\nu$ and $\rho u_0^2$, respectively, with $R = R_2 - R_1$. In turn, the magnetic field is normalized by $B_0$, while the electric current density, $j_r$, is normalized by $\sigma\Delta\phi/R$. The dimensionless radial coordinate, $r$, and electric potential, $\phi$, are defined as $r = (r' - R_1)/R = r'/R - \alpha$ and $\phi = (\phi' - \phi_1)/\Delta\phi$, where $\alpha = R_1/R$, $r'$ and $\phi'$ being the dimensional radial coordinate and electric potential, respectively. Note that the continuity equation (Eq. 2.1) is identically satisfied.

The *Hartmann number* is defined as

$$Ha = B_0 R\sqrt{\frac{\sigma}{\rho\nu}}, \tag{2.9}$$

which estimates the strength of magnetic forces compared with viscous forces. The forth term in Eq. (2.6) is the linear friction that results from the averaging procedure and considers the effect of Hartmann layers in the bottom wall [Sommeria (1988), Andreev *et al.* (2001)], where $\varepsilon = h/R$ is the aspect ratio. In the following sections, analytical solutions for the system of equations (2.5)-(2.8), considering slip boundary conditions for the cases of liquid metal and electrolyte flows, are obtained.

## 2.4 Solution for the liquid metal flow

We first proceed to obtain solutions for the case of a liquid metal flow. Integrating Eq. (2.8) once we obtain

$$\frac{d\phi}{dr} = Ha^2 u_\theta + \frac{C}{r+\alpha}, \tag{2.10}$$

where $C$ is an integration constant. If Eq. (2.10) is substituted into Eq. (2.7) and the result is inserted into Eq. (2.6), it yields

$$\frac{d^2u_\theta}{dr^2}+\frac{1}{r+\alpha}\frac{du_\theta}{dr}-\left(\beta^2+\frac{1}{(r+\alpha)^2}\right)u_\theta=-\frac{C}{r+\alpha}, \tag{2.11}$$

where $\beta^2=Ha/\varepsilon$. Equation (2.6) is a non-homogeneous Bessel equation and has to satisfy the general slip boundary conditions at the inner and outer cylinder's walls, that is,

$$u_\theta(0)=l_s\left(\frac{du_\theta}{dr}-\frac{u_\theta}{r+\alpha}\right)\Bigg|_{r=0}=l_s\,(r+\alpha)\,\frac{d}{dr}\left(\frac{u_\theta}{r+\alpha}\right)\Bigg|_{r=0}, \tag{2.12}$$

$$u_\theta(1)=-l_s\left(\frac{du_\theta}{dr}-\frac{u_\theta}{r+\alpha}\right)\Bigg|_{r=1}=-l_s\,(r+\alpha)\,\frac{d}{dr}\left(\frac{u_\theta}{r+\alpha}\right)\Bigg|_{r=1}, \tag{2.13}$$

where $l_s=L_s/R$ is the dimensionless slip length. The general solution of Equation (2.6) can be expressed as

$$u_\theta(r)=C_1J_1(-i\beta\,[r+\alpha])+C_2Y_1(-i\beta\,[r+\alpha])+\frac{C}{\beta^2}\frac{1}{r+\alpha}, \tag{2.14}$$

where $J_1$ and $Y_1$ are the Bessel's functions of order one of the first and second kind, respectively. As usual, only the real part has to be taken into account for physical interpretations. Constants $C_1$ and $C_2$ are obtained from the slip boundary conditions (2.12) and (2.13) in the form $C_1=CA_1$ and $C_2=CA_2$, where

$$A_1=\frac{1}{\gamma\beta^2}\left(\frac{A(BY_1^{1+\alpha}-i\beta l_s(1+\alpha)Y_0^{1+\alpha})}{\alpha}-\frac{B(AY_1^{\alpha}+i\beta l_s\alpha Y_0^{\alpha})}{1+\alpha}\right), \tag{2.15}$$

$$A_2=\frac{1}{\gamma\beta^2}\left(\frac{A(BJ_1^{1+\alpha}-i\beta l_s(1+\alpha)J_0^{1+\alpha})}{\alpha}-\frac{B(AJ_1^{\alpha}+i\beta l_s\alpha J_0^{\alpha})}{1+\alpha}\right), \tag{2.16}$$

and

$$\begin{aligned}\gamma=&\left(BJ_1^{1+\alpha}-i\beta l_s(1+\alpha)J_0^{1+\alpha}\right)\left(AY_1^{\alpha}+i\beta l_s\alpha Y_0^{\alpha}\right)\\&-\left(AJ_1^{\alpha}+i\beta l_s\alpha Y_0^{\alpha}\right)\left(BY_1^{1+\alpha}-i\beta l_s(1+\alpha)Y_0^{1+\alpha}\right),\end{aligned} \tag{2.17}$$

$$A=\alpha+2l_s,\quad B=1+\alpha-2l_s. \tag{2.18}$$

Here, the superscripts $\alpha$ and $1+\alpha$ mean that the corresponding Bessel functions are evaluated at $-i\beta\alpha$ and $-i\beta\,(1+\alpha)$, respectively. In addition, the constant $C$

is obtained by integrating Eq. (2.10) and applying the boundary conditions for the electric potential:

$$\phi(0) = 0 \quad , \quad \phi(1) = 1, \tag{2.19}$$

therefore,

$$\phi(r) = C \ln|r+\alpha| + \frac{Ha^2}{i\beta} C_1 J_0(-i\beta\,[r+\alpha]) + \frac{Ha^2}{i\beta} C_2 Y_0(-i\beta\,[r+\alpha]) + D, \tag{2.20}$$

where

$$C = \frac{1}{\left(1+\dfrac{Ha^2}{\beta^2}\right)\ln|\kappa| + \dfrac{Ha^2}{i\beta}\left[A_1\left(J_0^{1+\alpha} - J_0^{\alpha}\right) + A_2\left(Y_0^{1+\alpha} - Y_0^{\alpha}\right)\right]}, \tag{2.21}$$

$$D = -\frac{\left(1+\dfrac{Ha^2}{\beta^2}\right)\ln|\alpha| + \dfrac{Ha^2}{i\beta}\left[A_1 J_0^{\alpha} + A_2 Y_0^{\alpha}\right]}{\left(1+\dfrac{Ha^2}{\beta^2}\right)\ln|\kappa| + \dfrac{Ha^2}{i\beta}\left[A_1\left(J_0^{1+\alpha} - J_0^{\alpha}\right) + A_2\left(Y_0^{1+\alpha} - Y_0^{\alpha}\right)\right]}, \tag{2.22}$$

the constant $\kappa$ being defined as $\kappa = R_2/R_1 = 1 + 1/\alpha$. Figure 2.1 shows the azimuthal velocity profile as a function of the radial coordinate for the case of non-slip boundary conditions ($l_s = 0$). In all analyzed cases, a very thin fluid layer is assumed ($\varepsilon = 0.1$), which implies that the Hartmann friction is strong and the velocity magnitude is much smaller than in the case of cylinders of infinite length ($\varepsilon \to \infty$). Velocity profiles in Fig. 2.1a) that correspond to $Ha = 10$, display a marked asymmetry as the $\alpha$ parameter, which characterizes the gap between the concentric cylinders, is varied from 0.01 to 1 (the gap is reduced as $\alpha$ increases). The velocity does not present a monotonous behavior with $\alpha$. First, it increases as $\alpha$ grows, reaching a maximum for $\alpha = 0.1$, and then decreases for higher values. Figure 2.1b) shows the velocity profile as the Hartmann number is increased, for the case $\alpha = 0.5$, that is when the radius of the outer cylinder is three times that of the inner cylinder. For $Ha = 2$ a parabolic-like profile is obtained and, as $Ha$ increases, the profile is flattened and the velocity decreases as a consequence of the magnetic braking effects. Note that in both Figs. 2.1a) and 2.1b) the maximum value of the azimuthal velocity lies closer to the inner cylinder. The effect of slip boundary conditions on the velocity profile is clearly shown in Fig. 2.2a), where $u_\theta$ is plotted as function of the radial coordinate for $Ha = 10$, $\varepsilon = 0.1$, $\alpha = 0.5$ and different values of the dimensionless slip length parameter, $l_s$. Higher velocities are found close to the inner cylinder and a drastic increase on the slip velocity at the walls is observed as $l_s$ varies from 0 to 100, where the latter value could be considered as

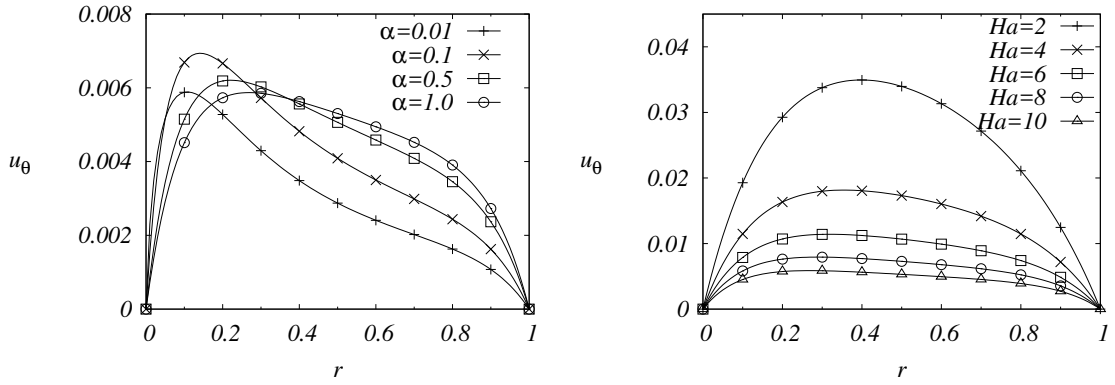


Figure 2.1: *a*) Velocity profile as function of the radial coordinate for different values of the $\alpha$ parameter. $Ha = 10$, $l_s = 0$, $\varepsilon = 0.1$. *b*) Velocity profile as function of the radial coordinate for different values of the Hartmann number. $\alpha = 0.5$, $l_s = 0$, $\varepsilon = 0.1$.

perfect slip ($l_s \to \infty$). Note, however, that the core flow remains mostly unchanged, independently of the $l_s$ parameter. The effect of the slip at the boundaries can also be assessed by calculating the volumetric flow rate, $Q$, in the gap between the cylinders. By direct integration of the velocity profile, we get

$$Q = -\frac{iC_1}{\beta}\Big[J_0(-i\beta[1+\alpha]) - J_0(-i\beta\alpha)\Big] - \frac{iC_2}{\beta}\Big[Y_0(-i\beta[1+\alpha]) - Y_0(-i\beta\alpha)\Big] + \frac{C}{\beta^2}\ln|\kappa|. \quad (2.23)$$

Figure 2.2b) shows the flow rate as function of the Hartmann number for different values of the slip parameter. For $Ha < 1$, a substantial increase of $Q$ is observed as $l_s$ varies from 0 to 100, while for higher Hartmann number the reduction of $Q$ is approximately the same for all $l_s$ values. Figures 2.3a) and 2.3b) show the electric potential for the liquid metal flow (Eq. 2.20) as function of the radial coordinate for different values of $Ha$ and $\alpha$, respectively. From Fig. 2.3a) it is clear that the variation of the Hartmann number does not affect the electric potential distribution, while Fig. 2.3b) shows that this quantity is modified by the separation between the concentric cylinders (electrodes). This behavior has a consequence on the electric current distribution and, hence, in the Lorentz force.

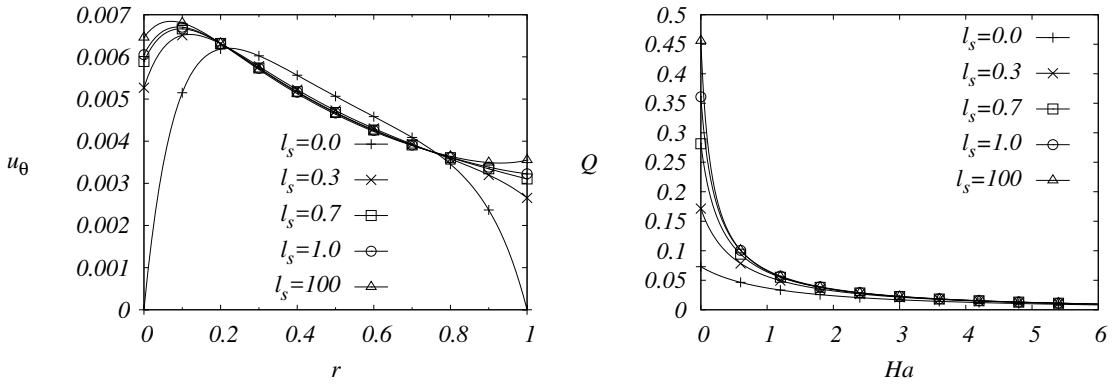


**(a)** **(b)**

Figure 2.2: *a*) Velocity profile for liquid metal flow as function of the radial coordinate for different values of the dimensionless slip length parameter, $l_s$. $Ha = 10$, $\alpha = 0.5$, $\varepsilon = 0.1$. *b*) Liquid metal flow rate for different values of the dimensionless slip length parameter as function of $Ha$. $\varepsilon = 0.1$, $\alpha = 0.5$.

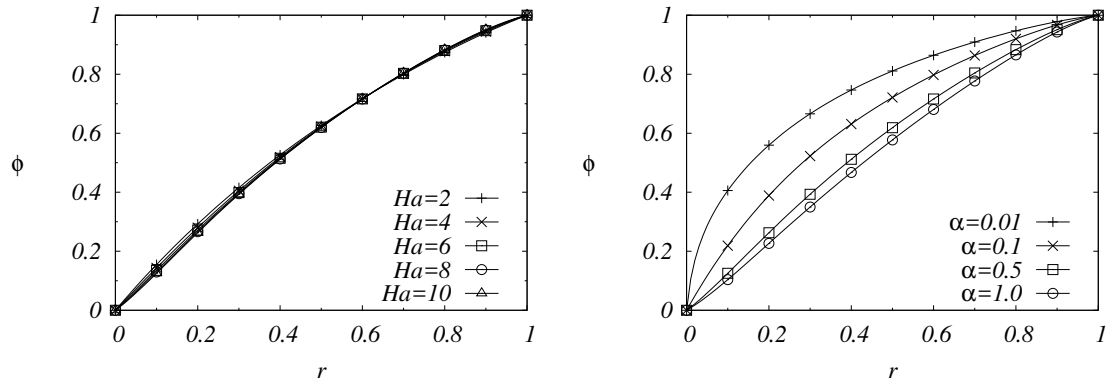


**(a)** **(b)**

Figure 2.3: *a*) Electric potential for the liquid metal flow as function of the radial coordinate for different values of the Hartmann number. $\alpha = 0.5$, $l_s = 0$, $\varepsilon = 0.1$. *b*) Electric potential for the liquid metal flow as function of the radial coordinate for different values of the geometrical parameter $\alpha$. $Ha = 10$, $\varepsilon = 0.1$, $l_s = 0$.

## 2.5 Solution for the electrolytic flow

It can be shown that for fluids of low electrical conductivity such as electrolytes, induction effects are negligible and fluid velocity is uncoupled from the electromagnetic equations [Figueroa *et al.* (2009)]. Also, in electrolytes under moderate magnetic fields the Hartmann number is very small ($Ha \ll 1$). In this case, the Poisson equation for the electric potential (Eq. 2.4) reduces to a Laplace equation and the solution for $\phi$ is expressed as

$$\phi(r) = \ln\left(\frac{r+\alpha}{\alpha}\right) / \ln|\kappa|. \tag{2.24}$$

In fact, this solution can be obtained from Equation (2.20) in the limit $Ha \to 0$.This implies that the applied radial current is proportional to $1/(r+\alpha)$. Under these conditions, Equation (2.6) reduces to

$$\frac{d^2u_\theta}{dr^2} + \frac{1}{r+\alpha}\frac{du_\theta}{dr} - \left(\frac{1}{(r+\alpha)^2} + \frac{1}{\varepsilon Re}\right)u_\theta = -\frac{1}{\ln|\kappa|}\frac{1}{r+\alpha}, \tag{2.25}$$

which is again a non-homogeneous Bessel equation. In this case, the linear friction term that appears in the Q2D approach due to the existence of a viscous boundary layer in the bottom wall takes the form $-u_\theta/(\varepsilon Re)$ [Satijn *et al.* (2001)], where the Reynolds number is given by $Re = u_0 R/\eta$. The solution of Eq. (2.25) under slip boundary conditions (2.12) and (2.13) can be expressed as

$$u_\theta(r) = C_3 J_1(-i\beta\,[r+\alpha]) + C_4 Y_1(-i\beta\,[r+\alpha]) + \frac{1}{\beta^2\ln|\kappa|}\frac{1}{r+\alpha}, \tag{2.26}$$

where $\beta^2 = 1/(\varepsilon Re)$. The constants $C_3$ and $C_4$ take the form

$$C_3 = \frac{1}{\gamma\beta^2\ln|\kappa|}\left(\frac{A(BY_1^{1+\alpha} - i\beta l_s(1+\alpha)Y_0^{1+\alpha})}{\alpha} - \frac{B(AY_1^{\alpha} + i\beta l_s\alpha Y_0^{\alpha})}{1+\alpha}\right), \tag{2.27}$$

$$C_4 = \frac{1}{\gamma\beta^2\ln|\kappa|}\left(\frac{A(BJ_1^{1+\alpha} - i\beta l_s(1+\alpha)J_0^{1+\alpha})}{\alpha} - \frac{B(AJ_1^{\alpha} + i\beta l_s\alpha J_0^{\alpha})}{1+\alpha}\right), \tag{2.28}$$

where $\gamma$, $A$ and $B$ are given by Equations (2.18) and (2.17). Figure 2.4 shows the velocity profiles for the electrolytic flow as function of the radial coordinate for $Re = 0.1$ and $\varepsilon = 0.1$. In Fig. 2.4a) profiles are displayed for different values of the $\alpha$ parameter, assuming the non-slip condition ($l_s = 0$). There is a resemblance

with profiles obtained for the liquid metal flow (see Fig. 2.1a), but in this case the magnitude of the velocity is almost 50% higher than for the liquid metal. This can be explained since for liquid metals the Hartmann friction is stronger than the viscous friction. Also, as in the liquid metal flow, the geometrical confinement has a pronounced effect on the asymmetry of the profile: the smaller the value of $\alpha$ (thick gap conditions) the stronger the asymmetry. Figure 2.4b) shows the profiles for different values of the dimensionless slip length and $\alpha = 0.5$. Again, the profiles are similar to the ones obtained in the liquid metal case but the velocities are almost 50% higher.

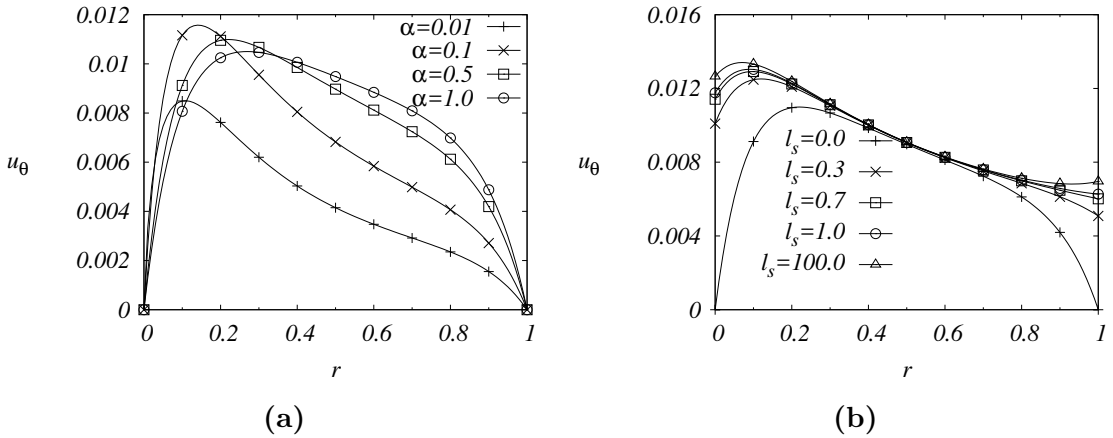


Figure 2.4: *a*) Velocity profiles for the electrolytic flow as function of the radial coordinate for different values of the $\alpha$ parameter. $Re = 0.1$, $\varepsilon = 0.1$ and $l_s = 0$. *b*) Velocity profiles for the electrolytic flow as function of the radial coordinate for different values of the dimensionless slip length parameter. $Re = 0.1$, $\varepsilon = 0.1$ and $\alpha = 0.5$.

Figure 2.5a) shows the velocity profile as function of the radial coordinate for Reynolds numbers varying from 0.01 to 1, assuming non-slip conditions ($l_s = 0$) and $\alpha = 0.5$. The velocity increases as $Re$ grows while the profile presents a more parabolic shape, although maximum velocity values are still closer to the inner cylinder. In Fig. 2.5b) the volumetric flow rate is displayed as function of the Reynolds number for values of the dimensionless slip parameter ranging from 0 to 100, where this last value represents perfect slip. By integrating the velocity profile in the gap between the cylinders, the explicit form of the flow rate reads

$$Q = -\frac{iC_3}{\beta}\Big[J_0(-i\beta[1+\alpha]) - J_0(-i\beta\alpha)\Big] - \frac{iC_4}{\beta}\Big[Y_0(-i\beta[1+\alpha]) - Y_0(-i\beta\alpha)\Big] + \frac{C}{\beta^2}. \qquad (2.29)$$

In spite of the viscous friction at the bottom, the flow rate grows with $Re$ while, as expected, a substantial gain is also observed as the parameter $l_s$ increases. It is observed that for $l_s \to \infty$, the flow rate grows linearly with $Re$, reaching a saturation value, as also occurs in other situations [Rivero & Cuevas (2012)].

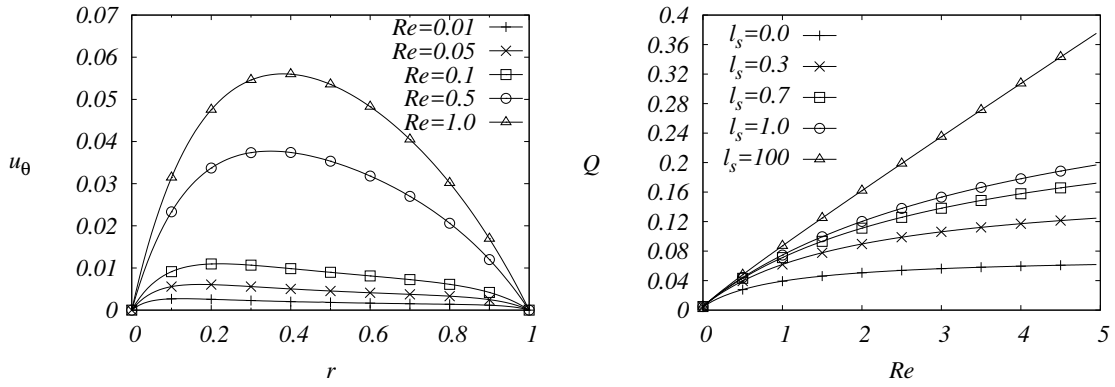


**(a)** **(b)**

Figure 2.5: *a*) Velocity profiles for the electrolytic flow as function of the radial coordinate for different Reynolds numbers. $\alpha = 0.5$, $\varepsilon = 0.1$ and $l_s = 0$. *b*) Electrolytic flow rate as function of $Re$ for different values of the dimensionless slip length parameter. $\varepsilon = 0.1$, $\alpha = 0.5$

## 2.6 Conclusions

In this Chapter, analytical solutions were provided for the azimuthal flow of a conducting fluid in an annular MHD stirrer that has been proposed for microfluidic applications [West *et al.* (2003), Gleeson *et al.* (2004), Gleeson (2005)]. The flow is driven by an azimuthal Lorentz force created by the interaction of an imposed radial current and an applied axial magnetic field. The cases of a highly conducting fluid (a liquid metal) and a poorly conducting fluid (an electrolyte) were considered. Unlike analytical solutions available in the literature, where the conducting concentric cylinders are assumed to be infinitely long, MHD flows have been explored here using a Q2D model that introduces a linear friction term that accounts for the existence

of boundary layers (either Hartmann or viscous layers) attached to the bottom wall. The bottom friction has a drastic effect in the flow behavior, reducing considerably the magnitudes of the velocity and flow rate. In addition, slip boundary conditions were considered at the lateral walls (conducting cylinders) and it was verified that the maximum velocity and flow rate increase as the slip length parameter grows. Further, it was found that the gap between the cylinders has a strong influence in the shape of the velocity profile: the larger the gap, the more asymmetric the profile.

The solutions presented here can be used as the starting point for microfluidic mixing studies, either with liquid metals or electrolytes, similarly to those performed with a more idealized solution [Gleeson *et al.* (2004), Gleeson (2005)].

Chapter 3

# Numerical solutions of the governing equations[♮]

This Chapter describes the three-dimensional numerical solutions of the governing equations for the electrolytic flow inside the electromagnetic stirrer previously described. It starts with a discussion of axisymmetric solutions based on quasi-two-dimensional and thin layer approximations. It continues with a selection of reasonable scales for the problem under consideration and the establishment of the dimensionless equations to be solved. Further, the experimental magnetic field is accurately modeled by means of analytical expressions reported in the literature. The numerical results obtained are presented in the form of velocity field distributions and velocity profiles, which are used to describe the full 3D behavior of the flow. Moreover, the numerical results are compared with experimental measurements, finding a good quantitative and qualitative agreement. A numerical implementation of the Lagrangian tracking of passive tracer particles was implemented in order to compare with the experimental observations described in Chapter 1. It is shown that the flow evolution is properly reproduced by the numerical simulation. This includes the initial axisymmetric flow as well as the triggering of the instability and the appearance of the anticyclonic vortices.

[♮]Part of this chapter was published in Suslov *et al.* (2017), *Electromagnetically driven flow of electrolyte in a thin annular layer: axisymmetric solutions.* **Journal of Fluid Mechanics**, Vol. 828, pp. 573-600.

## 3.1 Axisymmetric solutions in quasi-two dimensional and thin-layer approximations

Before presenting the full three-dimensional numerical simulation using a realistic magnetic field distribution we discuss some attempts to model the flow in the electromagnetic annular stirrer using simplified models. In fact, assuming that the fluid is contained between two coaxial perfectly conducting cylinders of infinite length under a uniform axial magnetic field the problem becomes 2D and an analytic solution is available [see for instance, Digilov (2007), Zhao *et al.* (2011)]. Even though exact 2D solutions are a valuable resource to validate numerical codes and get some insight of the flow, all our attempts to numerically reproduce the experimentally observed instability using a 2D approach failed. Therefore, in the following we discuss axisymmetric solutions obtained using quasi-two-dimensional and thin layer approximations trying to improve the modeling of the flow. These solutions as well as 3D axisymmetric numerical solutions are presented in detail in Suslov *et al.* (2017) and were obtained as a first step of an stability analysis currently being developed in parallel to the present work. Here, only the main results are highlighted as a background for the discussion of the numerical three-dimensional results. The quasi-two-dimensional solutions were obtained using a disk magnet vertically polarized and assuming a homogeneous magnetization. Experiments conducted with rectangular magnets revealed that the observed flow patterns remain largely the same as those arising when a smaller disk magnet is used as long as the horizontal dimensions of the rectangular magnet are larger than the diameter of the disk magnet, and the diameter of the magnet is not smaller than the outer diameter of the experimental container, so that no magnetic field reversal occurs within the electrolyte layer.

The symmetry of the problem suggests that an approximate steady two-dimensional solution $\mathbf{u} = (0, u_\theta(r,z), 0)$, $\mathbf{j} = (j_r(r,z), 0, j_z(r,z))$, $\phi = \phi(r,z)$ may exist. However, since the component $u_\theta(r,z)$ is enforced by the no-slip boundary condition at the bottom of the layer, the pressure equations cannot be satisfied, indicating that the problem solution is inherently three-dimensional with all velocity components being non-zero. Strictly, the quasi-two-dimensional solution with $p \approx$ const. can only exist in thin layers with a vanishing aspect ratio, $\varepsilon \to 0$. It was found that assuming a uniform magnetic field in the vertical direction ($B_z = 1$ in dimensionless terms), it is possible to get an exact solution away from the cylindrical electrodes although it does not satisfy the no-slip boundary conditions at the surface of the electrodes where boundary layers are formed. The analytical solution was compared with a high accuracy numerical spectral solution of the quasi-two-dimensional equation and

results are shown in Fig. 3.1.

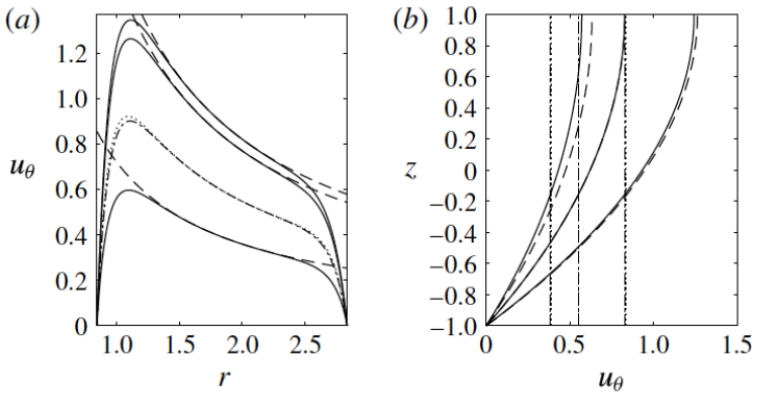


Figure 3.1: Quasi-two-dimensional azimuthal (dimensionless) velocity profiles corresponding to a reference magnetic field intensity of $B_0 = 0.02$ T, an applied current of $I_0 = 0.05$ A with a layer thickness of $h = 2.5$ mm. The inner and outer cylinders are located at $r = 1$ and $r = 2.8$ while the bottom wall is at $z = -1$ and the free surface at $z = 1$. The profiles are shown for $z = 1.0$, 0.5 and -0.5 in panel (a) (top to bottom), and for $r = 1.30$, 1.98 and 2.60 (right to left) in panel (b). The solid and dashed lines represent the numerical and exact solutions, respectively. The dash-dotted and dotted lines show the depth-averaged profiles with two different procedures. [Suslov *et al.* (2017)].

As seen from this figure, away from the cylindrical walls, the analytical and numerical (dimensionless) solutions coincide within the plotting resolution, but deviate from one another significantly in the boundary layers. It is important to note that in thin electrolyte layers, the maximum of the azimuthal velocity is necessarily located near the inner cylinder. As a result, the largest flow shear is found at small values of $r$. This is where the shear instability would be expected to set first, which, however, is not seen in our experiments. The variation of the geometry and strength of the magnetic field created by a realistic magnet is expected to only enhance this effect, as it weakens the driving Lorentz force near the outer edge of the layer.

Figure 3.1 also shows the approximate radial profile of the azimuthal velocity component in the complete flow domain calculated using a depth-averaged model as the one used in the previous Chapter [see also Pérez-Barrera *et al.* (2016)], assuming also a uniform magnetic field. This approach is commonly used in studies of thin fluid

layers [see Sommeria (1988), Andreev *et al.* (2001) for discussion in an MHD context]. Such a model is obtained by integrating the governing equations over the layer thickness and taking into account the proper boundary conditions. Two different procedures were implemented and the solutions are virtually indistinguishable except for a small difference in the boundary layers. On the other hand, it was found that in the vicinity of cylindrical walls, the quasi-two-dimensional approximation underestimates the bottom friction and thus predicts a slightly faster depth-averaged velocity than the full set of equations.

When a realistic magnetic field is considered, no analytical solutions are readily available. Thus, the quasi-two-dimensional equations were solved numerically using the Chebyshev pseudo-spectral collocation method. In Fig. 3.2, the azimuthal velocity profiles obtained for realistic magnetic fields created by a disk magnet are shown. Due to axial symmetry, the azimuthal component of the magnetic field is zero, therefore, the applied magnetic field is of the form $\mathbf{B} = (B_r(r,z), 0, B_z(r,z))$. To calculate the field the magnetostatic equations were solved with the same reference magnitude $B_0$ as that of the uniform vertical magnetic field used in Fig. 3.1. Comparison of the two figures demonstrates a remarkable robustness of the velocity profiles. Even though the details of the magnetic fields used to obtain the two solutions are drastically different, the velocity profiles remain qualitatively unchanged. However, quantitatively, the velocity profiles become fuller in the middle part of the flow region away from the electrodes: the profiles lie somewhat higher (to the right) in Fig. 3.2a) (Fig. 3.2b) than the dashed lines representing the reference analytical solutions.

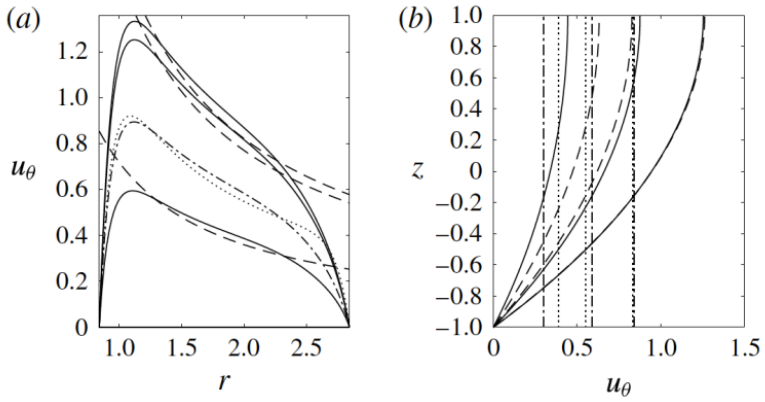


Figure 3.2: The same as Fig. 3.1 but for a realistic magnetic field created by a disk magnet placed 6 mm below the bottom of the electrolyte layer [Suslov *et al.* (2017)].

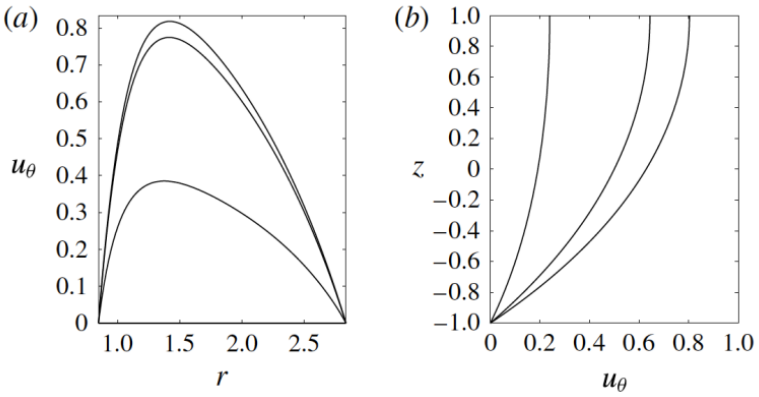


Figure 3.3: Quasi-two-dimensional azimuthal profiles calculated numerically for an electrolyte layer placed in a magnetic field created by a disk magnet at $\varepsilon = 0.248$. The reference magnetic field intensity is $B_0 = 0.02$ T and the applied current $I_0 = 0.2$ A and the layer thickness $h = 7.5$ mm. The profiles are shown for $z = 1.0$, 0.5 and -0.5 in panel (a) (top to bottom), and for $r = 1.30$, 1.98 and 2.60 (right to left) in panel (b) [Suslov *et al.* (2017)].

This trend continues as the depth of the layer and the electric current increase, and the shape of the velocity profile eventually deviates from that given by the depth-averaged model, as is shown in Fig. 3.3. The curvature of the velocity profiles becomes uniformly negative, but the largest velocity gradient is still found near the inner cylinder. This suggests that a potential shear instability would still set in preferentially near the inner cylinder. However, this is not what is observed experimentally. The failure to reproduce some of the main features observed in the experiment leads to the necessity of implementing a full three-dimensional numerical approach.

## 3.2 Dimensionless equations

To express the governing equations in a convenient nondimensional form where dimensionless parameters appear, characteristc scales are first defined. The length scale is taken as the gap between the electrodes ($L = R_2 - R_1$), the characteristic magnetic field is taken as the strength of the magnet, $B_0$, at certain position, namely, at the bottom of the cavity at the interface between the inner electrode and the fluid, as shown in Fig. 1.1; and the characteristic electric current is the applied

electric current $I_0$ used in the experiments, therefore, the current density is given by $J_0 = I_0/A$, where $A$ is the area through which the electric current is passing by, depending on the type of inner electrode used in the analysis. The characteristic velocity, which is related to the pressure drop caused by the Lorentz force, is taken as

$$u_c = \sqrt{\frac{j_0 B_0 L}{\rho}}. \tag{3.1}$$

The dimensionless variables are defined as

$$\mathbf{r}^* = \frac{\mathbf{r}}{L}, \quad \mathbf{B}^* = \frac{\mathbf{B}}{B_0}, \quad \mathbf{u}^* = \frac{\mathbf{u}}{u_c}, \quad \mathbf{j}^* = \frac{\mathbf{j}}{j_0}, \tag{3.2}$$

$$p^* = \frac{p}{\rho u_c^2}, \quad t^* = \frac{t}{L/u_c}, \quad \phi^* = \frac{\phi - \phi_1}{\phi_2 - \phi_1}, \tag{3.3}$$

where $\phi_1$ and $\phi_2$ are the values of the electric potential at the inner and outer electrodes, respectively, and the superscript (*) is used to refer to a dimensionless variable.

Substituting the dimensionless variables in the governing equations (see Appendix A) and dropping the superscript, the dimensionless governing equations can be expressed as

$$\nabla \cdot \mathbf{u} = 0, \tag{3.4}$$

$$\frac{\partial \mathbf{u}}{\partial t} + (\mathbf{u} \cdot \nabla)\mathbf{u} = -\nabla p + \frac{1}{Re}\nabla^2 \mathbf{u} + \mathbf{j} \times \mathbf{B}, \tag{3.5}$$

$$\mathbf{j} = -\nabla \phi + \frac{Ha^2}{Re}\mathbf{u} \times \mathbf{B}_0, \tag{3.6}$$

$$\nabla^2 \phi = \frac{Ha^2}{Re}\nabla \cdot (\mathbf{u} \times \mathbf{B}_0)\,. \tag{3.7}$$

The set of equations (3.4)-(3.7) constitutes a well-posed system which can be solved if suitable initial and boundary conditions are supplied.

## 3.3 Boundary conditions

In order to complete the set of governing equations and making it mathematically solvable, the following boundary conditions for the velocity field and electric potential

were implemented:

$$\mathbf{u} = 0, \quad \text{at solid boundaries,} \tag{3.8}$$

$$\frac{\partial u}{\partial z} = \frac{\partial v}{\partial z} = 0, \quad w = 0 \quad \text{at the free surface,} \tag{3.9}$$

$$\phi = 1, \quad \text{at the inner electrode;} \quad \phi = 0, \quad \text{at the outer electrode.} \tag{3.10}$$

$$\frac{\partial \phi}{\partial z} = 0, \quad \text{at the bottom and top boundaries.} \tag{3.11}$$

Equation (3.8) is the standard no-slip boundary condition. For this case solid boundaries refer to the electrodes and the bottom of the container. Equation (3.9) implies the absence of shear stress at the free surface and also that, for all intents and purposes, the free surface remains flat. In fact, as soon as the fluid starts rotating the free surface curves, but this deformation is very small and cannot be appreciated with the naked eye. An estimation of the deformation of the free surface for this particular flow can be found in Suslov *et al.* (2017), where it is shown that it can be neglected. Equation (3.10) sets the potential difference between the electrodes that establishes the current flow, whereas Eq. (3.11) implies that the bottom of the cavity (which is made of acrylic) and the free surface (which is in contact with air) are electrically insulated.

## 3.4 Applied magnetic field

In order to perform realistic numerical simulations it is necessary to feed the numerical code with accurate information regarding the experimental conditions. In fact, the accurate representation of the applied magnetic field distribution is crucial for the realistic simulation of magnetohydrodynamic flows. The magnetic field of the permanent magnet used in the experiments was measured by means of an automatic device which consists of two highly-precise, perpendicular positioners controlled by a computer, a magnetic probe attached to one of the positioners and a Gaussmeter, as shown in Fig. 3.4. Measurements of the normal component of the magnetic field were made in a plane located 3 mm away from the surface of the magnet, sweeping an area of 10.1 cm $\times$ 15.1 cm (which is large enough to cover the whole flow region of the electromagnetic stirrer) with a spatial resolution of 1 mm. In this way, a map of the spatial distribution of the normal field component was obtained. Given the size of the magnet and the spatial resolution of the measurements, about 15,000 measured data were obtained.

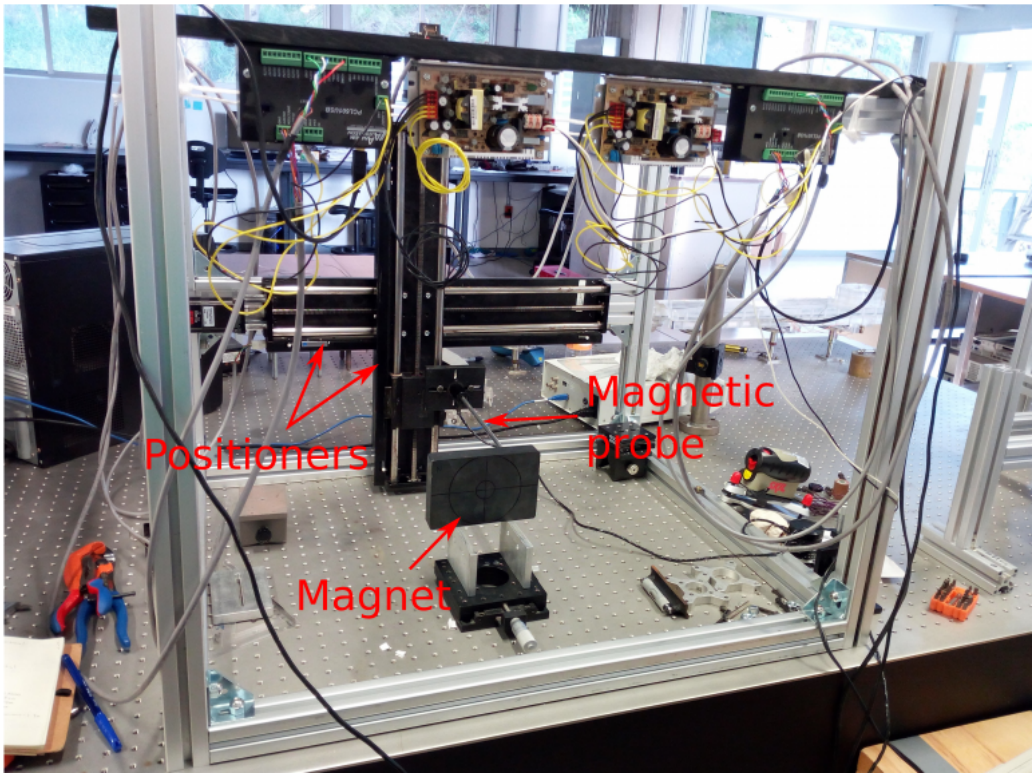


Figure 3.4: Mesaurement device to characterize permanent magnets. The magnetic probe is colocated in such a way that the normal component to the surface of the magnet can be measured.

Figure 3.5 shows the mapping of the normal component of the magnetic field in a plane 3 mm away from the magnet. It can be seen that due to the size of the magnet, the maximum values of the normal component are located close to the corners of the magnet, although decays very rapidly at the edges.

Once the magnet is characterized, the magnetic field distribution must be introduced in the numerical code. This can be done by interpolating the measured values to the numerical grid or using analytical expresions that reproduce this distribution. Due to the fact that measurements were made only for a single plane from which we cannot interpolate to other planes, it was chosen to use an analytical expression in the numerical code. There are some accurate expressions for different magnet geometries [*v. e.* McCaig (1977), Furlani (2001)] which can be fitted to the experimental measurements.

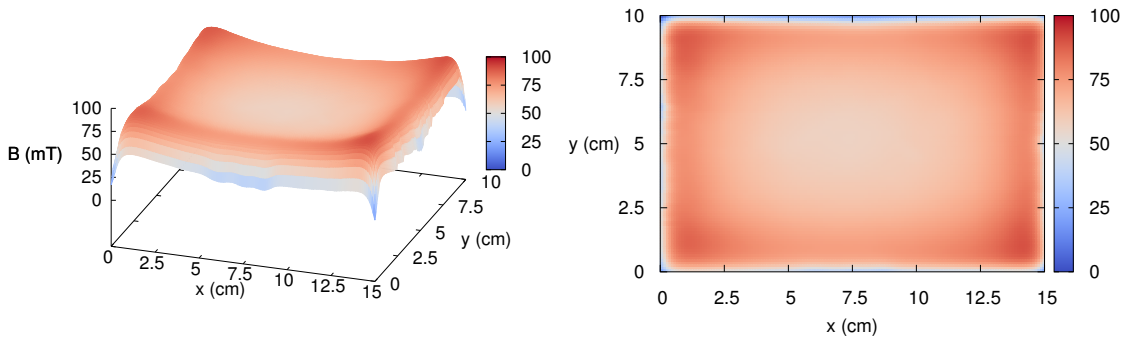


(a) (b)

Figure 3.5: Experimental characterization 3 mm above the permanent magnet used in the electromagnetic stirrer . (*a*) Isometric view. (*b*) Top view. Colors indicate the magnetic field strength of the normal component.

Consider a rectangular permanent magnet of dimensions $a$, $b$ and $c$ along the $x$, $y$ and $z$ coordinates, respectively, magnetized along the $z$-axis, as shown in Fig. 3.6. This magnet will generate a static, 3D magnetic field in the surrounding space which can be calculated according to Furlani's analytical expressions for a finite-sized, bar magnet [Furlani (2001)], namely:

$$B_x(x,y,z) = \frac{\mu_0 M_s}{4\pi} \sum_{k=1}^{2} \sum_{m=1}^{2} (-1)^{k+m} \ln\left[F(x,y,z,x_m,y_1,y_2,z_k)\right], \tag{3.12}$$

where

$$F(x,y,z,x_m,y_1,y_2,z_k) = \frac{(y-y_1) + \left[(x-x_m)^2 + (y-y_1)^2 + (z-z_k)^2\right]^{1/2}}{(y-y_2) + \left[(x-x_m)^2 + (y-y_2)^2 + (z-z_k)^2\right]^{1/2}}, \tag{3.13}$$

$$B_y(x,y,z) = \frac{\mu_0 M_s}{4\pi} \sum_{k=1}^{2} \sum_{m=1}^{2} (-1)^{k+m} \ln\left[H(x,y,z,x_1,x_2,y_m,z_k)\right], \tag{3.14}$$

where

$$H(x,y,z,x_1,x_2,y_m,z_k) = \frac{(x-x_1) + \left[(x-x_1)^2 + (y-y_m)^2 + (z-z_k)^2\right]^{1/2}}{(x-x_2) + \left[(x-x_2)^2 + (y-y_m)^2 + (z-z_k)^2\right]^{1/2}}, \tag{3.15}$$

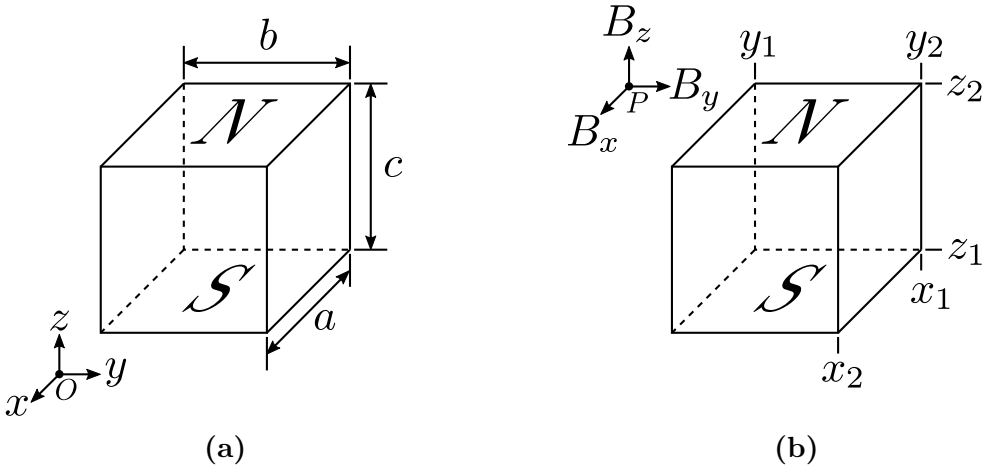


Figure 3.6: Skecth of a permanent bar magnet of dimensions $a$, $b$, $c$. ($a$) Magnetization and reference frame. ($b$) At some observation point $P$ the magnet creates a 3D field with components $B_x$, $B_y$, $B_z$ along the respective axes.

$$B_z(x,y,z) = \frac{\mu_0 M_s}{4\pi} \sum_{k=1}^{2}\sum_{n=1}^{2}\sum_{m=1}^{2} (-1)^{k+n+m} \tan^{-1}\left[\frac{(x-x_n)(y-y_m)}{(z-z_k)} g(x,y,z,x_n,y_m,z_k)\right], \tag{3.16}$$

where

$$g(x,y,z,x_n,y_m,z_k) = \frac{1}{\left[(x-x_n)^2+(y-y_m)^2+(z-z_k)^2\right]^{1/2}}. \tag{3.17}$$

In Equations (3.12) - (3.17) $x_1$, $x_2$, $y_1$, $y_2$, $z_1$, $z_2$ refer to the coordinates where the vertices of the magnet are located (see Fig. 3.6b); $\mu_0 = 4\pi \times 10^{-7}$ Tm/A is the magnetic permeability of vacuum (magnetic constant) and $M_s$ is the magnetization parameter of the magnet, given in A/m.

Qualitative agreement can be found by comparing the experimental isolines of $B_z$ and the isolines obtained with the analytical expressions, as shown in Fig. 3.7. It can be seen that the distribution of the magnetic field is very inhomogeneous close to the edges of the magnet whereas in the central region (where the flow domain is mostly located) the isolines form elipses due to the rectangular shape of the magnet. This fact renders a non-axisymmetric Lorentz force which is dependent on the spatial position. In turn, this spatial dependence of the driving force is likely to be an important factor to trigger the experimentally observed instability.

In order to use Furlani's equations in the numerical code, the magnetization of the

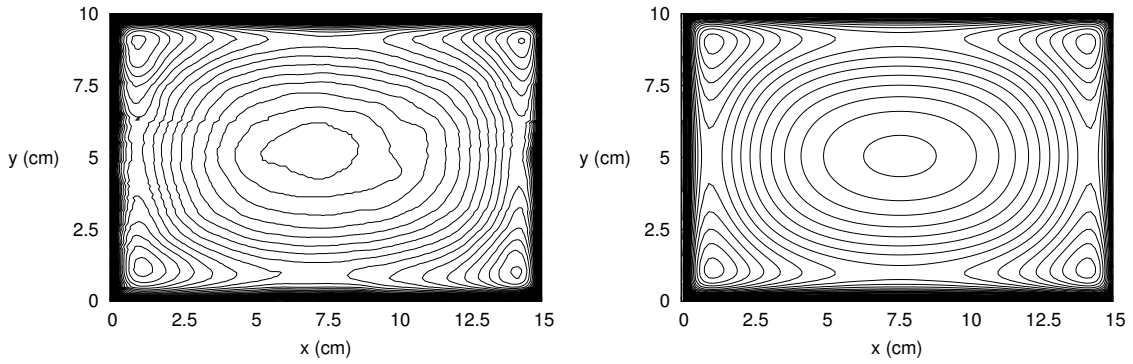


**(a)** **(b)**

Figure 3.7: Isolines of the $z$-component of the magnetic field. ($a$) Experimental measurements. ($b$) Furlani's analytical expression. It can be observed that the magnetic field is symmetric with respect to both the $x$- and $y$-axes.

magnet must be estimated, so the value of $M_s$ was varied to match the measured $z$-component of the magnetic field in the centerline along the $x$-coordinate. This process was made at a distance of 3 mm away from the surface of the magnet, for which the proposed value of the magnetization is $M_s = 2.65 \times 10^5$ A/m. Keeping this value fixed, the experimental measurements at a distance of 6 mm and 10 mm away from the magnet were compared with the corresponding analytical calculations. Figure 3.8 shows the comparison of the experimental measurements and Furlani's analytical expressions. For the three distances compared there is a good agreement between the calculated and experimental values. It can be observed that close to the surface of the magnet, the normal component of the magnetic field has an $M$-shaped symmetrical profile with its maximum values near the edges of the magnet from which it decays very fast, whereas in the center (where the flow domain is mostly located) $B_z$ is more uniform. When moving away from the magnet, the profile tends to flatten in the center and it is expected that for a long enough distance the profile becomes similar to a Gaussian distribution.

Figure 3.9 shows the computed magnetic field components for the domain of interest at two different heights. It can be seen from Figs. 3.9a) - 3.9d) that the azimuthal and radial components of the magnetic field barely change inside the electrolyte layer. On the other hand the axial component drastically changes in both shape and magnitude within the fluid layer.

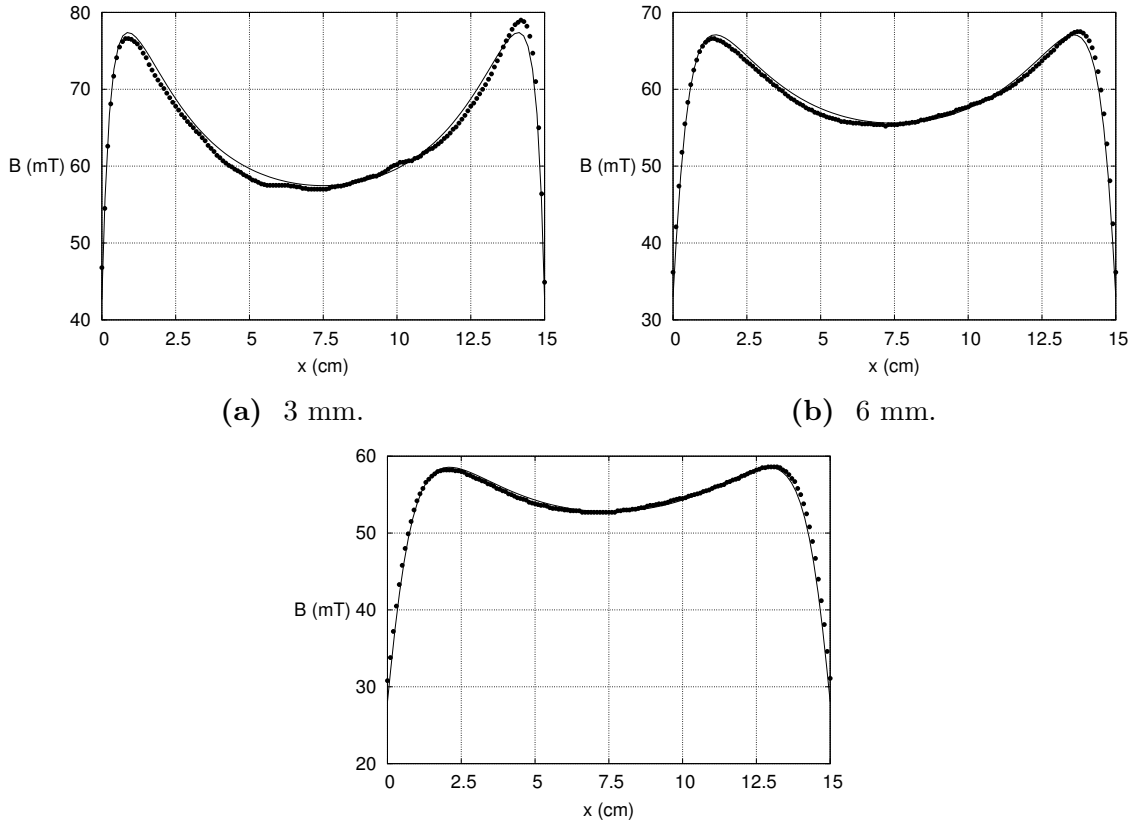


**(a)** 3 mm.

**(b)** 6 mm.

**(c)** 10 mm.

Figure 3.8: Comparison between the experimental measurements (black points) and Furlani's expression (solid line) for the $z$-component of the magnetic field along the centerline of the magnet for different heights.


(a) $B_\theta$

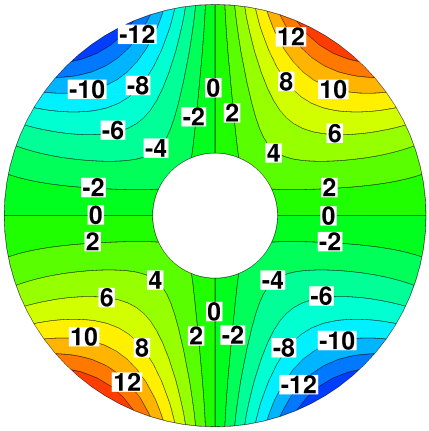


(b) $B_\theta$

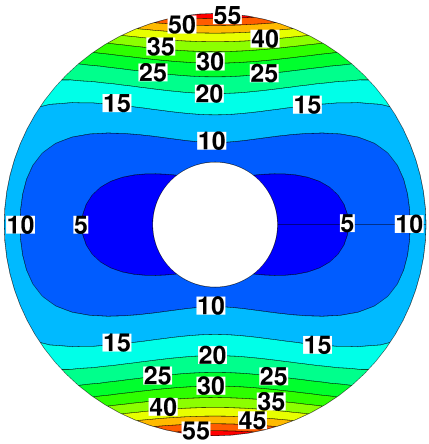


(c) $B_r$

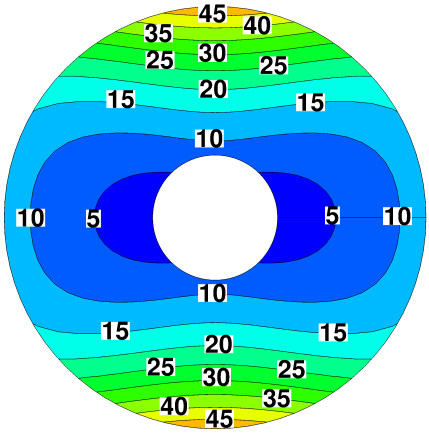


(d) $B_r$

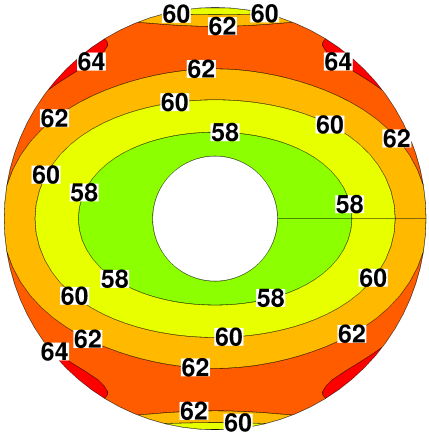


(e) $B_z$

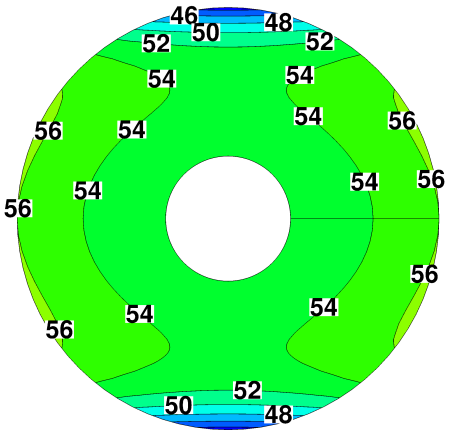


(f) $B_z$

Figure 3.9: Computed components of the magnetic field (in mT) at the bottom of the container (left column) and free surface (right column) of a 5 mm electrolyte layer.

## 3.5 Numerical results

In order to solve the governing equations numerically, a hybrid Fourier-Galerkin - Finite volume technique, as described by Nuñez *et al.* (2012), was implemented. Appendix B gives a brief description of the numerical method. The numerical code was partially paralellized using *OpenMP* directives and the calculation of the Fast Fourier Transform (FFT) as well as the solution of the linear systems of equations were optimized by the implementation of *Fishpack* libraries[a].

### 3.5.1 Mesh selection

A purely azimuthal experimental flow was measured using the PIV technique and compared with the numerical solutions for different mesh sizes. Figure 3.10 shows the comparison between the experimental measurements and the numerical solution of the azimuthal velocity as function of time for two different meshes for an applied electric current of 50 mA and an electrolyte layer thickness of 5 mm. It can be seen that the numerical solution reaches terminal velocity faster than the experiment, but both experimental and numerical velocity values are very close. It can also be noticed that the finer the mesh, the closer the numerical results are to the experiment.

In order to select an optimal mesh for the numerical calculations, several mesh sizes were used in the computations. By optimal it must be understood a mesh size that is fine enough to yield results very close to the experimental observations while also being coarse enough to render the numerical computations feasible, that is to say, the computational time needed to solve the problem is not extremely long. Table 3.1 shows the terminal velocity calculated using different mesh sizes as well as the difference with the measured velocity, which was averaged in the last 30 seconds of a one minute long experiment and has a value of $\sim 2.05$ cm/s. It can be seen that changing the number of nodes in the $\theta$-direction, $n_\theta$, does not affect the value of the terminal velocity, since $n_\theta$ is related to the number of Fourier modes considered in the solution. Since spectral accuracy is obtained with a small number of Fourier modes, it is expected that increasing the value of $n_\theta$ (and thus the number of Fourier modes) does not yield a significant improvement to the numerical solution. Therefore, in order to get closer results to the experimental measurements, the number of control volumes in the other two directions must be increased. Looking carefully at Table 3.1

[a] All these improvements in the numerical code were performed during a stay at the *Technische Universität Ilmenau* (TUI) in Ilmenau, Germany under the advise of Dr. Dmitry Krasnov.

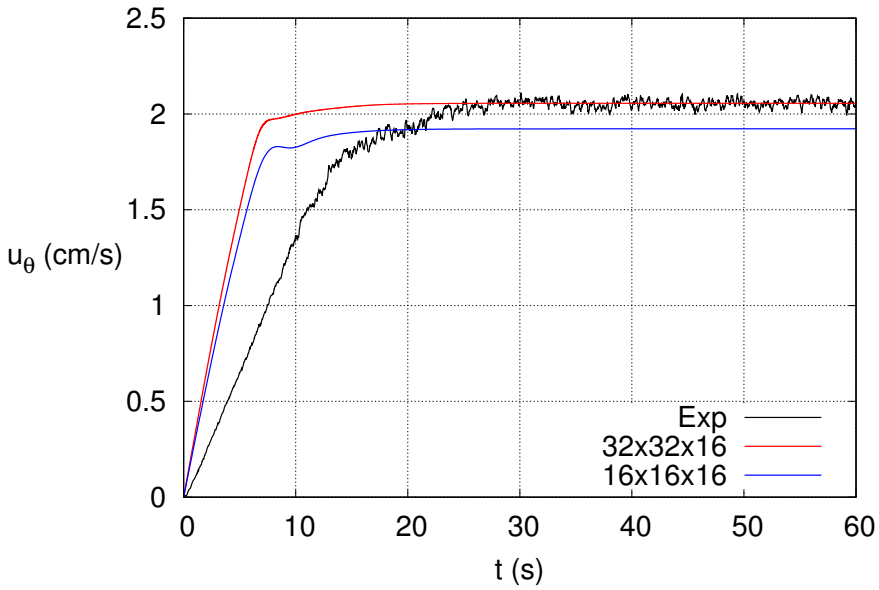


Figure 3.10: Comparison between the measured (black line) and calculated (blue and red lines) azimuthal velocity as function of time at $r = 3.1$ cm for an azimuthal flow. $I = 50$ mA and $h = 5$ mm.

it can also be seen that the value of $n_r$ has a larger impact in the computed solutions than the value of $n_z$ since going from $n_r = 16$ to $n_r = 32$ reduces the difference with the measured velocity from 0.13 cm/s to 0.02 cm/s whereas the increment of $n_z$ does not improve the numerical solutions significantly. From the above considerations, the optimal mesh chosen to produce the subsequent results was $64 \times 64 \times 32$. This choice was due to the fact that flows where vortices appear are more complex than a purely azimuthal flow. Using the aforementioned mesh size and a time step $\Delta t = 2 \times 10^{-5}$, the divergence of the velocity field was kept smaller than $10^{-5}$ and the divergence of the computed electrical current density was less than $10^{-6}$, thus ensuring electric charge conservation.

Since the PIV technique is capable of properly measuring the azimuthal flow, comparison between the experimental and numerical velocity profiles can be done. Figure 3.11 shows the numerically computed and experimentally measured steady-state velocity profiles for $\theta = 90°$. The experimental conditions for this case are $I_0 = 50$ mA and $h = 5$ mm, which can be translated into $Re = 297$ for the numerical code. It can be observed good agreement between both results. In fact, the numerical solution is able to properly reproduce the marked asymmetry of the velocity profile, which

Table 3.1: Terminal velocity for different mesh sizes.

| $n_\theta \times n_r \times n_z$ | $u_T$ (cm/s) | $\lvert u_T - u_m \rvert$ (cm/s) |
|---|---|---|
| $16 \times 16 \times 16$ | 1.92 | 0.13 |
| $32 \times 16 \times 16$ | 1.92 | 0.13 |
| $64 \times 16 \times 16$ | 1.92 | 0.13 |
| $128 \times 16 \times 16$ | 1.92 | 0.13 |
| $16 \times 32 \times 16$ | 2.07 | 0.02 |
| $16 \times 64 \times 16$ | 2.04 | 0.01 |
| $32 \times 32 \times 16$ | 2.07 | 0.02 |
| $32 \times 64 \times 16$ | 2.04 | 0.01 |
| $64 \times 32 \times 16$ | 2.07 | 0.02 |
| $64 \times 64 \times 16$ | 2.04 | 0.01 |
| $128 \times 32 \times 16$ | 2.07 | 0.02 |
| $128 \times 64 \times 16$ | 2.04 | 0.01 |
| $16 \times 16 \times 32$ | 1.93 | 0.12 |
| $16 \times 32 \times 32$ | 2.08 | 0.03 |
| $32 \times 16 \times 32$ | 1.93 | 0.12 |
| $32 \times 32 \times 64$ | 2.08 | 0.03 |
| $32 \times 32 \times 128$ | 2.08 | 0.03 |

has its maximum value close to the outer electrode and a fast decay as the radial distance approaches to the cylinder's axis ($r = 0$). This behavior confirms that, as the highest velocity gradient is closer to the outer electrode, it is more likely for the instability to trigger in this region, which is corroborated experimentally by the appearance of the anticyclonic vortices near the outer cylinder.

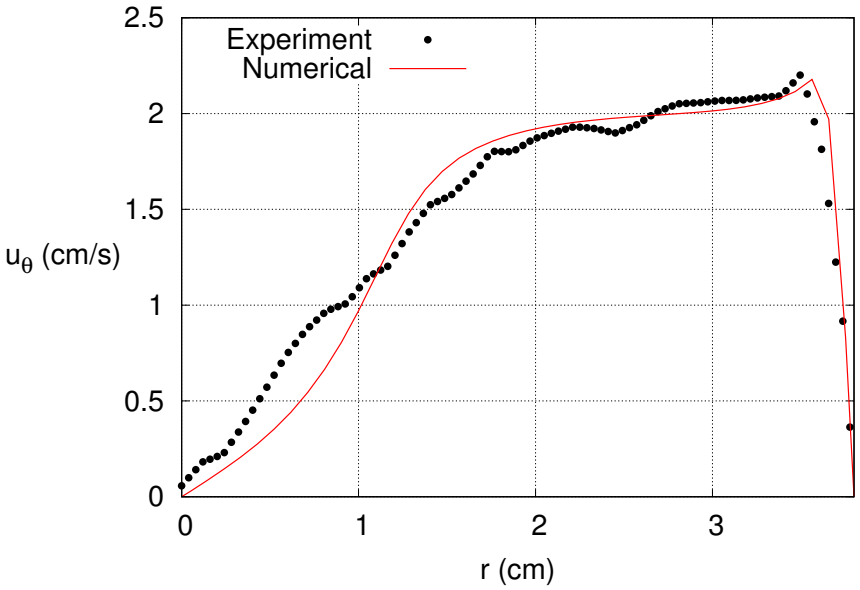


Figure 3.11: Comparison between the numerical and experimental azimuthal velocity profiles as a function of the radial coordinate for an applied electric current of 50 mA and an electrolyte layer thickness of 5 mm ($Re = 297$).

### 3.5.2 Comparison with PIV measurements

As it was shown in Chapter 1, the usual PIV technique is not capable of properly measuring the flow when the instability is triggered, however, far from the vortices, that is, at small radial positions, the flow is mostly azimuthal, thus letting us compare the numerical calculations with the experimental measurements. Figure 3.12 shows the azimuthal component of the velocity as a function of time for two different applied electric currents, 150 mA and 200 mA, and two distinct radial positions, 2.02 cm and 3.1 cm, for an electrolyte layer thickness of 5 mm. In both cases, the electric current intensity is large enough to trigger the instability.

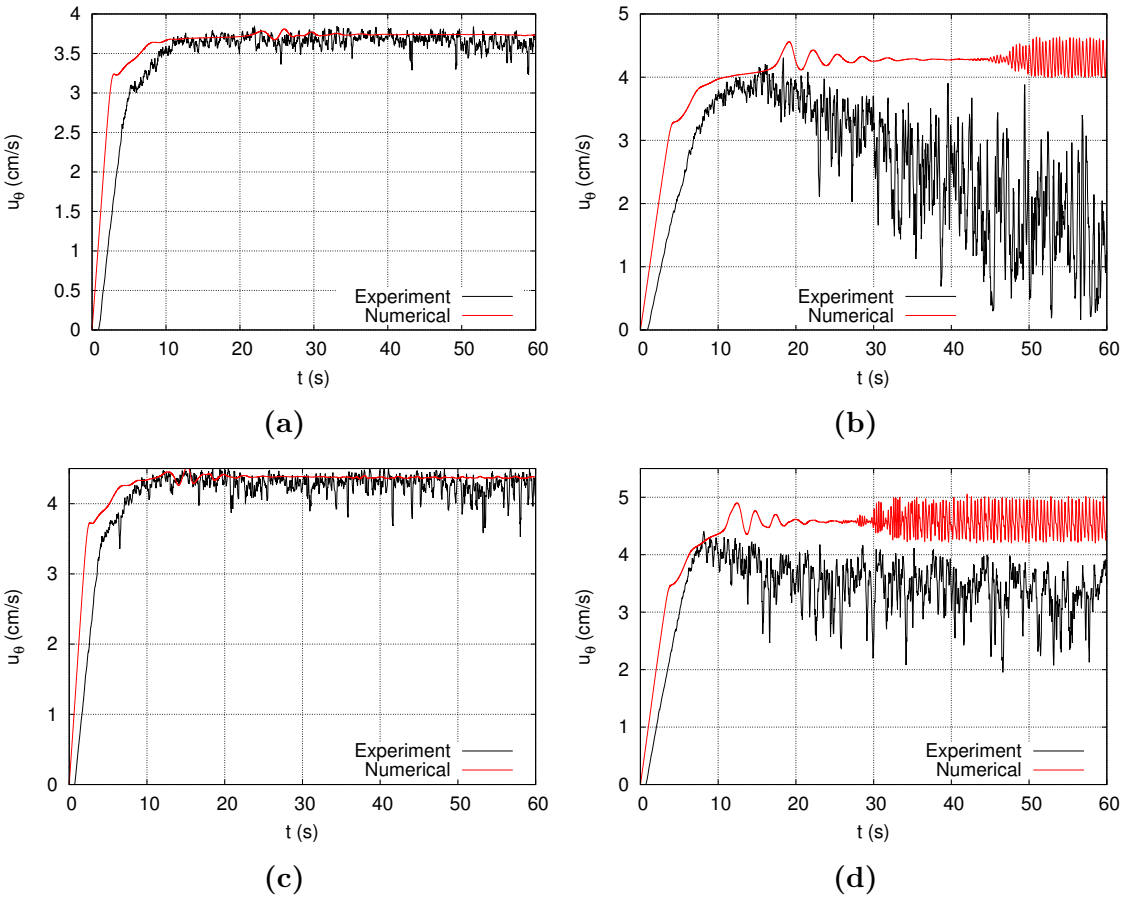


Figure 3.12: Azimuthal velocity component as a function of time for two different electric currents and two different radial positions. $I_0 = 150$ mA for upper row and $I_0 = 200$ mA for lower row. $r = 2.02$ cm for the left column and $r = 3.1$ cm for the right column. The layer thickness is $h = 5$ mm.

The upper row shows the results obtained for a current of 150 mA ($Re = 514$), whereas the lower is for a current of 200 mA ($Re = 594$). The left column shows the azimuthal component located at a radial position of 2.02 cm, where the flow is mostly azimuthal. It can be seen that both experimental and numerical results agree very nicely, even though the experimental results are a bit noisy, specially for the current of 200 mA. For both cases there is a linear growth of the azimuthal velocity for small times but this period seems to be smaller as the applied electric current increases, then the velocity reaches a terminal value. On the other hand, the right column shows the case for a radial position of 3.1 cm, it is clearly seen that the PIV technique is not capable of measuring the velocities once the instability triggers. The numerical results show the appearance of the instability by means of oscillations of almost constant amplitude, thus supporting the idea that the observed vortices can be considered as perturbations growing on a base azimuthal flow.

### 3.5.3 Flow description and comparison with axisymmetric flows

Once the mesh size was selected, simulations were carried out using realistic experimental conditions. Figure 3.13 shows the azimuthal velocity profiles for an applied electric current of 50 mA, for which no instability was observed. Figure 3.13a) shows the azimuthal velocity profile as a function of the radial position at different heights. It can be seen that the maximum velocity near the free surface ($z > 3$ mm) is located close to the outer cylinder, consistently with the experimental velocities measured using PIV at the free surface (see Fig. 3.11). In turn, near the bottom of the container the velocity profiles tend to flatten, and for $z = 1.12$ mm the maximum velocity is closer to the inner cylinder. Figure 3.13b) shows the azimuthal velocity as a function of the axial coordinate for different radial positions. It can be seen that this component presents a non-monotonus behavior since the maximum velocity is not at the free surface, as predicted by the Q2D solutions, but somewhere inside the bulk of the electrolyte layer. In fact, note that these profiles are strikingly different from those found with the Q2D and thin layer approximations (see Section 3.1).

Figure 3.14 presents the visualization of the velocity field at the meridional plane as well as streamlines and the azimuthal vorticity component projected onto this plane. The three-dimensionality of the flow is clearly observed as a large vortex (torus), in which the symmetry is broken due to the different boundary conditions imposed. The fluid rises near the cavity's axis and sinks close to the outer electrode, so that

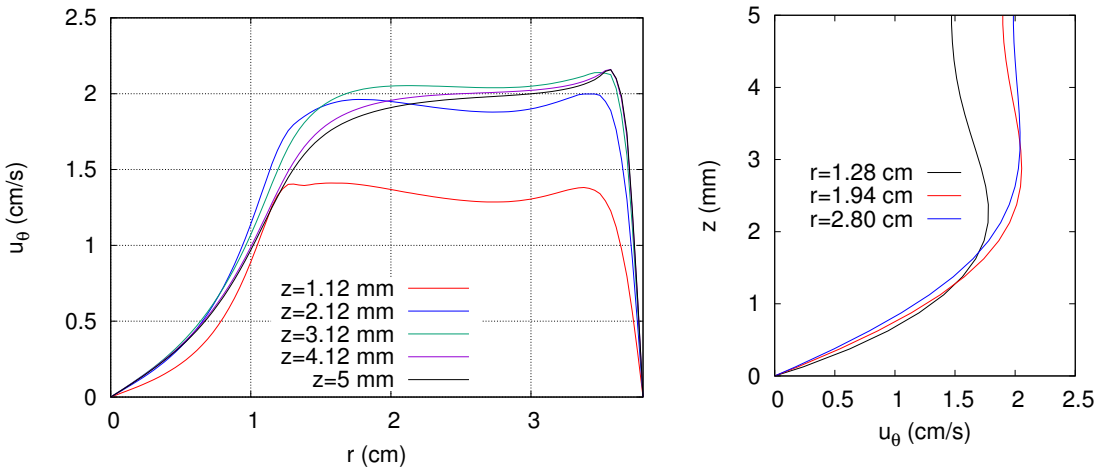


Figure 3.13: Behavior of the azimuthal velocity component as a function of the *a*) radial coordinate for different heights and *b*) axial coordinate for different radii. $I_0 = 50$ mA, $h = 5$ mm.

in the free surface the fluid is moving radially outwards.

It is interesting to look at the other velocity components, $u_r$ and $u_z$, which are shown in Fig. 3.15 as functions of the radial position for different heights. The first thing to notice is that they are one order of magnitude smaller than their azimuthal counterpart, nevertheless, as it was shown in Suslov *et al.* (2017), they have a pronounced effect in the overall flow and even in its stability. It seems that the three-dimensionality of the flow has a strong influence in the onset of the instability. The radial component has negative values near the bottom of the cavity and positive values near the free surface while the axial component presents positive values at the cylinder's axis, due to the rising fluid and negative values near the outer electrode where the fluid goes downwards.

As reported by Suslov *et al.* (2017) two distinct solutions can exist for the same experimental conditions. The first one consists of an axisymmetric flow with one large meridional torus (see Fig. 3.14), whereas the second one shows two counterotating tori in the meridional plane, one large torus covering almost the whole plane, and a smaller one in the upper outer corner of the meridional cross-section. Moreover, the latter flow is more likely to present the observed instability. In fact, this kind of flow was found for all the numerical simulations prior the triggering of the instability, as

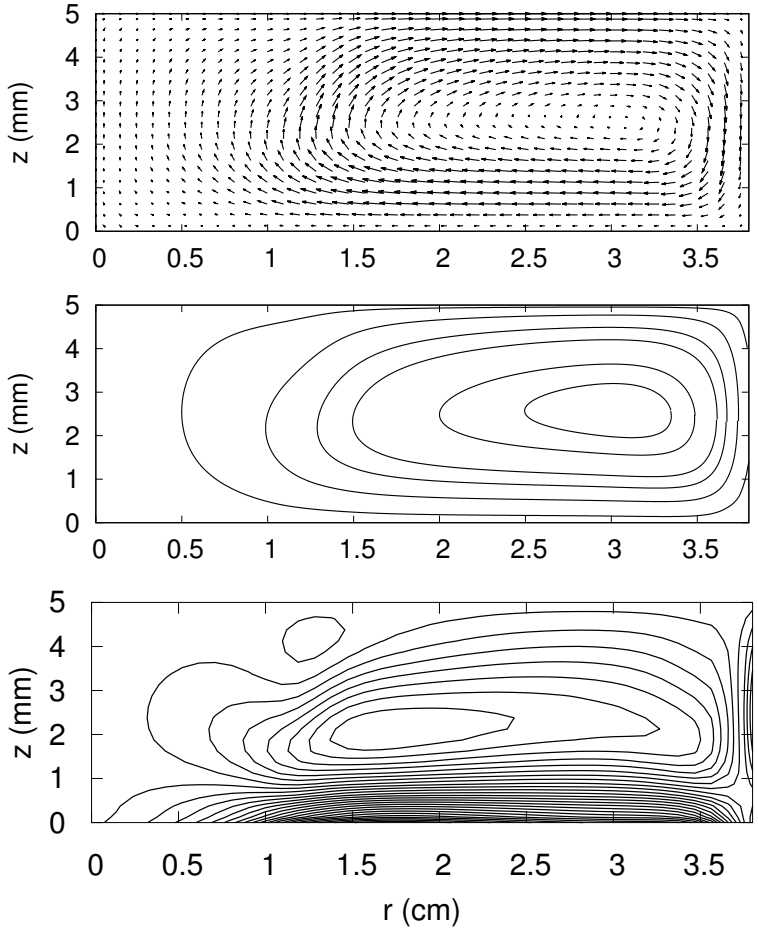


Figure 3.14: Velocity field (top), streamlines (middle) and azimuthal vorticity (bottom) projected onto the meridional $rz$-plane for an applied electric current of 50 mA and a layer thickness of 5 mm.

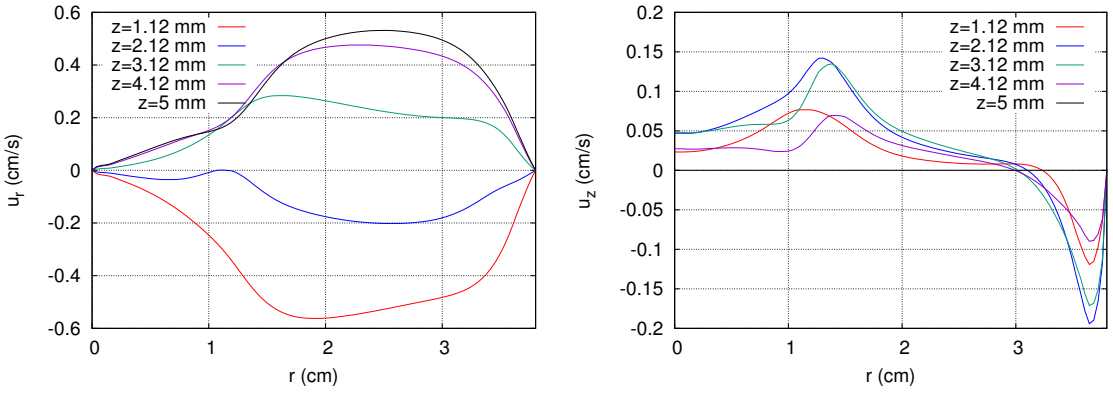


**(a)** **(b)**

Figure 3.15: *a*) Radial and *b*) axial components of the velocity field as functions of $r$ for an applied electric current of 50 mA. $h = 5$ mm.

it is shown if Fig. 3.16, where the velocity field in the meridional plane, streamlines and azimuthal velocity component projected in that plane are shown for $I_0 = 150$ mA and $h = 5$ mm. The corresponding velocity profiles are presented in Figs. 3.16 and 3.17.

The appearance of the smaller secondary vortex creates a noticeable radial counterflow along the free surface, with a radial stagnation point some distance away from the outer cylinder (see Figs. 3.16 and 3.18a). The existence of such a toroidal structure was also indicated by experimental observations: the dye tracer released at the free surface away from the side boundaries drifted towards the outer cylinder, confirming the three-dimensional structure of the flow, with a non-zero radial component, but never reached it and remained at a distance of approximately 12% of the total annular width from the wall, as shown in Fig. 3.19. A careful inspection of the experimental photograph in Fig. 3.19 also indicates that this toroidal vortex is the locus of the instability giving rise to the formation of the anticyclonic vortices seen in Fig. 1.4. Numerical results shown in the following section support this conclusion.

### 3.5.4 Numerical evolution of the instability

In order to compare the numerical simulations with the available experimental observations, a Lagrangian tracking of a passive "ink blob" was implemented. First, the blob was created as a set of particles connected to form a circle at the free surface.

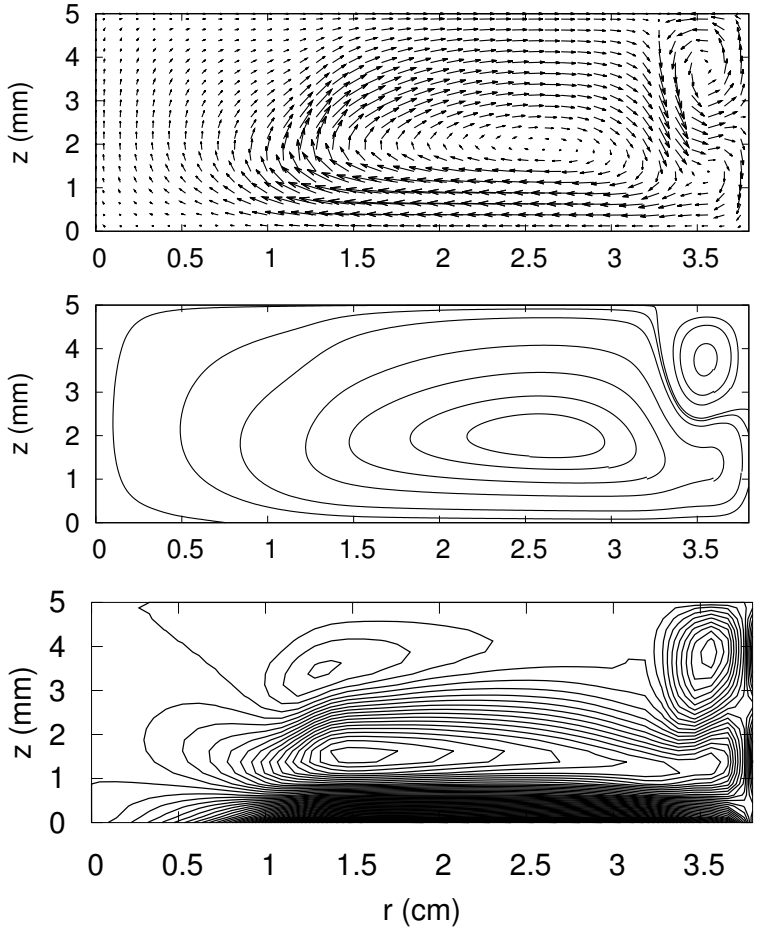


Figure 3.16: Velocity field (top), streamlines (middle) and azimuthal vorticity (bottom) projected onto the meridional $rz$-plane for an applied electric current of 150 mA and a layer thickness of 5 mm prior the triggering of the instability.

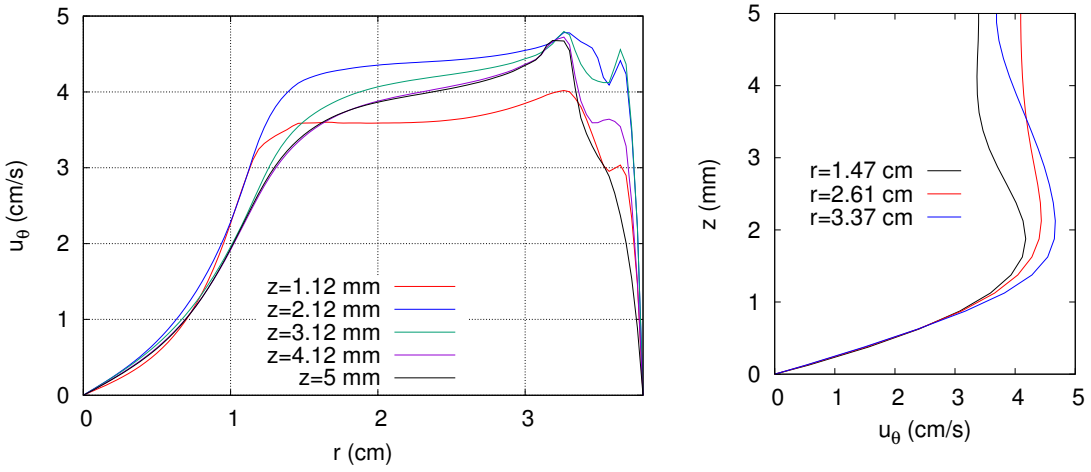


**(a)** **(b)**

Figure 3.17: Behavior of the azimuthal velocity component as a function of the *a*) radial coordinate for different heights and *b*) axial coordinate for different radii. $I_0 = 150$ mA and $h = 5$ mm.

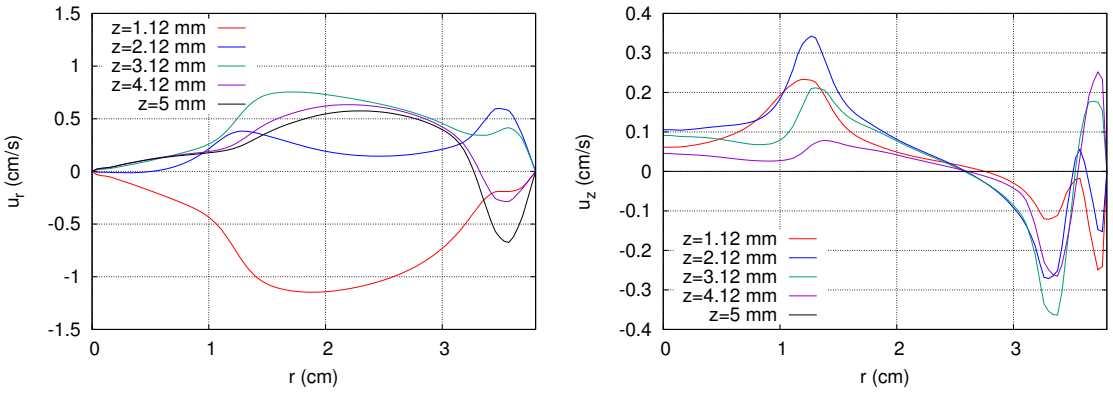


**(a)** **(b)**

Figure 3.18: *a*) Radial and *b*) axial components of the velocity field as functions of $r$ for an applied electric current of 150 mA. $h = 5$ mm. Notice that the radial profiles corresponding to $z = 4.12$ mm and 5 mm account for the stagnation region created by the existence of the secondary vortex in the upper outer corner. Axial profiles are also clearly modified by the presence of this vortex.

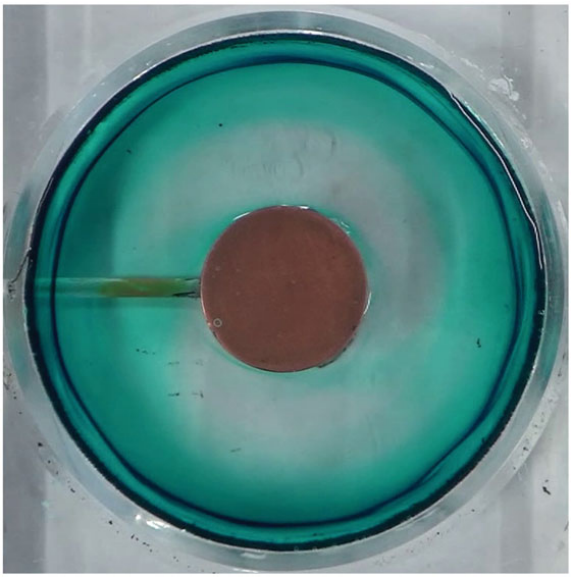

Figure 3.19: Torodial vortex visualization in an electrolyte layer of thickness $h = 5$ mm driven by a radial current of $I_0 = 100$ mA. The stagnation line of the radial flow visible on the free surface as a dark ring was located approximately 3 mm away from the outer electrode.

The velocity field obtained from the numerical solution of the governing equations was used to solve the advection equations for each particle of the blob, namely,

$$\frac{d\mathbf{x}}{dt} = \mathbf{u}. \tag{3.18}$$

Using the position of the corresponding particles at the previous time step as initial condition, the new positions were calculated. This implementation allows to mimic the advection of dye observed in the experiments.

For all the following results, the applied electric current goes radially outwards whereas the axial magnetic field points away from the plane of flow, thus rendering a clockwise Lorentz force.

In Fig. 3.20, the flow evolution leading to the instability is presented through the numerical Lagrangian tracking of an "ink blob" in an electrolyte layer of 5 mm thickness with an applied electric current of 150 mA, which correspond to $Re = 514$. Starting from rest, in the early stages the fluid is advected in the azimuthal direction as a

consequence of the applied Lorentz force. Due to the rotation of the fluid, the tracers are first drifted towards the outer cylinder, but eventually, they are drifted back from the electrode to reach a radial position where an azimuthal flow is established. This state coincides with the experimental picture 3.19. At a later time, the flow destabilizes and anticyclonic vortices appear. Comparing the numerical results with the experimental observations (see Fig. 1.4), some similitudes and differences can be observed. On the one hand, the experimental flow destabilizes long before its numerical counterpart (in about 15 s in contrast with the 50 s needed to destabilize the numerical simulation). On the other hand, the number of vortices observed in both cases is different, being 8 for the experimental case and 12 for the numerical one. Even though the number of vortices predicted numerically does not coincide precisely with the experiment, their qualitative behavior is very close to that observed experimentally. Particularly, the vortices appear closer to the outer electrode and remain almost equidistant from one another. It is worth noting that the axisymmetric flow patterns obtained with the present numerical method (namely, the single torus and the two corotating tori) coincide to those obtained with a different numerical method by Suslov *et al.* (2017) which correspond to two different solutions for the same experimental parameters. This seems to indicate that the problem presents multiple solutions, which could explain the disagreement between the experimental observations and the numerical results.

Varying the applied electric current originates different flow patterns. Figure 3.21 shows the observed anticyclonic vortices for electric current intensities of 150, 200, 250 and 300 mA. In Fig. 3.21a), corresponding to 150 mA, twelve equally spaced vortices can be clearly seen. In Figs. 3.21b) and 3.21c), corresponding to 200 and 250 mA, respectively, ten vortices are observed. Even though the number of vortices is the same, some differences can be identified. For instance, for the case of 200 mA, all the vortices seem to have the same size, whereas for 250 mA there are two diametrically opposite vortices bigger than the rest. The pattern obtained for 300 mA results more complicated and even the number of vortices cannot be identified without ambiguity.

For the sake of illustration, Fig. 3.22 shows a qualitative comparison between the flow patterns obtained through the numerical Lagrangian tracking in conditions where the instability is triggered and experimental images of the instability obtained with the thermographic camera under non-isothermal conditions (see Section 1.4). Although the applied electric currents in the numerical simulation coincide with the experimental cases (150 and 200 mA), the non-isothermal conditions of the experimental flow establish a different physical situation. Nevertheless, it is worth noticing some quali-

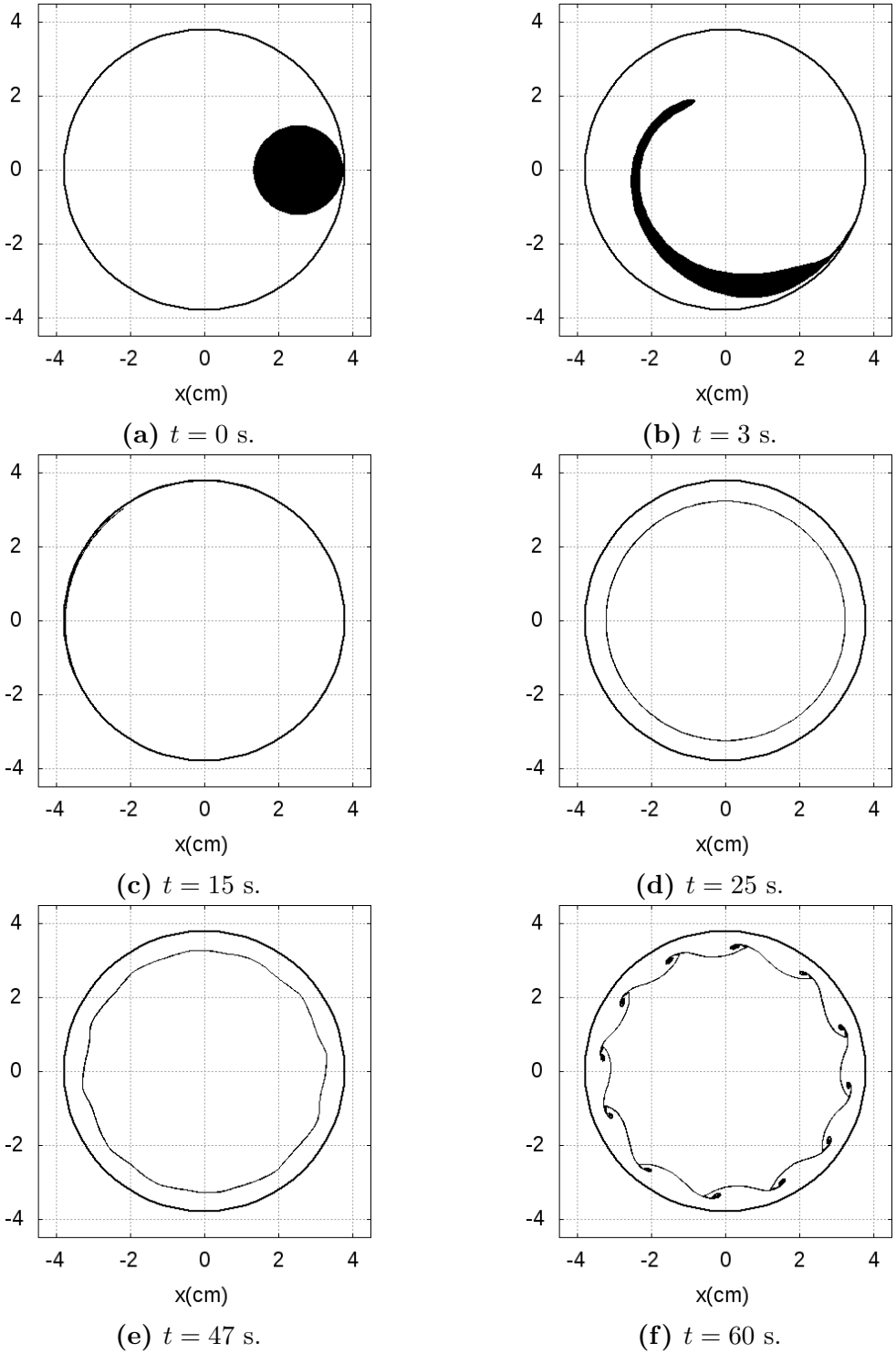


**(a)** $t = 0$ s. **(b)** $t = 3$ s.

**(c)** $t = 15$ s. **(d)** $t = 25$ s.

**(e)** $t = 47$ s. **(f)** $t = 60$ s.

Figure 3.20: Numerical Lagrangian tracking of a "blob" for $Re = 514$ ($I_0 = 150$ mA) which shows the evolution of the instability. ($a$) Initial blob position. ($b$) Early stages of the advected blob. ($c$) Drifting of tracers very close to the outer cylinder. ($d$) Confinement of tracers to a fixed radial position. ($e$) Onset of the instability. ($f$) Formation of anticyclonic vortices.

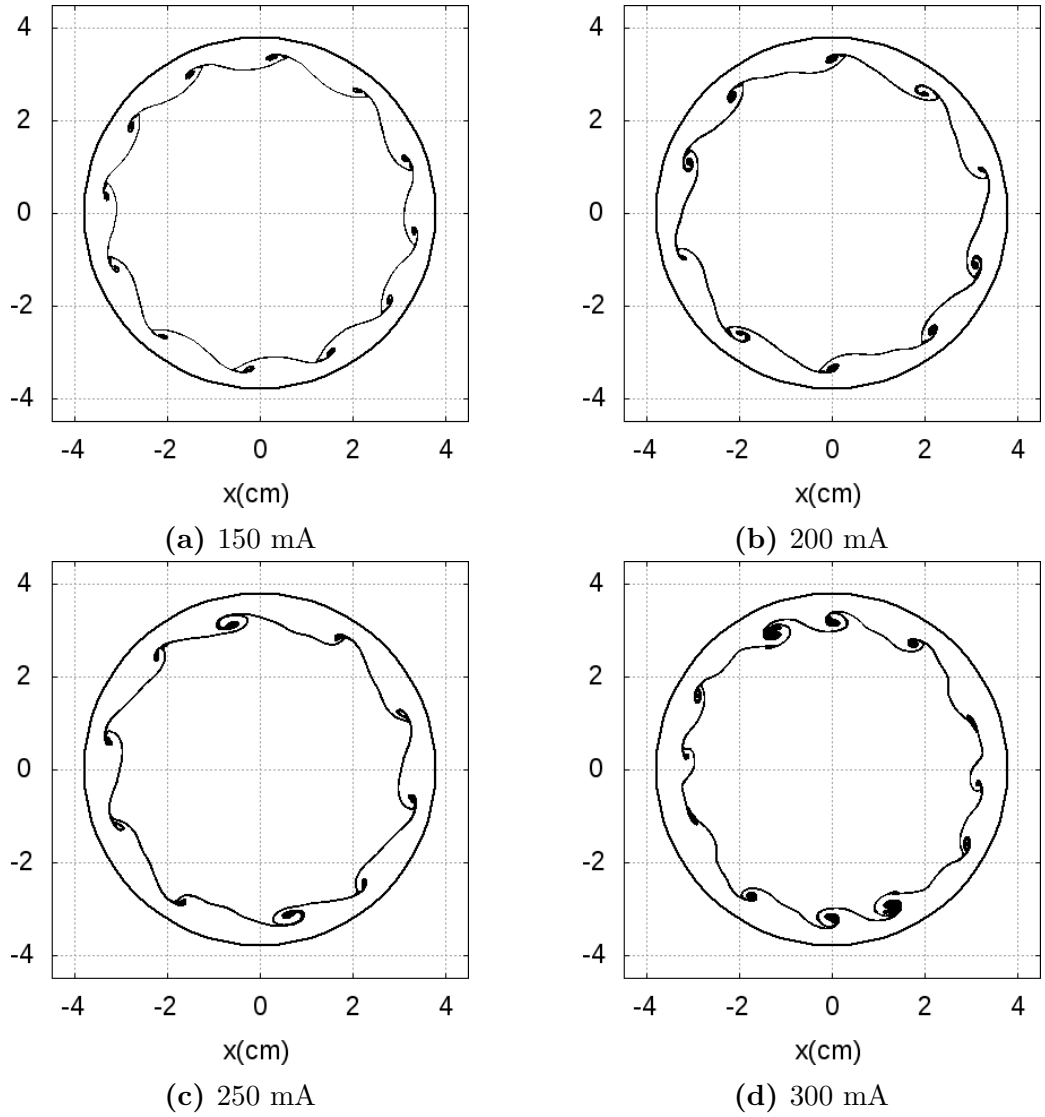


**(a)** 150 mA **(b)** 200 mA

**(c)** 250 mA **(d)** 300 mA

Figure 3.21: Numerical Lagrangian tracking of the flow instability showing different flow patterns for an electrolyte layer thickness of 5 mm and distinct electric currents. *a*) $Re = 514$, *b*) $Re = 594$, *c*) $Re = 664$ and *d*) $Re = 727$.

tative similarities, in particular, the persistance of the instability when heat transfer in present which confirms the robustness of the phenomena. For the case of 150 mA, twelve vortices are predicted in the numerical simulation in contrast with the experimental case where only eight vortices are present. As previously mentioned, this situation might be explained by the existence of multiple solutions [Suslov *et al.* (2017)]. However, for 200 mA the number or vortices appearing in both cases is the same and are qualitatively very similar. These results motivate a deeper exploration of the instability under non-isothermal conditions which could be of interest for heat transfer enhancement purposes.

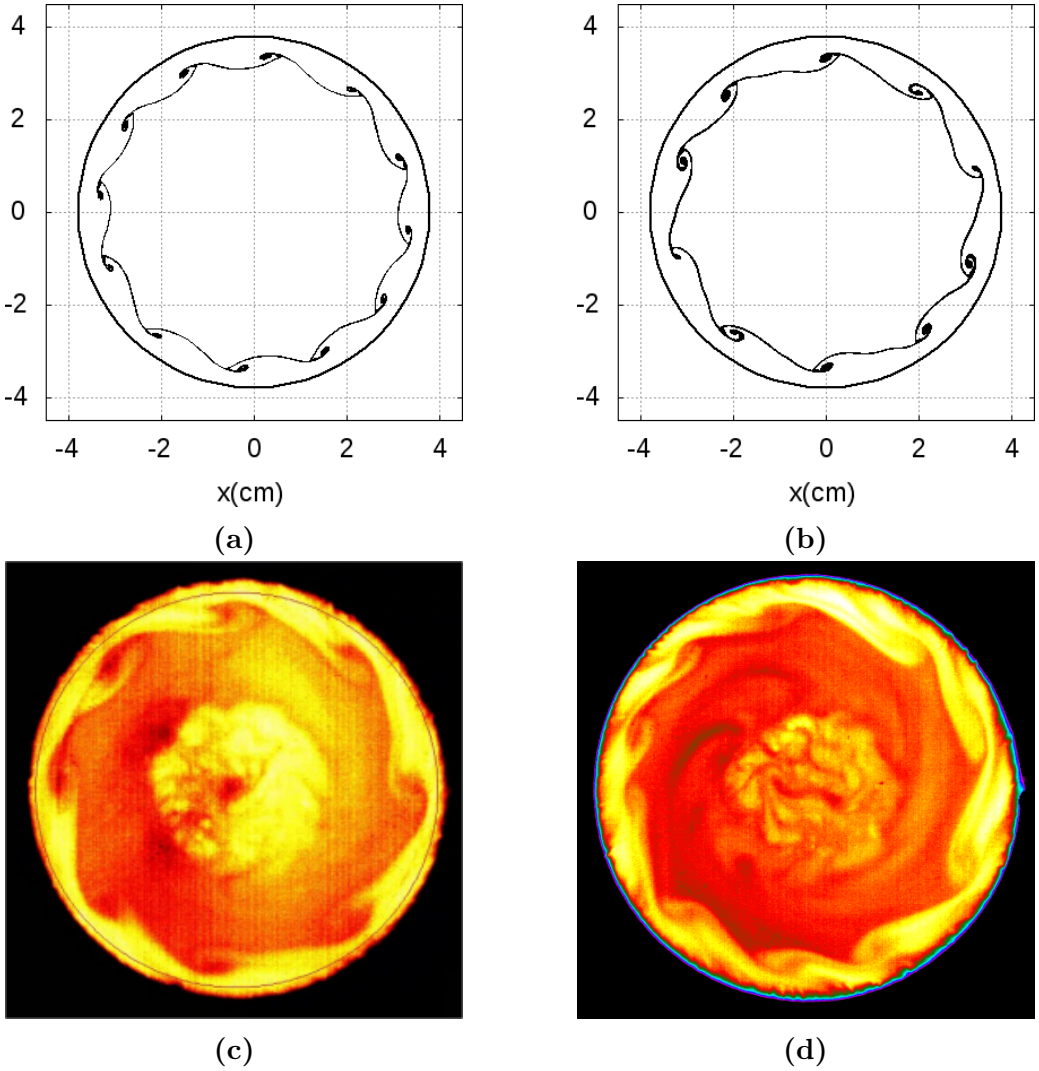


Figure 3.22: Qualitative comparison between the numerical Lagrangian tracking of the flow instability (top row) and experimental images of the instability obtained with the thermographic camera under non-isothermal conditions (bottom row). Left column corresponds to 150 mA and right column to 200 mA.

# Concluding remarks

In this thesis, the flow of a thin electrolyte layer driven by a Lorentz force created by the interaction of a radial electric current and an axial magnetic field was methodologically analyzed experimentally and theoretically. The flow takes place in a cylindrical electromagnetic stirrer with two coaxial electrodes on top of a permanent magnet with uniform polarity. The main goal was the understanding and modeling of a new type of hydrodynamic instability recently discovered experimentally at IER-UNAM. The instability is characterized by the emergence of anticyclonic vortices on a background azimuthal flow and could be of relevance for mixing purposes, heat transfer enhancement, and the modeling of atmospheric phenomena.

Three different experimental techniques were used to obtain information of the flow dynamics. Dye was used as a tracer to visualize the fluid motion near the free surface, while thermographic images allowed to visualize the flow under non-isothermal conditions. Through the variation of the control parameters, namely, the applied electric current and the electrolyte layer thickness, dye visualization allowed to build a map of qualitative behavior in which two distinct regions were identified, namely, a purely azimuthal flow and a flow with a varying number of anticyclonic vortices depending on the experimental conditions. On the other hand, thermographic images revealed the persistence of the instability in non-isothermal conditions and, at least qualitatively, the inferred flow patterns seem indistinguishable from dye visualization. This points out that, in this case, although heat transfer is present, is not able to inhibit the emergence of the instability. In turn, quantitative information obtained from PIV measurements was used to validate numerical simulations and establish the characteristic scales of velocity in the experimental flow. However, the PIV technique failed to accurately capture the velocity field once the flow instability is triggered. This failure motivated the development of an improved processing technique of the recorded images that is able to resolve the flow structures that appear as a consequence of the instability. The technique is currently under development

and will be published in the near future.

As a complement, the shear flow created by the use of an array of two concentric cylindrical magnets with opposite polarities was also qualitatively explored. It resulted in the appearance of a tripolar vortex similar to others reported for hydrodynamic cases [Van Heijst *et al.* (1991), Samimy *et al.* (2003)]. In contrast to results obtained with a magnet with uniform polarity, in this case flow patterns inferred from thermographic images revealed drastic changes with respect to dye visualization experiments, indicating a major impact of heat transfer. In any case, the use of thermographic images seems to be an useful tool to complement the information required for the analysis of flow dynamics problems, but its accuracy and potential application is still to be assessed.

Considering a simplified version of the studied problem, an analytical Q2D solution with general slip boundary conditions was obtained for both an electrolyte and a liquid metal. These solutions could be used as a starting point for microfluidic mixing related studies, since they are based on less idealized assumptions than previous investigations [Gleeson *et al.* (2004), Gleeson (2005)]. On the other hand, it was found that thin-layer approximations such as depth-averaged models and quasi-two-dimensional treatments are quickly invalidated as the thickness of the layer increases, and cannot adequately describe even qualitative features of the flow such as the velocity profiles observed in experiments. The flows remain axisymmetric but become essentially three-dimensional, and have to be treated as such by employing the appropiate numerical algorithms as the one developed in this work. This involved, in the first place, the use of a realistic magnetic field distribution that reproduces accurately the experimental meaurements. A hybrid finite volume - Fourier spectral numerical technique was implemented for the solutions of the equations governing the flow produced in the electromagnetic stirrer. One of the main contributions of the present work was the succesful numerical simulation of the three-dimensional dynamics of the flow. This includes the accurate reproduction of the main patterns of the axisymmetric flow, as well as the flow evolution leading to the instability. Numerical results were compared with experimental observations through the Lagrangian tracking of a passive scalar tracer that simulates the advection of dye in the experiment, finding good qualitative agreement. Nevertheless, there are still some interesting challenges for the future work, particularly, the fact that the number of vortices predicted by the simulation does not coincide in all cases with experimental observations. Also, the extension of the numerical algorithm to include the heat transfer analysis of non-isothermal advection flows seems an interesting project for future studies. Although the description of some scenarios for the appearance of the

instability was advanced in [Suslov *et al.* (2017)], a complete stability analysis is still a pending task.

Appendix A

# Mathematical problem formulation

This appendix describes the mathematical formulation of the problem under consideration. It starts with a brief description of the governing equations of a Newtonian, incompressible fluid. Next, the equations of the electromagnetic field are explained and combined alongside the fluid mechanics equations using the so-called MHD approximation to get the fundamental MHD equations. Finally, the equations are expressed in terms of the electric potential $\phi$, pressure and velocity fields.

## A.1 Equations of fluid dynamics

Fluid dynamics is aimed to describe the flow of fluids (liquids or gases) subjected to the action of external agents such as body forces, pressure gradients or temperature differences. From a macroscopic view, the *continuum hypothesis* holds, so that fluid variables (pressure, temperature, velocity, among others) can be univocally defined at any spatial point and any instant of time, disregarding the microscopic behavior. In this way, the fundamental physical laws of mass conservation, Newton's second law of motion and the first law of thermodynamics, alongside the constitutive equations and thermodynamic relations from local equilibrium, can be used to obtain a set of equations which describes the spatio-temporal behavior of fluids [Currie (2007)].

In many practical applications, both liquids and gases can be considered as incompressible, which means that its mass density remains constant. Application of mass conservation to an incompressible fluid results in the *continuity equation*:

$$\nabla \cdot \mathbf{u} = 0, \tag{A.1}$$

where $\mathbf{u}$ is the velocity vector field which, in general, is space- and time-dependent.

In many cases, the working fluid can be considered as Newtonian, this means that there is a linear relationship between the shear stress applied to the fluid and the

rate of strain. This is the case for the most common electrically conducing fluids: electrolytes and liquid metals. Application of Newton's second law of motion to a Newtonian fluid results in the well-known *Navier-Stokes equation*:

$$\rho\left(\frac{\partial \mathbf{u}}{\partial t} + (\mathbf{u}\cdot\nabla)\mathbf{u}\right) = -\nabla p + \eta\nabla^2\mathbf{u} + \rho\mathbf{f}, \tag{A.2}$$

where $\rho$ and $\eta$ are the mass density and dynamic viscosity of the fluid, respectively; $p$ is the scalar pressure field and $\mathbf{f}$ is used to represent any body force acting upon the fluid.

For a Newtonian fluid, the first law of thermodynamics leads to the heat transfer equation, namely,

$$\frac{\partial T}{\partial t} + (\mathbf{u}\cdot\nabla)\,T = \alpha\nabla^2 T + S, \tag{A.3}$$

where $T$ is the scalar temperature field, $\alpha$ is the thermal diffusivity of the fluid and $S$ represents any source of heat due to viscous or ohmic dissipation.

## A.2 Equations of the electromagnetic field

The behavior of electric and magnetic fields is described, in general, by means of relativistic equations, nevertheless, in MHD phenomena at laboratory and industrial scales, the characteristic velocities are much smaller than the speed of light. In what follows, we briefly present the electromagnetic field equations and then the MHD approximation that allows to obtain the fundamental MHD equations.

### A.2.1 Maxwell's equations

Maxwell's equations are a set of partial differential equations describing the spatio-temporal behavior of electric and magnetic fields and are considered among the most influential equations in science [Fleisch (2008)]. For a homogeneous, isotropic, linear medium these equations are expressed as

$$\nabla\cdot\mathbf{E} = \frac{\rho_e}{\epsilon}, \tag{A.4}$$

$$\nabla\cdot\mathbf{B} = 0, \tag{A.5}$$

$$\nabla \times \mathbf{E} = -\frac{\partial \mathbf{B}}{\partial t}, \tag{A.6}$$

$$\nabla \times \mathbf{B} = \mu \mathbf{j} + \mu\epsilon \frac{\partial \mathbf{E}}{\partial t}. \tag{A.7}$$

Equation (A.4) is *Gauss' law* for the electric field, where $\mathbf{E}$ is the electric field, $\rho_e$ is the total electric charge density and $\epsilon$ is the permitivity of the material medium. This equation shows that the electric fields are produced by the electric charges in such a way that the positive charges are "sources" of electric fields, whereas negative charges are "sinks" of such fields. Equation (A.5) states the nonexistence of magnetic monopoles, that is to say, magnets always posses two opposite poles, $\mathbf{B}$ being the magnetic induction vector field. Equation (A.6), known as *Faraday's law of induction*, expresses that the temporal variation of a magnetic field is capable of producing an electric field. Finally, Equation (A.7) is the *Ampère-Maxwell law* which expresses that a magnetic field can be produced by a stationary current density $\mathbf{j}$ and by a time-varying electric field. In this equation $\mu$ is the magnetic permeability of the medium. For non-magnetizable materials, such as the electrolytes and liquid metals, a good approximation is to consider $\mu = \mu_0$, $\mu_0$ being the magnetic permeability of free space [Davidson (2001)]. It is worth mentioning that the time-dependent term in Equation (A.7) is a relativistic term known as Maxwell's displacement current, where $1/(\mu\epsilon) = c^2$, $c$ being the speed of light.

Note that taking the divergence of Equation (A.7) and using Gauss' law for the electric field (Eq. A.4) results in

$$\nabla \cdot \mathbf{j} + \frac{\partial \rho_e}{\partial t} = 0. \tag{A.8}$$

This equation manifests *electric charge conservation*, that is to say, electric charge is not created nor destroyed.

### A.2.2 Ohm's law

Ohm's law is a constitutive equation which establishes that the electric current density inside an stationary conductor is proportional to the net force exerted upon its

free charges [Davidson (2001)], and therefore, proportional to the applied electric field, that is,

$$\mathbf{j} = \sigma \mathbf{E}', \tag{A.9}$$

where the proportionality constant $\sigma$ is a material property of the conductor known as electrical conductivity and $\mathbf{E}'$ is the electric field. When the conductor is moving with velocity $\mathbf{u}$ with respect to a reference frame, Ohm's law is modified considering the effective field measured from such a frame, that is,

$$\mathbf{j} = \sigma(\mathbf{E} + \mathbf{u} \times \mathbf{B}) + \rho_e \mathbf{u}, \tag{A.10}$$

where the first term of the right-hand side is the effective electric field and the second term is the convection current [Cuevas (2004)].

### A.2.3 The Lorentz force

In a material medium with an electric charge density $\rho_e$ through which an electric current density $\mathbf{j}$ flows, the electromagnetic force per unit volume acting upon such medium is given by

$$\mathbf{f} = \rho_e \mathbf{E} + \mathbf{j} \times \mathbf{B}. \tag{A.11}$$

This body force is known as *Lorentz force*.

## A.3 The MHD approximation

To study MHD phenomena is necessary to couple both equations for fluid dynamics and electromagnetism. Flows studied in classical fluid dynamics occur at very low velocities compared to the speed of light and the governing equations are Galilean invariant, whereas Maxwell's equations are relativistic and Lorentz invariant. To couple both set of equations, the so-called *MHD approximation* is used. This approximation is based on the following considerations:

1. Fluid motion is non relativistic, that is, the characteristic velocities of the flows are much smaller than the speed of light ($|\mathbf{u}| \ll c$).
2. Flows take place in quasi-stationary magnetic fields or fields that vary at low frequencies.

3. The electric fields are of the order of magnitude of the electromotive force induced by the fluid motion, that is, $\mathbf{u}\times\mathbf{B}$.

Taking into account the above assumptions, it is possible to simplify the set of equations in such a way that the resulting system is Galilean invariant so that the Maxwell's displacement current, the electric force $\rho_e\mathbf{E}$ and the convection current $\rho_e\mathbf{u}$, can be neglected [Cuevas (2004)].

With the previous considerations, the equations governing the behavior of a non-magnetizable, electrically conducting fluid under the action of a magnetic field can be reduced to

$$\nabla\cdot\mathbf{B} = 0 \quad , \quad \nabla\times\mathbf{E} = -\frac{\partial\mathbf{B}}{\partial t}, \tag{A.12}$$

$$\nabla\times\mathbf{B} = \mu_0\mathbf{j} \quad , \quad \mathbf{j} = \sigma(\mathbf{E}+\mathbf{u}\times\mathbf{B}), \tag{A.13}$$

$$\nabla\cdot\mathbf{u} = \mathbf{0}, \tag{A.14}$$

$$\rho\left(\frac{\partial\mathbf{u}}{\partial t} + (\mathbf{u}\cdot\nabla)\mathbf{u}\right) = -\nabla p + \eta\nabla^2\mathbf{u} + \mathbf{j}\times\mathbf{B}. \tag{A.15}$$

Note that taking the divergence of Ampère's law results in

$$\nabla\cdot\mathbf{j} = 0, \tag{A.16}$$

which states the conservation of electric charge for the considered approximation.

## A.4 The $\phi$ - Formulation ($Rm \ll 1$)

Electrically conducting fluids of interest for the research being developed at the Renewable Energy Institute are electrolytes and liquid metals. One of the main differences between these two types of conducting fluids lies in their electrical conductivity, being very small for electrolytes and about six orders of magnitude larger for liquid metals. The difference in the conductivities of these fluids allows different mathematical approximations and simplifications to the governing equations.

A dimensionless parameter of major importance in MHD is the *magnetic Reynolds number* defined as

$$R_m = \frac{u_c L}{\eta_m} = \mu_0\sigma u_c L, \tag{A.17}$$

where $\eta_m = 1/\mu_0\sigma$ is the magnetic diffusivity, $L$ and $u_c$ are characteristic scales of length and velocity, respectively. This parameter can be interpreted as the ratio of the induced and applied magnetic fields [Davidson (2001)].

Commonly, in electrolyte or liquid metal flows, both at laboratory and industrial scales, the magnetic field induced by the fluid motion under the applied fied is very small when compared with the latter, therefore, $R_m \ll 1$. This means that the applied magnetic field is not modified by the fluid motion.

Under this approximation, Faraday's law is reduced to

$$\nabla \times \mathbf{E} = 0, \tag{A.18}$$

and therefore, the electric field is potential, so that

$$\mathbf{E} = -\nabla\phi, \tag{A.19}$$

where $\phi$ represents the electric potential inside the fluid.

Using Equation (A.19), Ohm's law can be rewritten as

$$\mathbf{j} = \sigma\left(-\nabla\phi + \mathbf{u}\times\mathbf{B}_0\right). \tag{A.20}$$

Taking the divergence of the above equation and using the conservation of electric charge (Eq. A.16), a Poisson equation for the electric potential is obtained:

$$\nabla^2\phi = \nabla\cdot(\mathbf{u}\times\mathbf{B}_0). \tag{A.21}$$

Note that, the applied magnetic field must satisfy the magnetostatic equations

$$\nabla\cdot\mathbf{B}_0 = 0 \quad , \quad \nabla\times\mathbf{B}_0 = 0. \tag{A.22}$$

In summary, the fundamental MHD equations expressed in terms of the velocity field, pressure and electric potential as primitive variables, corresponding to the so-called $\phi$ - formulation [Smolentsev *et al.* (2010)] are

$$\nabla\cdot\,\mathbf{u} = 0, \tag{A.23}$$

$$\rho\left(\frac{\partial\mathbf{u}}{\partial t} + (\mathbf{u}\cdot\nabla)\mathbf{u}\right) = -\nabla p + \eta\nabla^2\mathbf{u} + \mathbf{j}\times\mathbf{B}, \tag{A.24}$$

$$\mathbf{j} = \sigma\left(-\nabla\phi + \mathbf{u}\times\mathbf{B}_0\right), \tag{A.25}$$

$$\nabla^2\phi = \nabla\cdot(\mathbf{u}\times\mathbf{B}_0), \tag{A.26}$$

which is a complete system that can be solved if suitable boundary and initial conditions are suplied, as it is done analytically and numerically in Chapters 2 and 3, respectively, for the electromagnetically driven flow in the annular container.

Appendix B

# The Fourier-Galerkin - Finite Volume method

The numerical solution of the governing equations was obtained by means of a hybrid methodology, which was proposed and has been succesfully applied to heat transfer and MHD problems by Nuñez *et al.* (2012). Since the geometry of the problem imposes periodicity in the azimuthal direction, it is natural to implement a Fourier spectral method in the $\theta$-direction. After that, the resulting equations are discretized using a standard Finite Volume methodology. For the purposes of describing the numerical method, only the 2D case will be presented with the unserstanding that the extension to 3D problems (such as the one reported in the present thesis) is straightforward. Detailed explanations on the application of the spectral approximation can be found in Peyret (2002), Canuto *et al.* (2006) and Korpiva (2009) whereas the finite volume method is extensively described in Versteeg & Malalasekera (1995).

## B.1 Preliminary treatment of the governing equations

We start from the 2D governing Navier-Stokes equations in cylindrical coordinates

$$\frac{1}{r}\frac{\partial\left(ru_r\right)}{\partial r}+\frac{1}{r}\frac{\partial u_\theta}{\partial\theta}=0, \tag{B.1}$$

$$\frac{\partial u_r}{\partial t}+\left(\mathbf{u}\cdot\nabla\right)u_r-\frac{u_\theta^2}{r}=-\frac{\partial p}{\partial r}+\frac{1}{Re}\left(\nabla^2u_r-\frac{u_r}{r^2}-\frac{2}{r^2}\frac{\partial u_\theta}{\partial\theta}\right)+f_r, \tag{B.2}$$

$$\frac{\partial u_\theta}{\partial t}+\left(\mathbf{u}\cdot\nabla\right)u_\theta+\frac{u_ru_\theta}{r}=-\frac{1}{r}\frac{\partial p}{\partial\theta}+\frac{1}{Re}\left(\nabla^2u_\theta-\frac{u_\theta}{r^2}+\frac{2}{r^2}\frac{\partial u_r}{\partial\theta}\right)+f_\theta, \tag{B.3}$$

where $u_\theta$ and $u_r$ are the azimuthal and radial components of the velocity field, respectively; $f_r$ and $f_\theta$ represent external forces acting upon the fluid in the respective directions and the operators are defined as

$$(\mathbf{u}\cdot\nabla) = u_r\frac{\partial}{\partial r} + \frac{u_\theta}{r}\frac{\partial}{\partial\theta}, \tag{B.4}$$

$$\nabla^2 = \frac{1}{r}\frac{\partial}{\partial r}\left(r\frac{\partial}{\partial r}\right) + \frac{1}{r^2}\frac{\partial^2}{\partial\theta^2}. \tag{B.5}$$

In order to solve the system of equations, it must be rewritten in a simpler, more convenient form

$$\frac{1}{r}\frac{\partial(rv)}{\partial r} + \frac{1}{r}\frac{\partial u}{\partial\theta} = 0, \tag{B.6}$$

$$\frac{\partial v}{\partial t} + N_v = -\frac{\partial p}{\partial r} + \Gamma\nabla^2 v - \frac{\Gamma}{r^2}v + \Gamma L_v, \tag{B.7}$$

$$\frac{\partial u}{\partial t} + N_u = -\frac{1}{r}\frac{\partial p}{\partial\theta} + \Gamma\nabla^2 u - \frac{\Gamma}{r^2}u + \Gamma L_u, \tag{B.8}$$

with $\Gamma = 1/Re$, $u = u_\theta$ y $v = u_r$, from where it is easy to find that

$$N_v = (\mathbf{u}\cdot\nabla)\,v - \frac{u^2}{r}, \quad L_v = -\frac{2}{r^2}\frac{\partial u}{\partial\theta} + f_r, \tag{B.9}$$

$$N_u = (\mathbf{u}\cdot\nabla)\,u + \frac{uv}{r}, \quad L_u = \frac{2}{r^2}\frac{\partial v}{\partial\theta} + f_\theta, \tag{B.10}$$

where the letters $L$ and $N$ are used to indicate linear and nonlinear terms in the governing equations, respectively.

## B.2 Fourier series expansion and Galerkin approximation

Taking advantage of the periodicity of the problem, the important quantities can be expanded by means of a truncated Fourier series with $n_\theta$ terms:

$$p = \sum_{k=-n_\theta/2}^{n_\theta/2-1} \hat{p}_k e^{ik\theta}, \tag{B.11}$$

$$u = \sum_{k=-n_\theta/2}^{n_\theta/2-1} \hat{u}_k e^{ik\theta}, \quad N_u = \sum_{k=-n_\theta/2}^{n_\theta/2-1} \hat{N}_{uk} e^{ik\theta}, \quad L_u = \sum_{k=-n_\theta/2}^{n_\theta/2-1} \hat{L}_{uk} e^{ik\theta}, \tag{B.12}$$

$$v = \sum_{k=-n_\theta/2}^{n_\theta/2-1} \hat{v}_k e^{ik\theta}, \quad N_v = \sum_{k=-n_\theta/2}^{n_\theta/2-1} \hat{N}_{vk} e^{ik\theta}, \quad L_v = \sum_{k=-n_\theta/2}^{n_\theta/2-1} \hat{L}_{vk} e^{ik\theta}, \tag{B.13}$$

with $\hat{p}_k$, $\hat{u}_k$, $\hat{v}_k$, $\hat{N}_{uk}$, $\hat{N}_{vk}$, $\hat{L}_{uk}$ and $\hat{L}_{vk}$ as the expansion coefficients for the respective variables. It is worth noting that these coefficients depend on the radial coordinate and time only, whereas the angular dependence is kept in the complex exponential functions.

Substituting equations (B.11) - (B.13) into the governing equations (B.6) - (B.8), multiplying by the complex conjugates of the exponential functions, integrating over the interval $\theta \in [0, 2\pi]$ and using the orthogonality property (Galerkin approximation),

$$\left(e^{ikx}, e^{ilx}\right) = \int_0^{2\pi} e^{ikx} e^{-ilx} dx = \int_0^{2\pi} e^{i(k-l)x} dx = 2\pi\delta_{kl} = \begin{cases} 2\pi, & \text{if } k = l, \\ 0, & \text{if } k \neq l, \end{cases} \tag{B.14}$$

results in a set of equations for each wavenumber $k$:

$$\frac{1}{r}\frac{\partial(r\hat{v})}{\partial r} + \frac{ik}{r}\hat{u} = 0, \tag{B.15}$$

$$\frac{\partial \hat{v}}{\partial t} + \hat{N}_v = -\frac{\partial \hat{p}}{\partial r} + \Gamma\left[\frac{1}{r}\frac{\partial}{\partial r}\left(r\frac{\partial \hat{v}}{\partial r}\right) - \frac{k^2}{r^2}\hat{v} - \frac{1}{r^2}\hat{v}\right] + \Gamma\hat{L}_v, \tag{B.16}$$

$$\frac{\partial \hat{u}}{\partial t} + \hat{N}_u = -\frac{ik}{r}\hat{p} + \Gamma\left[\frac{1}{r}\frac{\partial}{\partial r}\left(r\frac{\partial \hat{u}}{\partial r}\right) - \frac{k^2}{r^2}\hat{u} - \frac{1}{r^2}\hat{u}\right] + \Gamma\hat{L}_u, \tag{B.17}$$

where the subscript $k$ as well as its range have been omitted for simplicity. A very important feature of the system (B.15) - (B.17) is that it does not depend on $\theta$ anymore, that is, the number of spatial variables was dimished by one, thus turning a two dimensional, time-dependent problem into a set of one-dimensional ones. Note that the new variables of these systems are the Fourier expansion coefficients rather than the physical quantities, so from now on the problem is discretized and solved in Fourier space.

## B.3 Finite Volume discretization in Fourier space

To obtain the discrete linear equations, the system (B.15) - (B.17) is integrated in a control volume according to the classical finite volume method. In order to avoid unphysical solutions due to the so-called *checkerboard effect*, is it costumary to use a *staggered grid* as the one shown in Fig. B.1, where it can be seen that the Fourier coefficients for the pressure and $u$ component (in black) are located at the same point, whereas the $v$ component (in blue) is placed half a control volume above, thus, two different grids are used to solve the equations.

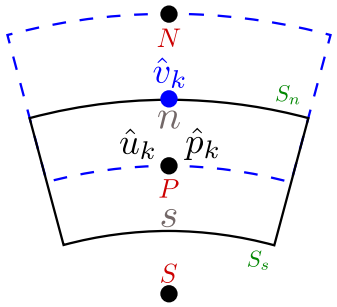


Figure B.1: Staggered grid for the variables in the control volume. Uppercase red letters are used to indicate the centers of the control volumes ($N$ and $S$ refer to the north and south neighboring points, respectively), whereas lowercase gray letters are used to denote the middle point of the boundaries of the control volume $P$. $S_n$ and $S_s$ are the surface area of the north and south boundaries, respectively.

Using a first order differencing scheme for time discretization and the middle-point rule for the diffusive term, the equation for the $u$ component can be rewritten as

$$\int_{\Delta V} \frac{\partial \hat{u}}{\partial t} dV + \int_{\Delta V} \hat{N}_u dV = -\int_{\Delta V} \frac{ik}{r} \hat{p} dV + \Gamma \int_{\Delta V} \left[ \frac{1}{r} \frac{\partial}{\partial r} \left( r \frac{\partial \hat{u}}{\partial r} \right) - \frac{k^2+1}{r^2} \hat{u} \right] dV + \Gamma \int_{\Delta V} \hat{L}_u dV, \quad \text{(B.18)}$$

$$\frac{\hat{u}_P - \hat{u}_P^0}{\Delta t} \Delta V + \hat{N}_{uP}^0 \Delta V = -\frac{ik}{r_P} \hat{p}_P \Delta V + \Gamma \left( \frac{S_n}{\Delta r} (\hat{u}_N - \hat{u}_P) - \frac{S_s}{\Delta r} (\hat{u}_P - \hat{u}_S) - \frac{k^2+1}{r_P^2} \Delta V \hat{u}_P \right) + \Gamma \hat{L}_{uP}^0 \Delta V, \quad \text{(B.19)}$$

where the superscript "zero" is used to indicate the previous time step and the subscripts $P$, $N$ and $S$ represent the centers of the control volume and its corresponding north and south neighbors, respectively (see Fig. B.1). The above equation can be

rewritten in the form

$$a_P\hat{u}_P = a_N\hat{u}_N + a_S\hat{u}_S - \frac{ik}{r_P}\hat{p}_P\Delta V + \hat{S}_{up}, \tag{B.20}$$

with

$$a_N = \frac{\Gamma S_n}{\Delta r}, \quad a_S = \frac{\Gamma S_s}{\Delta r}, \quad \hat{S}_{uP} = \hat{u}_P^0\frac{\Delta V}{\Delta t} + \Gamma\hat{L}_{uP}^0\Delta V - \hat{N}_{uP}^0\Delta V, \tag{B.21}$$

$$a_P = a_N + a_S + \Gamma\frac{k^2+1}{r_P^2}\Delta V + \frac{\Delta V}{\Delta t}. \tag{B.22}$$

Similarly, the equation for the $v$ component is expressed as

$$a_P\hat{v}_P = a_N\hat{v}_N + a_S\hat{v}_S - \frac{\hat{p}_n - \hat{p}_s}{\Delta r}\Delta V + \hat{S}_{vp}, \tag{B.23}$$

where

$$a_N = \frac{\Gamma S_n}{\Delta r}, \quad a_S = \frac{\Gamma S_s}{\Delta r}, \quad \hat{S}_{vP} = \hat{v}_P^0\frac{\Delta V}{\Delta t} + \Gamma\hat{L}_{vP}^0\Delta V - \hat{N}_{vP}^0\Delta V, \tag{B.24}$$

$$a_P = a_N + a_S + \Gamma\frac{k^2+1}{r_P^2}\Delta V + \frac{\Delta V}{\Delta t}. \tag{B.25}$$

The discrete continuity equation (Eq. B.15) is

$$\hat{v}_n S_n - \hat{v}_s S_s + \frac{ik}{r_P}\Delta V\hat{u}_P = 0. \tag{B.26}$$

## B.4 Velocity-pressure coupling (SIMPLEC algorithm)

Given the fact that the pressure is one of the main variables in the mathematical formulation, but there is no transport equation nor boundary conditions for it, a strategy to decouple the velocity and pressure fields must be applied. There are several techniques to achieve this, but in this work a pressure-correction methodology was implemented.

The first step is to guess a pressure field, $\hat{p}^*$, as initial approach. The corresponding momentum equations for such a field are then

$$a_P \hat{u}_P^* = a_N \hat{u}_N^* + a_S \hat{u}_S^* - \frac{ik}{r_P} \hat{p}_P^* \Delta V + \hat{S}_{up}, \tag{B.27}$$

$$a_P \hat{v}_P^* = a_N \hat{v}_N^* + a_S \hat{v}_S^* - \frac{\hat{p}_n^* - \hat{p}_s^*}{\Delta r} \Delta V + \hat{S}_{vp}, \tag{B.28}$$

where $\hat{u}^*$ and $\hat{v}^*$, in general do not satisfy mass conservation.

Now it is possible to define corrections for the variables:

$$\hat{u} = \hat{u}^* + \hat{u}', \quad \hat{v} = \hat{v}^* + \hat{v}', \quad \hat{p} = \hat{p}^* + \hat{p}', \tag{B.29}$$

the primed variables being small corrections that are added to the guessed variables in order to find the correct velocity and pressure fields.

Substraction of Equations (B.27) and (B.28) from Equations (B.20) and (B.23) yields

$$a_P \left( \hat{u}_P - \hat{u}_P^* \right) = \sum a_{nb} \left( \hat{u}_{nb} - \hat{u}_{nb}^* \right) - \frac{ik}{r_P} \Delta V \left( \hat{p}_P - \hat{p}_P^* \right), \tag{B.30}$$

$$a_P \left( \hat{v}_P - \hat{v}_P^* \right) = \sum a_{nb} \left( \hat{v}_{nb} - \hat{v}_{nb}^* \right) - \frac{\hat{p}_n - \hat{p}_s}{\Delta r} \Delta V + \frac{\hat{p}_n^* - \hat{p}_s^*}{\Delta r} \Delta V, \tag{B.31}$$

where the subscript $nb$ is used to refer to the neighboring control volumes.

From Eq. B.29 the above equations can be written as

$$a_P \hat{u}_P' = \sum a_{nb} \hat{u}_{nb}' - \frac{ik}{r_P} \Delta V \hat{p}_P', \tag{B.32}$$

$$a_P \hat{v}_P' = \sum a_{nb} \hat{v}_{nb}' - \frac{\hat{p}_n' - \hat{p}_s'}{\Delta r} \Delta V. \tag{B.33}$$

Depending on the considerations made regarding the first terms of the right-hand side in the previous equations, a family of methods can be constructed. The generic name for such a family is *SIMPLE*, which stands for Semi-Implicit Method for Pressure-Linked Equations. For the SIMPLEC algorithm (the "C" stands for "Consistent") the term $\sum a_{nb} \hat{u}_P'$ must be substracted from both equations, thus resulting in

$$\left( a_P - \sum a_{nb} \right) \hat{u}_P' = \sum a_{nb} \left( \hat{u}_{nb}' - \hat{u}_P' \right) - \frac{ik}{r_P} \Delta V \hat{p}_P', \tag{B.34}$$

$$\left(a_P - \sum a_{nb}\right) \hat{v}'_P = \sum a_{nb} \left(\hat{v}'_{nb} - \hat{v}'_P\right) - \frac{\hat{p}'_n - \hat{p}'_s}{\Delta r} \Delta V. \tag{B.35}$$

Since the corrections are considered to be small, the terms including the difference between the central point and its neighbors (first term on the right-hand side) can be neglected to obtain

$$\left(a_P - \sum a_{nb}\right) \hat{u}'_P = -\frac{ik}{r_P} \Delta V \hat{p}'_P, \tag{B.36}$$

$$\left(a_P - \sum a_{nb}\right) \hat{v}'_P = -\frac{\hat{p}'_n - \hat{p}'_s}{\Delta r} \Delta V. \tag{B.37}$$

Solving for the velocity corrections:

$$\hat{u}'_P = -\frac{\Delta V}{\left(a_P - \sum a_{nb}\right)} \frac{ik}{r_p} \hat{p}'_P = -du \frac{ik}{r_P} \hat{p}'_P, \tag{B.38}$$

$$\hat{v}'_P = -\frac{1}{\Delta r} \frac{\Delta V}{\left(a_P - \sum a_{nb}\right)} \left(\hat{p}'_n - \hat{p}'_s\right) = -dv \left(\hat{p}'_n - \hat{p}'_s\right). \tag{B.39}$$

Then, the velocity components can be calculated according to

$$\hat{u} = \hat{u}^* - du \frac{ik}{r_p} \hat{p}'_P, \quad \hat{v} = \hat{v}^* - dv \left(\hat{p}'_n - \hat{p}'_s\right). \tag{B.40}$$

In order to correct the velocity field, corrections for the pressure must be known, this can be achieved by substituting Equation B.40 into the discrete continuity equation (Eq. B.26)

$$\left(\hat{v}^*_n - (dv)_n \left(\hat{p}'_n - \hat{p}'_s\right)_n\right) S_n - \left(\hat{v}^*_s - (dv)_s \left(\hat{p}'_n - \hat{p}'_s\right)_s\right) S_s + \frac{ik}{r_P} \Delta V \left(\hat{u}^*_P - (du)_P \frac{ik}{r_p} \hat{p}'_P\right) = 0. \tag{B.41}$$

Since the continuity equation was made discrete at the same point as the pressure, it can be noted that the evaluation of the pressure differences at the north and south boundaries can be calculated according to

$$\left(\hat{p}'_n - \hat{p}'_s\right)_n = \hat{p}'_N - \hat{p}'_P, \quad \left(\hat{p}'_n - \hat{p}'_s\right)_s = \hat{p}'_P - \hat{p}'_S, \tag{B.42}$$

from which the equation for the pressure corrections is expressed as

$$\left(\hat{v}^*_n - (dv)_n \left(\hat{p}'_N - \hat{p}'_P\right)\right) S_n - \left(\hat{v}^*_s - (dv)_s \left(\hat{p}'_P - \hat{p}'_S\right)\right) S_s + \frac{ik}{r_p} \Delta V \left(\hat{u}^*_P - (du)_P \frac{ik}{r_p} \hat{p}'_P\right) = 0, \tag{B.43}$$

or in a more simplified form

$$a_P \hat{p}'_P = a_N \hat{p}'_N + a_S \hat{p}'_S + \hat{S}_{pP}, \tag{B.44}$$

with

$$a_N = (dv)_n S_n, \quad a_S = (dv)_s S_s, \quad , \tag{B.45}$$

$$a_P = a_N + a_S + \frac{k^2}{r_P^2} \Delta V (du)_P, \tag{B.46}$$

$$\hat{S}_{pP} = -\left( \hat{v}^*_n S_n - \hat{v}^*_s S_s + \frac{ik}{r_p} \Delta V \hat{u}^*_P \right). \tag{B.47}$$

Note that the source term (Eq. B.47) for this pressure correction is nothing but the negative of the discrete form of the divergence of the velocity field $\hat{\mathbf{u}}^*$.

Since the calculation of the pressure corrections was the only thing missing to complete the numerical methodology, now it is possible to list the complete procedure to follow in order to solve the governing equations:

1. Start with an initial guess for the pressure field, $\hat{p}^*$.
2. Calculate the coefficients for the velocity components (Eqs. B.21, B.22, B.24 and B.25).
3. With the guessed pressure, solve Equations B.27 and B.28 to get $\hat{u}^*$ and $\hat{v}^*$.
4. Having $\hat{u}^*$ and $\hat{v}^*$, calculate the coefficients for the pressure corrections (Eqs. B.45, B.46 and B.47).
5. Solve Eq. B.44 to get corrections for the pressure, $\hat{p}'$.
6. Correct the pressure by means of $\hat{p} = \hat{p}^* + \hat{p}'$.
7. With $\hat{p}'$, correct the velocity field by means of Eq. B.40
8. Iterate until convergence is reached using the following criterion:

   *The correct pressure field is obtained when the solution of the momentum equations yields a free-divergence velocity field.*

## B.5 Some comments on the numerical technique

Given the nature of the numerical scheme used in the present work, it is worth pointing out some important features of it. First, since the methodology combines a spectral and a finite volume approach, it has some of the advantages of both: in the one hand, the relative convergence of the solutions is better than the one obtained with finite volume only, but is not as good as with the purely spectral techniques; on the other hand, the structure of the linear systems of equations is similar to the ones obtained with FV, that is, diagonal systems for which very efficient numerical methodologies (such as TDMA) and computational libraries (like LAPACK or FISHPACK) have been developed. So, the hybrid scheme has a good balance between high convergence and simplicity to solve the discrete governing equations.

Another advantage of the hybrid technique is the implementation of the boundary conditions, which are exactly the same as for FV, except in the azimuthal direction, where it does not have to be implemented since the Fourier series expansion satisfies periodicity naturally. This way, the simplicity of FV method is conserved in the hybrid technique.

Finally, the hybrid methodology implemented calculates the Fourier coefficients of the variables of interest, this has the advantage that the calculation of the angular derivatives of the linear and nonlinear terms can be easily done since in Fourier space derivatives are calculated simply by multiplying by $ik$. In order to use this this approach, the Fast Fourier Transform (FFT) and its inverse must be calculated during the numerical solution of the governing equations, for which there are several computational tools to make both calculations efficiently.

Appendix C

# Numerical solution of hyperbolic PDE

As part of the PhD studies, a short-term research stay was done at the Osservatorio Astronomico di Cagliari (OAC), in Cagliari, Sardinia, Italy. The stay was supported by the *Associazone di Fondazione e di Casse di Risparmio Spa (ACRI)*, which is an Italian independent, non-profit, apolitical association aimed to "search cooperation oportunities between members and Italian and foreign entities, companies and relevant organizations" in order to "provide strategic planning and organizational asistance as well as develop international relations and arrange actions and projects with third parties". This stay was part of a Young Investigators Training Program (YITP) which was held alongside the $10^{th}$ PAMIR International Conference - Fundamental and Applied MHD in June 2016.

Since MHD phenomena play a major role in astrophysical flows, the objective of the one-month stay was to learn about the mathematical nature of the equations governing astrophysical flows and to develop numerical methods to solve them. This Appendix briefly describes the basic mathematical and numerical aspects of the governing equations and some textbook problems that were solved during the aforementioned stay. An easy-to-follow, detailed description of the numerical methods as well as its application to astrophysical flows, gas dynamics and many other phenomena can be found in LeVeque (1992), LeVeque *et al.* (1998) and LeVeque (2004).

## C.1 Hyperbolic conservation laws

The application of basic conservation principles to many physical situations results in the so-called conservation laws. Consider a one-dimensional domain over which the density of a conserved quantity $q(x,t)$ is distributed. In a finite-sized control

volume, the total amount $Q(t)$ enclosed between the interval $x \in [x_1, x_2]$ can be calculated by means of

$$Q(t) = \int_{x_1}^{x_2} q(x,t)dx. \tag{C.1}$$

If there are no sinks or sources of the physical quantity inside the control volume, the only way its value can change is because of the flux through its boundaries, hence

$$\frac{dQ}{dt} = \frac{d}{dt}\int_{x_1}^{x_2} q(x,t)dx = F_1(t) - F_2(t) = f(q(x_1,t)) - f(q(x_2,t)), \tag{C.2}$$

where the fluxes are considered to depend on the value of the density $q(x,t)$ in order to consider the most general case. Figure C.1 shows the sketch of the physical situation described above.

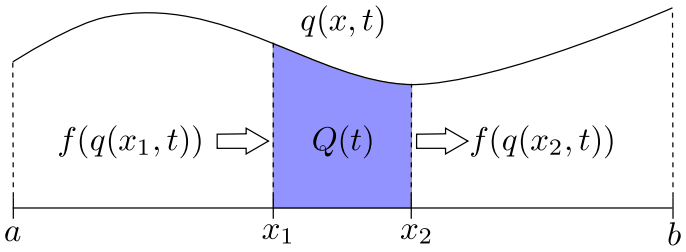


Figure C.1: Conservation of the physical quantity $q(x,t)$ in a one-dimensional domain $x \in [a,b]$. Since there are no sinks/sources in the control volume, the total amount of the physical quantity can only change due to the fluxes through its boundaries.

Equation C.2 is a *conservation law* and similar equations are encountered in very many physical situations when modeling natural phenomena. Using standard calculus notation Equation C.2 can be rewritten as

$$\frac{d}{dt}\int_{x_1}^{x_2} q(x,t)dx = -f(q(x,t))\Big|_{x_1}^{x_2}. \tag{C.3}$$

If the above equation is to be solved, the identity of the fluxes must be specified. It is common to relate the fluxes at the boundaries with the physical quantity of interest, so some assumptions can be made, for instance, if the quantity is being transported by a fluid (as it will be considered further in some examples), the flux at any point at

time $t$ can be considered as the product of the fluid velocity $u(x,t)$ times the density $q$:

$$f(q) = u(x,t)q.$$

If the velocity is constant, the flux becomes simpler as well as the equation itself. Regardless of the considerations about the flux, Equation C.3 must hold over every arbitrary interval $[x_1, x_2]$, which can be a difficult task to achieve, so, instead of tackling this equations directly, it can be converted into a partial differential equation that can be handled by different techniques. To do so, it should be rewritten in the form

$$\frac{d}{dt}\int_{x_1}^{x_2} q(x,t)dx = -\int_{x_1}^{x_2} \frac{\partial}{\partial x} f(q(x,t))dx. \tag{C.4}$$

By further manipulation it can be found that

$$\int_{x_1}^{x_2} \frac{\partial}{\partial t} q(x,t)dx = -\int_{x_1}^{x_2} \frac{\partial}{\partial x} f(q(x,t))dx, \tag{C.5}$$

$$\int_{x_1}^{x_2} \left[\frac{\partial}{\partial t} q(x,t) + \frac{\partial}{\partial x} f(q(x,t))\right] dx = 0. \tag{C.6}$$

Since the values of $x_1$ and $x_2$ can be chosen arbitrarily, the only way the above expression equals zero is if the integrand is also zero, hence the differential form of the conservation law is

$$\frac{\partial}{\partial t} q(x,t) + \frac{\partial}{\partial x} f(q(x,t)) = 0, \tag{C.7}$$

which is a hyperbolic partial differential equation (HPDE).

As stated before, HPDEs arise in many physical situations, for example, consider the Navier-Stokes equations for an incompressible viscous fluid

$$\frac{\partial \mathbf{u}}{\partial t} + (\mathbf{u}\cdot\nabla)\,\mathbf{u} = -\frac{1}{\rho}\nabla p + \nu\nabla^2\mathbf{u}, \tag{C.8}$$

where $\mathbf{u}$ is the velocity vector field, $p$ is the pressure field, $\rho$ and $\nu$ are the mass density per unit volume and kinematic viscosity of the fluid, respectively. Now, if the viscosity is neglected (ideal fluid) and the nonlinear term and the pressure gradient are algebraically manipulated, the resulting equations are the Euler equations in the form

$$\frac{\partial \mathbf{u}}{\partial t} + \nabla\cdot\left(\frac{1}{2}\mathbf{u}\mathbf{u} + \frac{1}{\rho}p\mathbf{I}\right) = 0, \tag{C.9}$$

which are hyperbolic in nature. Mathematically speaking, removing the diffusive term in Navier-Stokes changed its mathematical nature from parabollic to hyperbolic. It is woth noting that something similar happens in astrophysical level since astrophysical fluids have little to no viscosity, hence the mathematical equations governing astrophysical magnetohydrodynamic flows are also hyperbolic. Gas dynamics, relativistic flows and compressible fluids all are modeled using HPDE.

A very important feature of the hyperbolic equations is that they admit **shockwaves** in their solutions. Although, physically speaking, shockwaves are very steep gradients of a certain variable, mathematically they are discontinuities and, as such, must be handled very carefully when solving numerically the conservation equations because these discontinuities can appear even if the initial conditions are smooth.

## C.2 The Riemann problem

Since hyperbolic systems are likely to develop discontinuities in their solutions, this section is devoted to describe a classical problem where a simple discontinuity is present.

Consider the conservation equation C.7 together with the initial condition

$$q(x,0) = q_0(x) = \begin{cases} q_l, & \text{if } x < 0, \\ q_r, & \text{if } x \geqslant 0, \end{cases} \tag{C.10}$$

that is, piecewise constant data with a single jump discontinuity (Fig. C.2). This

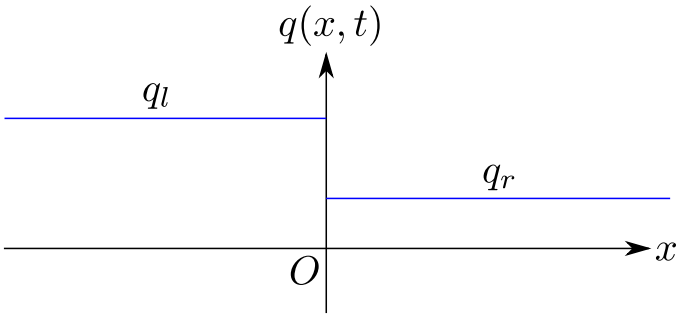


Figure C.2: The initial condition for the Riemann problem consist in a single jump discontinuity at $x = 0$.

problem, known as *Riemann problem*, is relatively easy to solve, but its solution reveals many aspects of the solutions of more complicated problems and constitutes the basis of many numerical methods for hyperbolic systems.

If the flux function is considered to be dependent on certain constant velocity $\bar{u}$, the conservation law simplifies to the linear advection equation

$$\frac{\partial q}{\partial t} + \bar{u}\frac{\partial q}{\partial x} = 0. \tag{C.11}$$

For this particular equation, it is easy to demonstrate that the solution has the form

$$q(x,t) = q_0(x - \bar{u}t), \tag{C.12}$$

that is to say, the initial discontinuity moves in the $x$-direction without changing its original shape. Figure C.3 shows this behavior.

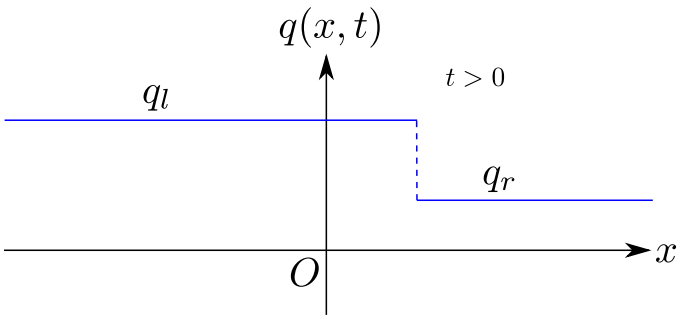


Figure C.3: If $\bar{u} > 0$, the discontinuity travels to the right as time passes.

The knowledge of this simple behavior of the solution to the linear advection equation was the main idea employed by Godunov to develop the numerical scheme named after him. Although the ideas of Godunov's method are simple, they are very powerful as a basis to develop better, more accurate methods for HPDE.

## C.3 Godunov's method (The REA algorithm)

One of the first methods to numerically solve conservation equations was proposed by Godunov (1959). Godunov's original idea is based on the finite volume method: the domain is discretized in several control volumes (closed intervals of size $\Delta x$ for

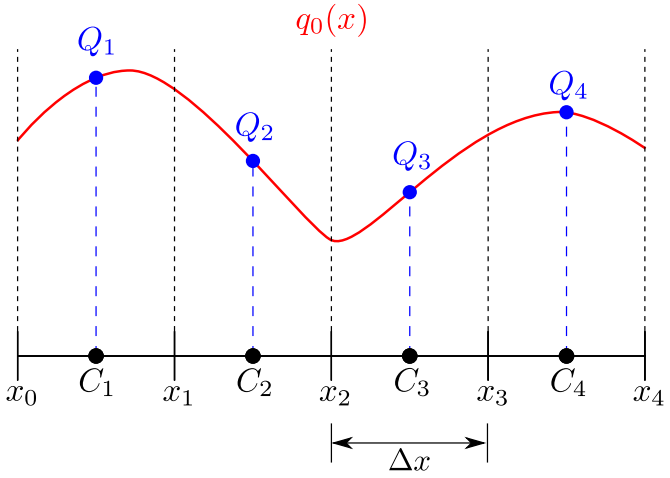


Figure C.4: Initial condition and space discretization for a hyperbolic problem.

the one-dimensional case), each of which is denoted by the interval $C_i = [x_{i-1}, x_i]$. At the center of each cell, the value of the initial condition is $Q_i$ (see Fig. C.4). As in the finite volume method, the first step in Godunov's method is to calculate average values for the variables of interest and assign this value to the whole cell. This can be done by means of the integral

$$\bar{q}_i(x) = \frac{1}{\Delta x} \int_{x_{i-1}}^{x_i} q_0(x) dx \quad \forall \quad x \in [x_{i-1}, x_i], \tag{C.13}$$

or by simply taking the value at the mid-point of the cell:

$$\bar{q}_i(x) = Q_i + \mathcal{O}(\Delta x^2) \quad \forall \quad x \in [x_{i-1}, x_i]. \tag{C.14}$$

The latter is a good approximation because has a good order of accuracy and is very simple to do, so it is better to calculate average values using Eq. C.14.

Once the average values has been assigned, the initial condition is now represented as a piecewise-constant **reconstruction** of the original distribution, as shown in Fig. C.5. Here the reconstruction is denoted by $\bar{q}_i(x, t_n)$, where $t_n$ represents the current time step. Note that this reconstruction has just created a discontinuity at the cell interfaces, thus a Riemann problem for each control volume arises.

If the time step is not that big, then it is expected that the original piecewise-constant function will only travel a small distance, so that the new solution is given by

$$\bar{q}_i^{n+1}(x) = \bar{q}_i(x - \bar{u}\Delta t, t_n). \tag{C.15}$$

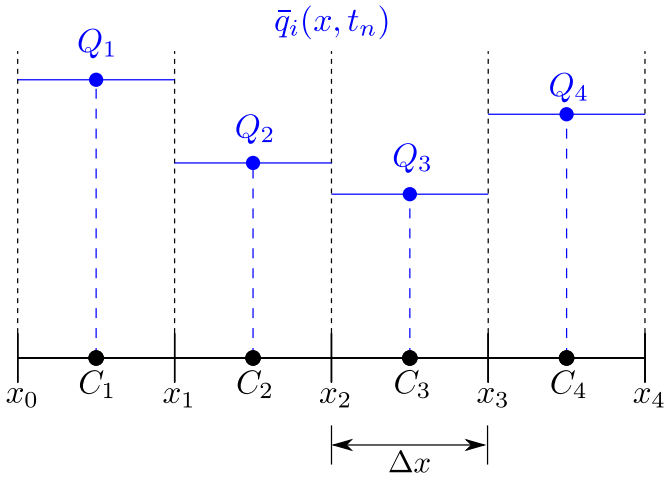


Figure C.5: Piecewise-constant reconstruction of the variable $q$ using average values. At the cell interfaces a Riemann problem is created as a result of the reconstruction.

So that, taking advantage of the behavior of the Riemann problem, the solution is **evolved** one time step forward simply by moving the profile obtained in the previous instant. Finally, the new **average** values can be found simply by calculating the area under the curve in every cell (which for this case is the area of two rectangles added together) and dividing it by $\Delta x$ (see Fig. C.6). As a result of this averaging procedure, a new piecewise-constant function is obtained and the algorithm must be repeated to continue advancing in time.

It is very important to point out that a necessary condition must be met in order for Godunov's method to be stable and converge to the correct solution: the *CFL condition* (named after Courant, Friedrichs and Lewy), which stablishes that the discontinuities must travel, at most, one cell from its previous position, that is to say, the information must have a chance to propagate at the correct physical speed. In mathematical terms

$$c = \left| \frac{\bar{u}\Delta t}{\Delta x} \right| \leqslant 1, \tag{C.16}$$

where $c$ is the Courant number, which compares the distance traveled by the discontinuity ($\bar{u}\Delta t$) with the length of the cell ($\Delta x$). This condition is necessary but not sufficient to ensure the stability of the numerical code. As it will be shown in the next examples, for the linear advection equation the best results are obtained when $c = 1$.

Finally, to close this section, Godunov's method (REA algorithm) can be summarized

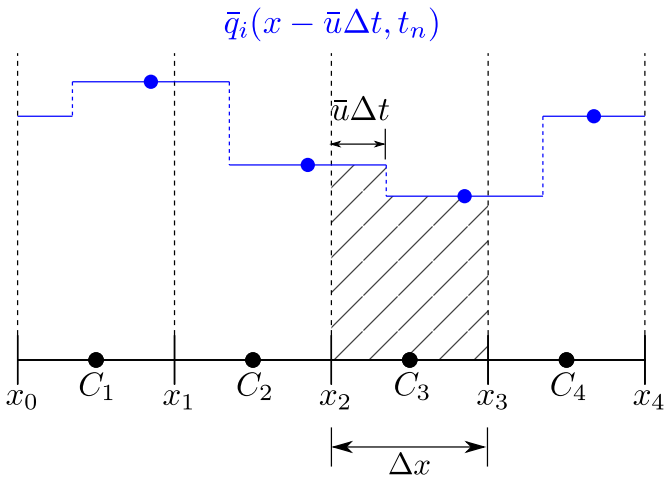


Figure C.6: The Riemann problem is evolved in time by moving the current distribution a distance $\bar{u}\Delta t$. After that, new average values can be found by calculating the area under the curve in every control volume.

in three steps:

1. **Reconstruct** a piecewise-constant function using average values for each cell.
2. **Evolve** (solve) the respective Riemann problems by means of exact or approximate solutions taking into account the CFL condition.
3. **Average** the solutions obtained in the previous step over each cell to obtain new cell averages.

### C.3.1 Numerical examples using Godunov's method

To show the behavior of the solutions obtained with the REA algorithm, the linear advection equation (Eq. C.11) was solved in the interval $x \in [-1, 1]$ using periodic boundary conditions, a time step $\Delta t = 0.01$ and $\bar{u} = 1$. The latter implies that the initial condition and the numerical solution should coincide everytime a revolution is completed (every unit time). Two different initial conditions, each with two different values of the Courant number, were tested: a smooth function,

$$q_0(x) = \sin(2\pi x), \tag{C.17}$$

and a discontinuous function,

$$q_0(x) = \begin{cases} 1, & -1 \leq x \leq -0.75, \\ 0, & -0.75 < x < -0.25, \\ 1, & -0.25 \leq x \leq 0.25, \\ 0, & 0.25 < x < 0.75, \\ 1, & 0.75 \leq x \leq 1. \end{cases} \tag{C.18}$$

Figure C.7 shows the solutions obtained using $c = 0.5$ and $c = 1.0$ for $t = 2$, that is, after two revolutions have been completed. It can be seen that this method gives very smeared solutions when the Courant number is equal to one half, and this is because this method, in general, introduces too many numerical difussion; as a result, the profiles get damped very fast as time passes and this cannot be avoided even for the smooth initial conditions, let alone for the discontinuous one, for which the discontinuities are completely absent in the numerical solution. On the other hand, for $c = 1$ the numerical solution and the initial condition are indistinguishable from each other (even for the discontinuous case) and this is because the piecewise-constant profile travels exactly on cell each time step, so the average values calculated at the end of the REA algorithm are the same as in the previous time step, thus the shape of the profile is exactly the same since no numerical difussion is introduced in the solution. Unfortunately, the absence of numerical difussion is expected to happen only for very simple equations. If the velocity $u$ is not constant or if the conservation equation is nonlinear, then the discontinuities at each cell interface will travel a different distance in the same time interval and the the numerical solution will be damped.

In order to improve the numerical solutions given by Godunov's method, different reconstructions have have been proposed. The next section briefly describes some of them.

### C.3.2 Piecewise-linear reconstruction

The REA algorithm previously described makes a reconstruction by means of a piecewise-constant function, then solves the Riemann problems arising at the cell interfaces and finally averages over each cell to get a new reconstruction for the next time step. One of the ways to improve the numerical method in order to increase the order of accuracy is to make a higher-order reconstruction, thus the algorithm remains the same and only the reconstruction based on the average values is modified.

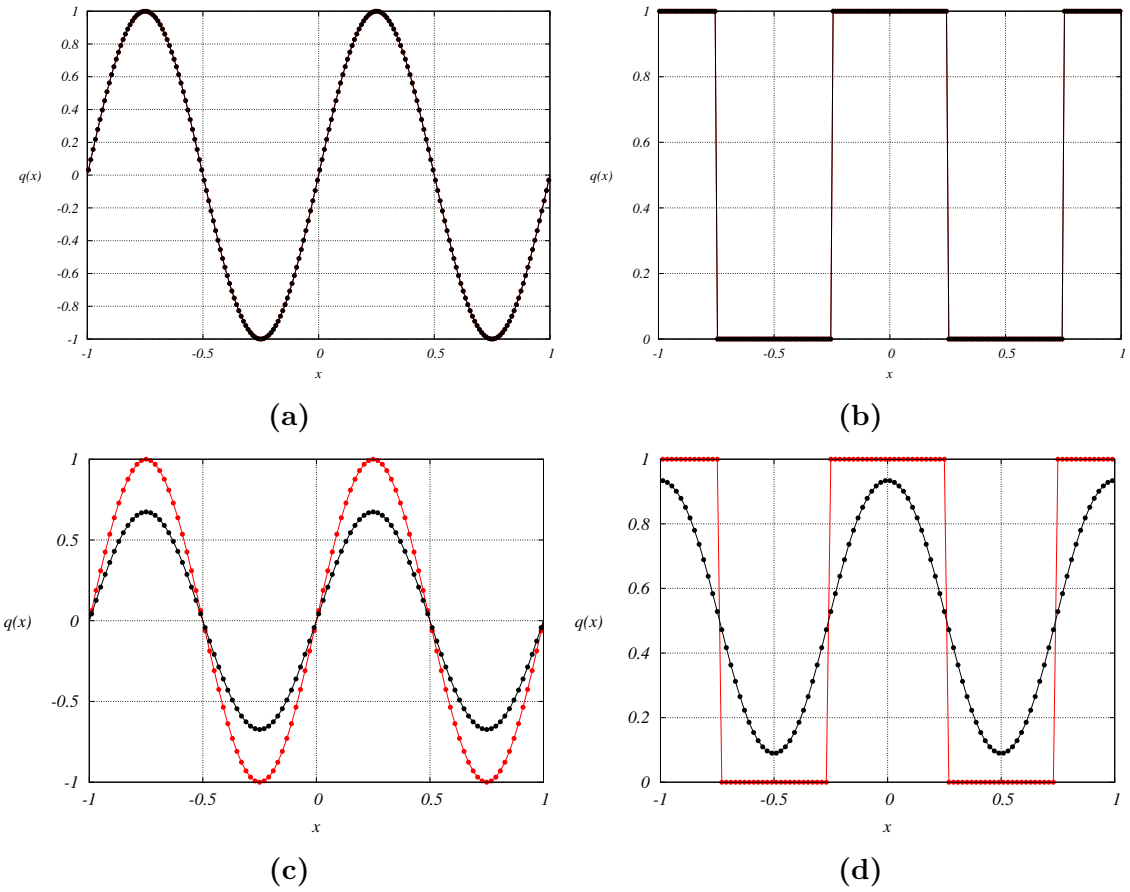


Figure C.7: Solutions for the linear advection equation using $c = 0.5$ (lower row) and $c = 1$ (upper row) for a smooth (left column) and discontinuous (right column) initial condition. Red line is the initial condition whereas the black line is the numerical solution.

A piecewise-linear reconstruction at every control volume has the form

$$\bar{q}_i(x, t_n) = Q_i + \sigma_i(x - \bar{x}_i) \quad \forall \quad x \in [x_{i-1}, x_i], \tag{C.19}$$

where $\sigma_i$ is the slope of the linear function at the $i$-th cell and $\bar{x}_i = \frac{1}{2}(x_{i-1} + x_i)$ is the middle-point of the interval (see Fig. C.8). This reconstruction has the advantage that the average value in each cell equals the value of the linear function evaluated at the middle-point, no matter what value the slope $\sigma_i$ takes. The latter is crucial in order for the method to be conservative.

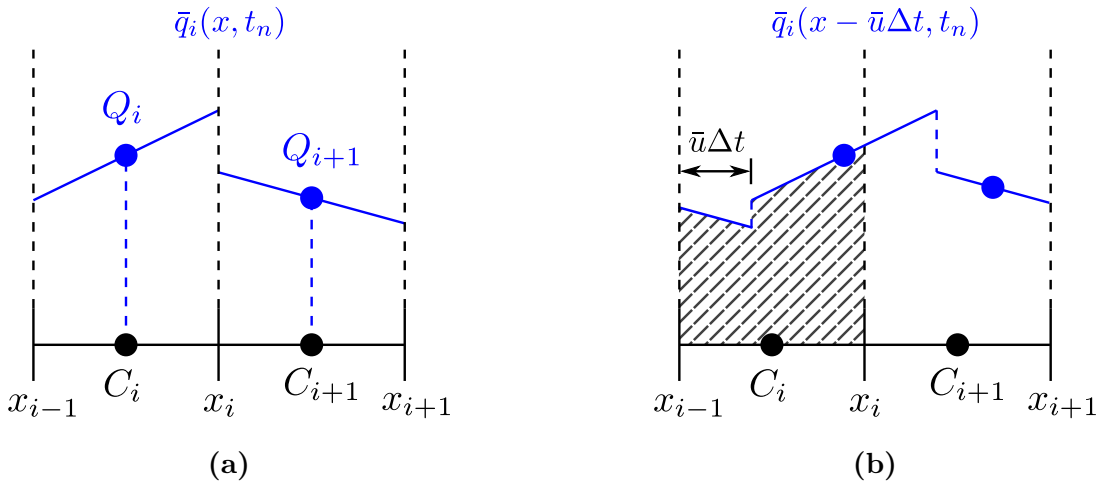


Figure C.8: Piecewise-linear reconstruction. ($a$) Choosing this reconstruction also creates a Riemann problem at each interface. ($b$) The linear distribution is evolved by moving the previous distribution to the right.

To implement this new approximation only one question remains: what values for the slopes must be chosen?

### Slope/flux limiters

It is clear that choosing $\sigma_i = 0$ results in the original Godunov's method, so it is desirable to chose nonzero values for the slopes. With this in mind and given the fact that two points are nedeed to calculate the slope, three possibilities arise: use the previous and current cells ($i$ and $i - 1$), the next and current cells ($i$ and $i + 1$) or the previous and next cells ($i + 1$ and $i - 1$). Even though these three choices

are the most natural to implement, many other choices, which can alternate between the three basic ones, can be made. It is important to note that the choice of the slopes is a very easy-to-grasp geometrical interpretation, but it can also be given a physical one as the values chosen to limit the fluxes through the boundaries in each cell. Since these fluxes are related to the spatial derivative of the function $f(q(x,t))$, they can be approximated from

$$\frac{\Delta Q_i}{\Delta x} = \frac{Q_{i+1} - Q_i}{\Delta x}, \tag{C.20}$$

where $\Delta Q_i$ is the jump discontinuity at the $i$-th interface.

For the linear advection equation, it can be shown that the discrete form of the fluxes considering a linear reconstruction has the form

$$F_i = \max(\bar{u}, 0)Q_i + \min(\bar{u}, 0)Q_{i+1} + \frac{1}{2}|\bar{u}| \left(1 - \left|\frac{\bar{u}\Delta t}{\Delta x}\right|\right) \phi(\theta_i)\Delta Q_i, \tag{C.21}$$

where it has been considered that the velocity $\bar{u}$ can have positive or negative values. $\phi$ is the *flux-limiter function*, which depends on the variable

$$\theta_i = \frac{\Delta Q_I}{\Delta Q_i}, \quad \text{with} \quad I = \begin{cases} i-1, & \text{if } \bar{u} > 0, \\ i+1, & \text{if } \bar{u} \leqslant 0. \end{cases}$$

Depending in the choice of the variable $\theta$, different methods can be obtained. Table C.1 shows different choices for the flux-limiter function.

Table C.1: Different methods for piecewise-linear reconstruction.

| Method | $\phi(\theta)$ |
|---|---|
| Godunov | 0 |
| Lax-Wendroff | 1 |
| minmod | minmod(1,$\theta$) |
| Superbee | max(0,min(1,2$\theta$),min(2,$\theta$)) |
| MC | max(0,min((1+$\theta$)/2,2,2$\theta$)) |
| van Leer | $\dfrac{\theta + \lvert\theta\rvert}{1 + \lvert\theta\rvert}$ |

The function minmod is defined by

$$\text{minmod}(a,b) = \begin{cases} a, & \text{if } |a| < |b| \text{ and } ab > 0, \\ b, & \text{if } |b| < |a| \text{ and } ab > 0, \\ 0, & \text{if } ab \leqslant 0. \end{cases}$$

### C.3.3 Numerical results using piecewise-linear reconstruction

To show the improvements achieved with a higher-order reconstruction, the linear advection equation was solved using the same inital conditions as for Godunov's method (Eqs. C.17 and C.18). Figure C.9 shows the comparison between the initial condition and the numerical results obtained using the different methods pointed out in Table C.1 considering a smooth initial condition, whereas Fig. C.10 shows the same except that the initial condition is discontinuous. In both cases the Courant number was chosen to be $c = 0.5$. Since the boundary conditions are periodic and the value of the velocity is $\bar{u} = 1$, the initial condition and the numerical solution must coincide everytime a whole revolution is completed. Both figures are shown for $t = 2$.

For the smooth data, as it was previously seen, Godunov's method introduces too many numerical difussion, thus giving very smeared solutions. The other five numerical solutions are second-order accurate, that is why they agree very well with the initial condition. Among the five it can be noticed that Lax-Wendroff and the MC limiter yield the most accurate solutions.

For the discontiuous data, again Godunov's method gives smeared solutions and is not capable of approximating the discontinuities of the problem. For this case the worst solution is given by the Lax-Wendroff method, this is because Lax-Wendroff is based in a linear reconstruction of the solution which calculates very large slopes/fluxes near the discontinuities. These large slopes/fluxes eventually produce unphysical oscillations that grow as time goes by. To avoid these oscillations, slope/flux limiters are implemented. The Superbee and MC-limiters are the most accurate solutions because are able to track the discontinuities although they are somewhat smoothed.

From the shown examples, it can be clearly seen that increasing the order of the reconstruction from order one to order two greatly increases the accuracy of the numerical solutions, nevertheless Godunov's method is still the most used approximation employed when simulating astrophysical flows [*e. g.* Bachetti *et al.* (2010),

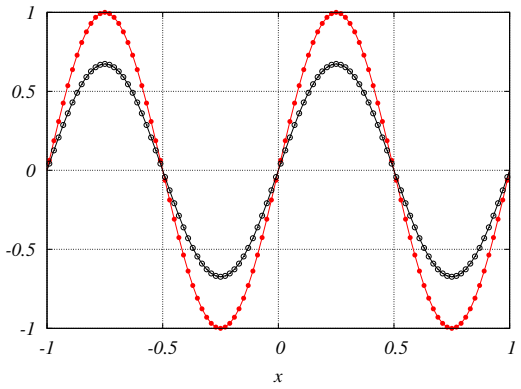


**(a)** Godunov

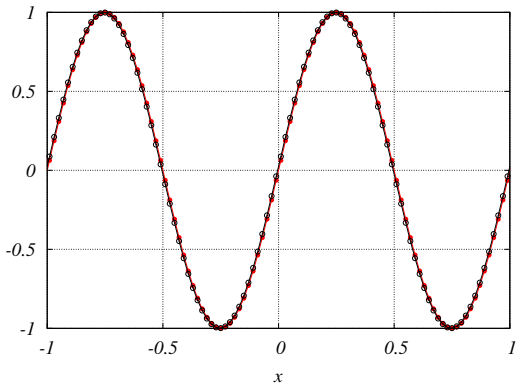


**(b)** Lax-Wendroff

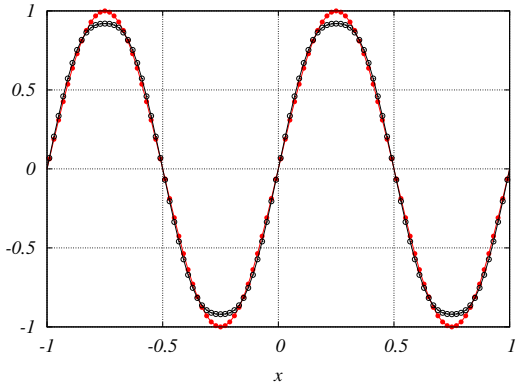


**(c)** minmod limiter

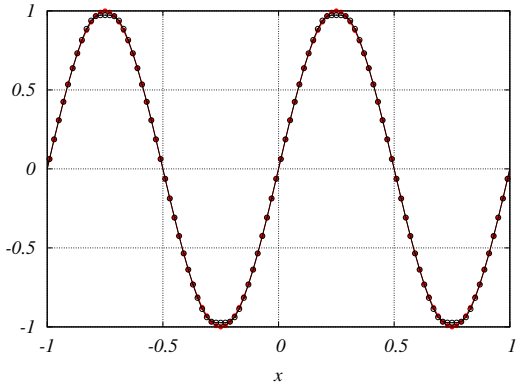


**(d)** MC limiter

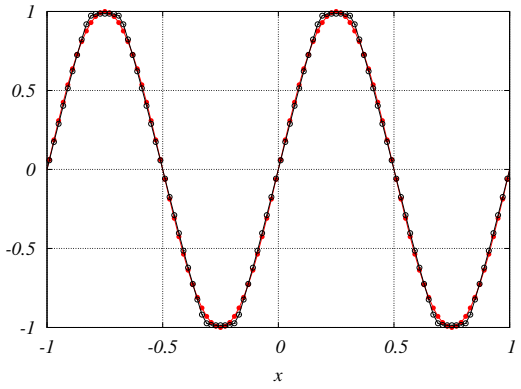


**(e)** Superbee limiter

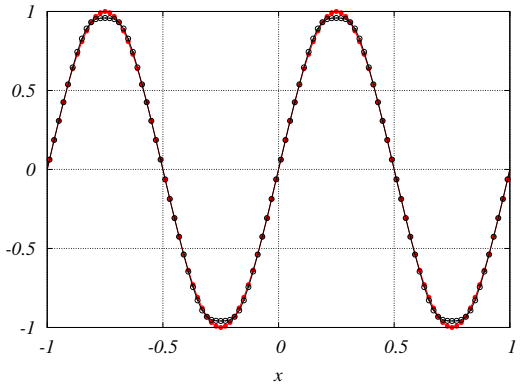


**(f)** van Leer

Figure C.9: Comparison between the analytical solution (in red) and numerical solutions (in black) for the one-dimensional linear advection problem with periodic boundary conditions and a smooth initial condition.

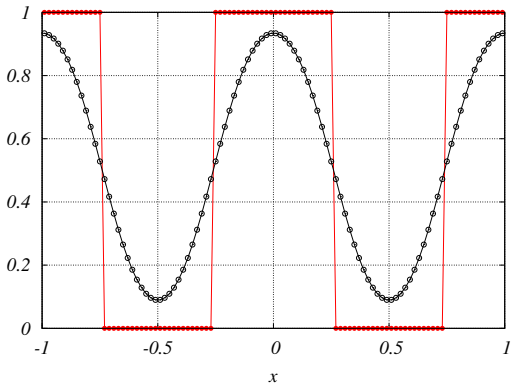


**(a)** Godunov

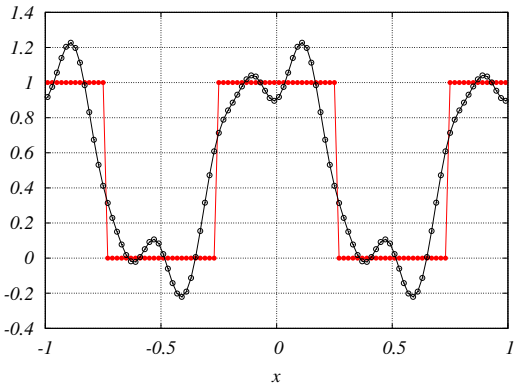


**(b)** Lax-Wendroff

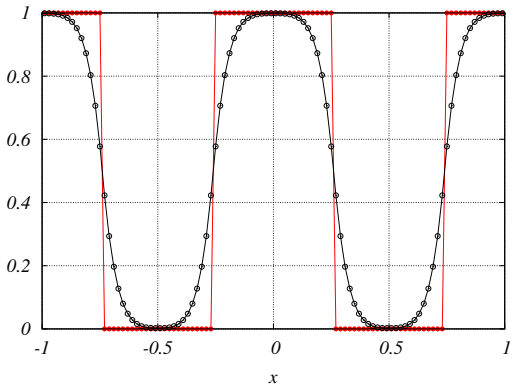


**(c)** minmod limiter

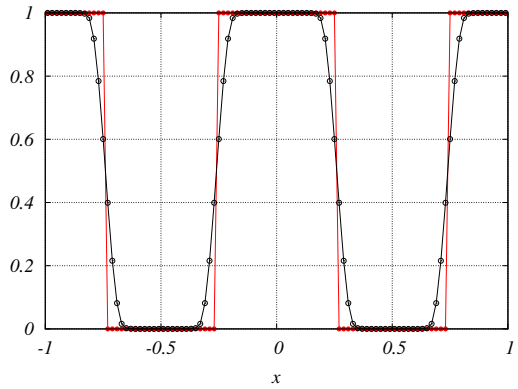


**(d)** MC limiter

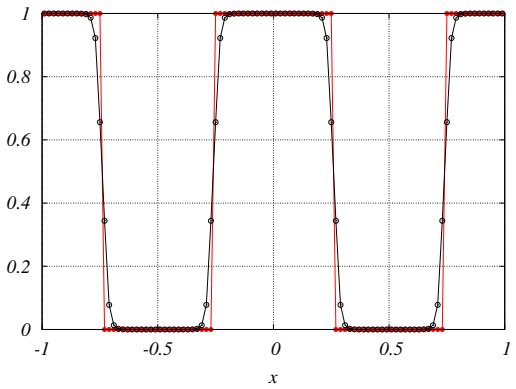


**(e)** Superbee limiter

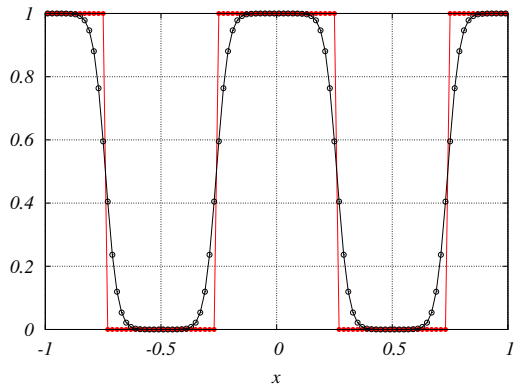


**(f)** van Leer

Figure C.10: Comparison between the analytical solution (in red) and numerical solutions (in black) for the one-dimensional linear advection problem with periodic boundary conditions and a discontinuous initial condition.

Romanova *et al.* (2013)]. Observing this behavior, the goal of the one-month stay was to explore the possibility of implementing a global (spectral) approximation to solve hyperbolic PDE. Since the idea behind spectral methods is to increment the order of approximation so that the calculations are done considering all the points in the domain, not just the immediate neighbors, at first glance it appears that this is plausible, unfortunately, due to the short time available to focus on this project, it was not possible to advance further to achieve this goal.

# Bibliography


[1] Andreev, O., Haberstroh, C., & Thess, A. (2001). "MHD flow in electrolytes at high Hartmann numbers". *Magnetohydrodynamics* **37**, 151–160.

[2] Asai, S. (2012). "Electromagnetic processing of materials". Springer, Berin.

[3] Bachetti, M., Romanova, M. M., & Kulkarni, A. (2010). "QPO emission from moving hot spots on the surface of neutron stars: a model". *Mon. Not. R. Astrom. Soc.* **0**, 14.

[4] Batchaev, A. M. & Ponomarev, V. M. (1989). "Experimental and theoretical investigation of Kolmogorov flow in a cylindrical surface". *Izvestiya Akademii Nauk SSR, Mekhanika Zhidkosti i Gaza* **5**, 25–31.

[5] Bau, H. H., Zhu, J., Qian, S., & Xiang, Y. (2003). "A magneto-hydrodynamically controlled fluidic network". *Sensors and Actuators, B: Chemical* **88**, 206–216.

[6] Baylis, J. A. (1971). "Experiments on laminar flows in curved ducts of square cross-section". *Journal of Fluid Mechanics* **48**, 417–422.

[7] Baylis, J. A. & Hunt, J. C. R. (1971). "MHD flow in an annular channel: theory and experiment". *Journal of Fluid Mechanics* **48**, 423–428.

[8] Beltrán, A. (2010). "Dinámica de flujos en obstáculos magnéticos". PhD Thesis, Centro de Investigación en Energía, UNAM.

[9] Bondarenko, N. F., Gak, E. Z., & Gak, M. Z. (2002). "Application of MHD effects in electrolytes for modelling vortex processes in natural phenomena and in solving engineering-physical problems". *Journal of Engineering Physics and Thermophysics* **75**, 1234–1247.

[10] Bondarenko, N. F. & Gak, M. Z. (1978). "Application of Magnetohydrodynamic Effects in Electrolytes for Modeling Eddy Hydrodynamic Processes". *Atmospheric and Oceanic Physics* **14** (2), 146–150.

[11] Bondarenko, N. F., Gak, M. Z., & Dolzhanskiy, F. V. (1979). "Laboratory and Theoretical Models of Plane Periodic Flow". *Atmospheric and Oceanic Physics* **15** (10), 711–716.

[12] Bracco, A., Chavanis, P. H., & Provenzale, A. (1999). "Particle aggregation in a turbulent Keplerian flow". *Physics of Fluids* **11**, 2280–2287.

[13] Canuto, C., Quarteroni, A., hussaini, M. Y., & Zang, T. A. (2006). "Spectral methods Fundamental in Single Domains". Springer.

[14] Chang, C. C. & Lundgren, T. S. (1959). "Flow of an incompressible fluid in a hydrodynamic capacitor". *Physics of Fluids* **2** (2), 627–632.

[15] Cuevas, S. (2004). "Introducción a la magnetohidrodinámica: Memorias de la escuela de verano de física". UNAM-UAEM.

[16] Currie, I. G. (2007). "Fundamental mechanics of fluids". Cambridge. Third edition.

[17] Davidson, P. A. (2001). "An introduction to magnetohydrodynamics". Cambridge.

[18] Digilov, R. M. (2007). "Making a fluid rotate: Circular flow of a weakly conducting fluid induced by a Lorentz body force". *American Journal of Physics* **75**, 361–367.

[19] Dolzhanskii, F. V., Krymov, V. A., & Manin, D. Y. (1992). "An advanced experimental investigation of quasi-two-dimensional shear flows". *Journal of Fluid Mechanics* **241**, 705–722.

[20] Dolzhanskii, F. V., Krymov, V. A., & Manin, D. Y. (1990). "Stability and Vortex Structures of Quasi-Two-Dimensional Shear Flows". *Sov. Phys. Usp.* **33** (7), 495–520.

[21] Domínguez, D. R. (2013). "Diseño, construcción y caracterización de un circuito de metal líquido impulsado por una bomba de inducción MHD". Master Thesis, Instituto de Energías Renovables, UNAM.

[22] Dovzhenko, V. A., Novikov, Y. V., & Obuhkov, A. M. (1979). "Modeling the Vortex Generation Process in an Axially Symmetrical Azimuthal Field by a Magnetohydrodynamic Method". *Atmospheric and Oceanic Physics* **15** (11), 834–836.

[23] Dovzhenko, V. A., Obuhkov, A. M., & Ponomarev, V. M. (1981). "Generation of Vortices in an Axisymmetric Shear Flow". *Izvestiya Akademii Nauk SSR, Mekhanika Zhidkosti i Gaza* No. 4, 27–36.

[24] Figueroa, A. (2010). "Dinámica de vórtices generados mediante fuerzas electromagnéticas". PhD Thesis, Centro de Investigación en Energía, UNAM.

[25] Figueroa, A., Demieaux, F., Cuevas, S., & Ramos, E. (2009). "Electrically driven vortices in a weak dipolar magnetic field in a shallow electrolytic layer". *Journal of Fluid Mechanics* **641**, 245–261.

[26] Fleisch, D. (2008). "A student's guide to the Maxwell's equations". Cambridge.

[27] Furlani, E. P. (2001). "Permanent Magnet and Electromechanical Devices". Academic Press.

[28] Gak, E. Z. (1981). "Hydrodynamic Effects in Water Media in Electric and Magnetic Fields". *Inzhenerno-Fizicheskii Zhurnal* **43** (1), 140–153.

[29] Ghallab, Y. H. & Badawy, W. (2010). "Lab-on-a-Chip Techniques, Circuits and Biomedical Applications". Artech House.

[30] Gledzer, A. E., Gledzer, E. B., Khapaev, A. A., & Chkhetiani, O. G. (2013). "Experimental Manifestation of Vortices and Rossby Wave Blocking at the MHD Excitation of Quasi-Two-Dimensional Flows in a Rotating Cylindrical Vessel". *JETP Letters* **97** (6), 359–365.

[31] Gleeson, J. P. (2005). "Transient micromxing: Examples of laminar and chaotic stirring". *Physics of Fluids* **17**, 100614.

[32] Gleeson, J. P., Roche, O. M., West, J., & Gelb, A. (2004). "Modeling annular micromixers". *SIAM Journal of Applied Mathematics* **64** (4), 1294–1310.

[33] Godunov, S. K. (1959). "A difference method for numerical calculation of discontinuous solutions of the equations of hydrodynamics *(in Russian)*". *Mat. Sb.* **47** (3), 271–306.

[34] Hjellming, L. N. & Walker, J. S. (1986). "Melt motion in a Czochralski cristal puller with an axial magnetic field: isothermal motion". *Journal of Fluid Mechanics* **164**, 237–273.

[35] Kessey, K. O. (1964). "Rotating electrically conducting fluid in a long cylinder". *AIAA Journal* **2** (5), 864–871.

[36] Korpiva, D. A. (2009). "Implementing Spectral Methods for Partial Differential Equations". Springer.

[37] Krymov, V. A. (1989). "Stability and Supercritical Regimes of Quasi-Two-Dimensional Shear Flow in the Presence of External Friction (Experiment)". *Izvestiya Akademii Nauk SSR, Mekhanika Zhidkosti i Gaza* No. 2, 12–18.

[38] LeVeque, R. J., Mihalas, D., Dorfi, E. A., & Müller, E. (1998). "Computational Methods for Astrophysical Fluid Flow". Springer.

[39] LeVeque, R. J. (2004). "Finite-Volume Methods for Hyperbolic Problems". Cambridge University Press.

[40] LeVeque, R. J. (1992). "Numerical Methods for Conservation Laws". Birkhaüser Verlag.

[41] Li, P. C. H. (2005). "Microfluidic Lab-on-a-Chip for Chemical and Biological Analysis and Discovery". Taylor & Francis.

[42] Manin, D. Y. (1989). "Stability and Supercritical Regimes of Quasi-Two-Dimensional Flow in the Presence of External Friction (Theory)". *Izvestiya Akademii Nauk SSR, Mekhanika Zhidkosti i Gaza* No. 2, 19–26.

[43] Marcus, P. S. (1990). "Vortex dynamics in a shearing zonal flow". *Journal of Fluid Mechanics* **215**, 393–430.

[44] McCaig, M. (1977). "Permanent magnets in theory and practice". Wiley.

[45] Mikhailovich, B. (2010). "Some properties of turbulent rotating MHD flows under crossed electrical and magnetic fields". *Magnetohydrodynamics* **46** (4), 381–386.

[46] Mikhailovich, B., Shapiro, A., Sukoriansky, S., & Zilberman, I. (2012). "Experiments with turbulent rotating MHD flows in an annular gap". *Magnetohydrodynamics* **48** (1), 43–50.

[47] Moresco, P. & Alboussière (2004). "Experimental study of the instability of the Hartmann layer". *Journal of Fluid Mechanics* **504**, 167–181.

[48] Nuñez, J., Ramos, E., Hernández-Cruz, G., Vargas, M., & Cuevas, S. (2012). "Verification and experimental validation of a numerical simulation of natural convection in a slender cylinder". *International Journal of Heat and Fluid Flow* **38**, 118–125.

[49] Nuñez, J. (2012). "Simulación numérica de la convección bajo la influencia de fuerzas electromagnética y fuerzas de rotación". PhD Thesis, Centro de Investigación en Energía, UNAM.

[50] Nuñez, J., Ramos, E., & López, L. M. (2012). "A mixed Fourier-Galerkin-finite-volume method to solve the fluid dynamics equations in cylindrical geometries". *Fluid Dynamics Research* **44**, 031414 (10pp).

[51] Pérez-Barrera, J., Ortíz, A., & Cuevas, S. (2016). *Recent Advances in Fluid Dynamics with Environmental Applications* chapter Analysis of an annular MHD stirrer for microfluidic applications, pages 275–288. Springer.

[52] Pérez-Barrera, J., Pérez-Espinoza, J. E., Ortíz, A., Ramos, E., & Cuevas, S. (2015). "Instability of electrolyte flow driven by an azimuthal Lorentz force". *Magnetohydrodynamics* **51**, 203–213.

[53] Pérez-Espinoza, J. E. (2012). "Diseño y construcción de un agitador magneto-hidrodinámico". Bachelor Thesis, Instituto Tecnológico de Zacatepec.

[54] Peyret, R. (2002). "Spectral Methods for Incompressible Viscous Flow". Springer.

[55] Ponomarev, V. M. (1980). "Stability of a Class of Axisymmetric Flows of an Incompressible Liquid". *Izvestiya Akademii Nauk SSR, Mekhanika Zhidkosti i Gaza* No. 1, 3–9.

[56] Qian, S. & Bau, H. H. (2009). "Magneto-Hydrodynamics Based Microfluidics". *Mech. Res. Commun.* **31** (1), 10–21.

[57] Qin, M. & Bau, H. H. (2012). "Magnetohydrodynamic flow of a binary electrolyte in a concentric annulus". *Physics of Fluids* **24**, 037101–1–20.

[58] Rivero, M. A. & Cuevas, S. (2012). "Analysis of the slip condition in magnetohydrodynamic (MHD) micropumps". *Sensors and Actuators, B: Chemical* **166-167**, 887–892.

[59] Román, J. J. (2012). "Estudio numérico de la transferencia de calor en un flujo a través de arreglos de obstáculo magnéticos". Master Thesis, Centro de Investigación en Energía, UNAM.

[60] Romanova, M. M., Ustyugova, G. V., Koldoba, A. V., Wick, J. V., & Lovelace, R. V. E. (2013). "Three-dimensional simulations of disk accretion to inclined dipole: I. Magnetospheric flow at different Θ". *The Astrophysical Journal* **595** (2), 1009–1031.

[61] Samimy, M., Breuer, K. S., Leal, L. G., & Steen, P. H. (2003). "A Galery of Fluid Motion". Cambridge University Press.

[62] Satijn, M. P., Cense, A. W., Verzicco, R., Clercx, H. J. H., & van Heijst, G. J. F. (2001). "Three-dimensional structure and decay properties of vortices in shallow fluid layers". *Physics of Fluids* **13**, 1932–1945.

[63] Schweitzer, S. & Soler, A. (1970). "One-dimensional viscous magnetofluiddynamic flow in an annulus". *J. Franklin Inst.* **289** (6), 445–456.

[64] Smolentsev, S., Cuevas, S., & Beltrán, A. (2010). "Induced electric current-based formulation in computations of low magnetic Reynolds number magnetohydrodynamic flows". *Journal of Computational Physics* **229**, 1558–1572.

[65] Sommeria, J. (1988). "Electrically driven vortices in a strong magnetic field". *Journal of Fluid Mechanics* **189**, 553–569.

[66] Suslov, S. A., Pérez-Barrera, J., & Cuevas, S. (2017). "Electtromagnetically driven flow of electrolyte in a thin annular layer: axisymmetric solutions". *Journal of Fluid Mechanics* **828**, 573–600.

[67] Thess, A., Votyakov, E. V., Knaepen, B., & Zikanov, O. (2007). "Theory of the Lorentz force flowmeter". *New Journal of Physics* **9**, 28.

[68] Thess, A., Votyakov, E. V., & Kolesnikov, Y. (2006). "Lorentz Force Velocimetry". *Physical Review Letters* **96** (16), 164501–1–164501–4.

[69] Van Heijst, G. J. F., Kloosterziel, R. C., & Williams, C. W. M. (1991). "Laboratory experiments on the tripolar vortex in a rotating fluid". *Journal of Fluid Mechanics* **225**, 301–331.

[70] Versteeg, H. K. & Malalasekera, W. (1995). "An Introduction to Computational Fluid Dynamics: the finite volume method". Longman Scientific & Technical.

[71] West, J., Gleeson, J. P., Alderman, J., Collins, J. K., & Berney, H. (2003). "Structuring laminar flows using annular magnetohydrodynamic actuation". *Sensors and Actuators, B: Chemical* **96**, 190–199.

[72] Yi, M., Qian, S., & Bau, H. H. (2002). "A magnetohydrodynamic chaotic stirrer". *Journal of Fluid Mechanics* **468**, 153–177.

[73] Zhao, Y. & Zikanov, O. (2012). "Instabilities and turbulence in magnetohydrodynamic flow in a toroidal duct prior to transition in Hartmann layers". *Journal of Fluid Mechanics* **692**, 288–316.

[74] Zhao, Y., Zikanov, O., & Krasnov, D. (2011). "Instability of magnetohydrodynamic flow in an annular channel at high Hartmann numbers". *Physics of Fluids* **23**, 084103.